Shashi Thutupalli

Towards Autonomous Soft Matter Systems

Experiments on Membranes and Active Emulsions

Springer

Springer Theses

Recognizing Outstanding Ph.D. Research

Aims and Scope

The series "Springer Theses" brings together a selection of the very best Ph.D. theses from around the world and across the physical sciences. Nominated and endorsed by two recognized specialists, each published volume has been selected for its scientific excellence and the high impact of its contents for the pertinent field of research. For greater accessibility to non-specialists, the published versions include an extended introduction, as well as a foreword by the student's supervisor explaining the special relevance of the work for the field. As a whole, the series will provide a valuable resource both for newcomers to the research fields described, and for other scientists seeking detailed background information on special questions. Finally, it provides an accredited documentation of the valuable contributions made by today's younger generation of scientists.

Theses are accepted into the series by invited nomination only and must fulfill all of the following criteria

- They must be written in good English.
- The topic should fall within the confines of Chemistry, Physics, Earth Sciences, Engineering and related interdisciplinary fields such as Materials, Nanoscience, Chemical Engineering, Complex Systems and Biophysics.
- The work reported in the thesis must represent a significant scientific advance.
- If the thesis includes previously published material, permission to reproduce this must be gained from the respective copyright holder.
- They must have been examined and passed during the 12 months prior to nomination.
- Each thesis should include a foreword by the supervisor outlining the significance of its content.
- The theses should have a clearly defined structure including an introduction accessible to scientists not expert in that particular field.

Shashi Thutupalli

Towards Autonomous Soft Matter Systems

Experiments on Membranes and Active Emulsions

Doctoral Thesis accepted by
the University of Göttingen, Germany

🐎 Springer

Author
Dr. Shashi Thutupalli
Department of Physics
Princeton University
Princeton, NJ
USA

Supervisor
Prof. Stephan Herminghaus
Department for Dynamics of Complex
  Fluids
Max Planck Institute for Dynamics
  and Self-Organization
Göttingen
Germany

To my parents and grandparents

Supervisor's Foreword

The spontaneous formation of patterns and structures in systems far from thermal equilibrium belongs to the most fascinating phenomena in nature. Without such processes there would not be any life, leave alone anyone to do science. The bizarre morphologies into which bacterial colonies evolve, the dazzling number of inter-dependent self-organizing sub-systems (ions, nucleic acids, proteins, organelles) which organize their metabolism, yield just a glance at the immense organizational power of living systems. Yet the overarching principles of such self-organizing, autonomous systems are as yet elusive.

In order to achieve a deeper understanding of the underlying physics of self-organization, and possibly to venture out into new areas of application, it would be very desirable to come up with artificial systems which imitate life at the micro-scopic level. In fact, recent developments in droplet-based microfluidics have paved the way to the preparation of compartmentalized soft-matter systems con-sisting of similar building blocks as cellular organisms.

The work Shashi Thutupalli is presenting here provides a considerable step forward in this direction. Rafts of droplets of aqueous suspensions are created which are separated from each other only by lipid bilayers. It is shown that the latter can not only be used to incorporate membrane proteins such as ion channels, but also as interesting nonlinear electrical circuitry elements. By introducing oscillating chemical reactions in the droplets, complex coupling patterns can be observed which depend upon the properties of the membranes between adjacent droplets. This provides already a high-level integration of nonlinearity, pattern formation, and biological building blocks.

In a further step, the packing density of the droplets is reduced such that they become freely mobile. A formulation is found which gives rise to locomotion of the droplets, such that their collective behavior can be investigated as another direct consequence of nonequilibrium physics. By a simple rectification experi-ment, it is demonstrated that the behavior of swarming droplets is fundamentally different from diffusing Brownian particles, although it appears similar to the unexperienced eye. Other striking phenomena like single-file diffusion of active particles can be studied here as well.

In a nutshell, this book provides deep insight into self-assembly and collective phenomena in systems which are extremely versatile and can be well controlled. It is to be expected that it will spur a considerable amount of further research into autonomous soft-matter systems.

Göttingen, May 2013   Prof. Stephan Herminghaus

Acknowledgments

I owe my deepest gratitude to Prof. Stephan Herminghaus for his supervision and guidance during this work. He has provided me with innumerable opportunities, has let me fly with my imagination when I wanted to and has led me by hand when I needed it. I still remember my first meeting with him at the DB Lounge in the Frankfurt train station and it has, since, been a most delightful and significant journey in my life. Stephan's infectious scientific temper, the way he thinks about scientific questions and the wonderfully stimulating atmosphere he creates in the department will remain indelible influences throughout my life. For all the discussions, motivation, for your support and understanding during the hurried thesis writing, for that unforgettable retreat on the sailing boat, and above all, for being a Doktorvater in the truest sense of the word, thank you Stephan!

Prof. Dr. Ralf Seemann has played an invaluable role in my Ph.D. journey. As part of his group I always enjoyed and benefited from the discussions during the group meetings. Together with Prof. Karin Jacobs, he organized winter schools at Feldberg, that were a fun part of my Ph.D. tradition. For your support and guidance, in spite of being in far away Saarbrücken, and in fact at all times, I am very grateful to you Ralf.

My thesis committee members, Prof. Dr. Christoph Schmidt and Prof. Dr. Eberhard Bodenschatz have provided me great feedback about my work. I fondly remember the week at Il Ciocco where I had a great chance to spend considerable time with Prof. Bodenschatz. His feedback about my work and his kind words of advice about my career came at a very timely moment.

I was very fortunate to be a part of the SFB 755 that was led by Prof. Dr. Tim Salditt. I thank him for his enthusiastic organization and discussion during the winter and autumn schools of the SFB where I learnt a lot of new things and many new scientific questions opened up for me. More importantly, I thank him and Dr. Andre Beerlink for the collaboration on the phase contrast imaging project. Tim and I were the 'day time team' at the ESRF during one intense week of measurements and needless to say I learnt a lot working with him. Matthias Bartels and Michael Mell were the remaining members of that collaboration to whom I am very grateful. It was always interesting to work together with Andre on that project and I wish him very well in his career and look forward to a similar successful collaboration in the future.

I met Dr. Geert van den Bogaart at a 2-day methods course that he organized and those 2 days led to 'side project' that lasted many Friday afternoons over 2 years. We did some exciting experiments together, had many great discussions about membrane fusion and life in general and it was always fun! It was a serendipitously wonderful collaboration and has formed a crucial part of my thesis.

I met Dr. Sergio Alonso at the DPG meeting in Regensburg and he ended up doing some beautiful simulations of B–Z droplets. I really look forward to completing that story with him very soon. Sergio was a terrific host to me at Berlin and I look forward to seeing him again soon! Prof. Marcus Hauser has been very encouraging of my work and provided me with a very kind invitation to visit his group at Magdeburg. It was enriching to talk to him about all things BZ and he showed me the delightful world of the plasmodium, where a lot of promise lies. I thank Prof. Holger Stark, Dr. Vasily Zaburdaev, Andreas Zöttl and Max Schmitt, who hosted me in Berlin, and for their inspiring discussions about squirmers. At the very beginning of my thesis, Dr. Jakob Sorensen and Jens Weber at the MPIbpc showed me how to make measurements with a patch clamp amplifier—later, I had many hours of fun, playing with the amplifier!

Monika Teuteberg is a wonderful colleague! Without her help and patience, many things will simply not be possible at the department. My mornings started with her cheery greeting as I walked past her office. It is not the same anymore at the Bunsenstrasse, Monika! Antje Erdmann and Michaela Böttcher have been very kind, efficient and helped me immensely with all the GGNB administration. I thank Udo Krafft and Wolf Keiderling for their technical help during this work. Thomas Eggers, Kris Hantke, and Sibylle Nägle kept the computers and printers and networks running smoothly, with only the finest paper jams.

I have great colleagues and many of them have become good friends, helped us with adjusting to life in Germany and made us feel at home here—Konstantina, Semra, Krish, Venkat, Enkhtuul, Mario, Zeina, Audrey, Shuang, JB, Ciro, Julie, Martin, Jürgen, Thomas, Matthias, Jean-Christophe, Quentin, Sandro, Sonia, Christoph, Max, Jean-Francois, Katherine, Klaus, Siddharth, Pramod, Daniel, Johannes, Marta, Ohle. I especially thank Eric for sharing the 'madness', like only he and I will understand. Thank you all very much for enriching my Ph.D. days. I hope that our paths will cross in the future!

Away from work, many friends have made my time in Göttingen unforgettable. I had many lively weekends and evenings with them. Krish, Venkat, Harish, Shweta, Vimal, and Atul were the first people I met and will remain in my heart always. Spending time with Srinivas was always engaging—I will never forget our violin playing times. Gopal, Soujanya, Swathi, Mayur, Eshwar, Aniket, Sarath, Varun, Sai, Karthik, Bhaskar, Sonia, Anjali, Durga, Raj, Anmol, Ratika, Sridhar, Raunak, and many many more, whose faces I remember but names have faded away, have made it especially memorable for me.

My friends Rajiv Iyer, Umakant Rapol, Kunj Tandon, Ayan Bannerjee, and Shankar Chandrasekharan motivated me greatly toward doing a Ph.D. Guys, here it is. Thank you very much!

Abstract

This book presents experiments on lipid bilayer membranes and nonequilibrium phenomena in active emulsion droplets. In the first part, we outline a concept of self-assembled soft-matter devices based on microfluidics, which use surfactant bilayer membranes as their main building blocks. Membranes form spontaneously when suitable water-in-oil emulsions are forced into microfluidic channels at high-dispersed phase volume fractions and are remarkably stable even when pumped through the microfluidic channel system. Their geometric arrangement is self-assembling, driven by interfacial energy and wetting forces. The ordered membrane arrays thus emerging can be used to build wet electronic circuitry, with the aqueous droplets as the 'solder points'. Furthermore, the membranes can serve as well-controlled coupling media between chemical processes taking place in adjacent droplets as is shown for the well-known Belousov–Zhabotinsky reaction. We also investigate the dynamics of the fusion of vesicles with bilayer membranes. The particular process that we study is the fusion mediated by the SNARE-proteins embedded in the membranes. It is shown that the electrostatic repulsion between the membranes, due to the charged lipids that comprise them, blocks their fusion. Under such conditions, the conformational change of the membrane protein Synaptotagmin-1, under the influence of Ca^{2+} binding, restores membrane fusion. Thus we show in vitro, for the first time, the massive increase in the membrane fusion due to Ca^{2+} triggering, as is the case in vivo. Further, we present a propagation-based X-ray phase contrast imaging to study structure and interfacial properties of ultrathin model membrane systems.

A scheme of active self-propelled liquid microdroplets which closely mimics the locomotion of some protozoal organisms, so-called squirmers, is presented. In contrast to other schemes proposed earlier, it is demonstrated that locomotion paths of the swimmers are not self-avoiding, since the effect of the squirmer on the surrounding medium is weak. Our results suggest that not only the velocity, but also the mode of operation (i.e., the spherical harmonics of the flow field) can be controlled by appropriate variation of parameters. We have studied experimentally the collective behavior of such self-propelling liquid droplets. We find strong polar correlation of the locomotion velocities of neighboring droplets, which point to the formation of ordered rafts. This shows that pronounced textures, beyond what has been seen in simulations so far, may show up in crowds of simple model

squirmers, despite the simplicity of their (purely physical) mutual interaction. As such, the self-propelled droplets are not restricted by the classical equilibrium constraints such as the fluctuation dissipation theorem. We build a correlation ratchet, which relies on a broken detailed balance, to demonstrate a passive rectification scheme of a population of the swimmers. Finally, we study the collective dynamics of a population of swimmers when they are confined to a single dimension, in a setting similar to the well-studied single-file diffusion. It is shown that when the short-time dynamics of the swimmer are ballistic, a transition to a diffusive behavior is seen at the long times and when the short-time dynamics are diffusive, the long-time dynamics follow an anomalous diffusion law, as predicted by theory.

Contents

Publications and Meetings

Publications

(1) *Bilayer membranes in microfluidics: from gel emulsions to soft functional devices*, **S. Thutupalli**, R. Seemann, S. Herminghaus, *Soft Matter*, 2011, 7, 1312–1320.

(2) *Microfluidic scheme to study lipid bilayers*, J-B. Fleury, **S. Thutupalli**, V. Chokkalingam, and R. Seemann, *Proceedings of the 2nd European Conference on Microfluidics* Toulouse, December 8–10, 2010, µFLU10-224.

(3) *Synaptotagmin-1 may be a distance regulator acting upstream of SNARE nucleation*,G v d. Bogaart, **S. Thutupalli**, J. H. Risselada, K. Meyenberg, M. Holt, D. Riedel, U. Diederichsen, S. Herminghaus, H. Grubmuller, R. Jahn, *Nat. Struct. Mol. Biol., 18 (7), 805–812*

(4) *Simple model squirmers with tunable velocity*, **S. Thutupalli**, R. Seemann, S. Herminghaus, *arXiv:1103.5425*, 2011

(5) *Swarming behaviour of simple model squirmers*, **S. Thutupalli**, R. Seemann, S. Herminghaus, *New. J. Phys., 13 (7), 073021*

(6) *Nanoscale Phase Contrast Imaging of Lipid Bilayer Membranes using Hard X-Rays*, A. Beerlink, **S. Thutupalli**, S. Herminghaus, T. Salditt, *Soft Matter 8 (17), 4595–4601*

(7) *Why can artificial membranes be fabricated so rapidly in microfluidics?* **S. Thutupalli**, J-B. Fleury, A. Steinberger, R. Seemann, S. Herminghaus, *Chem. Comm. 49 (14), 1443–1445*

Invited Seminars

2011   Seminar über Nichtlinearität und Unordnung in komplexen Systemen, University of Magdeburg

2010   Cell Biology and Biophysics Unit, European Molecular Biology Laboratory, Heidelberg

2010   Institute for Theoretical Physics, Technical University, Berlin
2010   Center for Models of Life, Neils Bohr Institute, Copenhagen

Selected Meetings

2011   *APS March Meeting*, Dallas, USA (Talk)
2011   *DPG Spring Meeting*, Dresden (Talk, Poster)
2010   *Nonlinear Dynamics Meeting*, Bayreuth (Poster—Best poster award)
2010   *GRC on Oscillations and Dynamical Instabilities in Chemical Systems*, Italy (Poster)
2010   *DPG Spring Meeting*, Regensburg (Talks)
2009   *European Conference on Molecular Electronics*, Copenhagen, Denmark (Poster)
2009   *DPG Spring Meeting*, Dresden (Talk, Poster)
2008   *DPG Spring Meeting*, Berlin (Poster)

Chapter 1
Introduction

The structural hierarchy, functional complexity and, most importantly, the delicate interplay between the two in complex open systems often lead to intriguing behaviour. In particular, quite unexpected collective phenomena are often observed when many similar units couple with one another, resulting in pattern formation, emergence, broken symmetries, and phase transitions. While some physical systems display spontaneous collective ordering, such realizations are particularly striking in situations when the systems are far from thermal equilibrium. The molecular organization during cell division [1], spatio-temporal patterns due to catalytic reactions at surfaces [2, 3], spontaneous emergence of animal and bird flocks [4], turbulence and cloud formation, cellular growth and organization during morphogenesis [5] are just a few such phenomena spanning various length and time scales.

Indeed, life itself may be viewed as a complex system comprised of interacting self-organizing hierarchical subunits [6, 7]. Though at first glance, cells are simply lipid bilayer compartments containing macromolecules, they are capable of many complex functions such as growth, replication, locomotion and communication (Fig. 1.1). The interplay between functional units and the resulting complex dynamics spans multiple length and time hierarchies. This is evident in Fig. 1.1, which shows a few exemplary processes in a bacterial cell. While the organization of macromolecules within the cell give rise to a set of functions such as growth and replication, the co-ordination of the motion of multiple cells leads to a fascinating organization of the individual cells into a seemingly collective entity. A natural question that arises then is: how is this organization and the emergence of function co-ordinated?

The machinery of life is predominantly comprised of *soft matter* and is maintained off equilibrium by the supply and consumption of energy via suitable chemical means. *Soft matter*, such as proteins, colloids, emulsions and membranes, is characterized by typical interaction energies on the thermal scale ($\sim kT$), such that non-trivial operations are possible preferentially at room temperature, as in biological processes. A few main soft building blocks—lipids, proteins and nucleic acids—constitute biological matter. These building blocks have evolved such that they either self-assemble into a desired structure or function, or can be assembled at the expense of only small
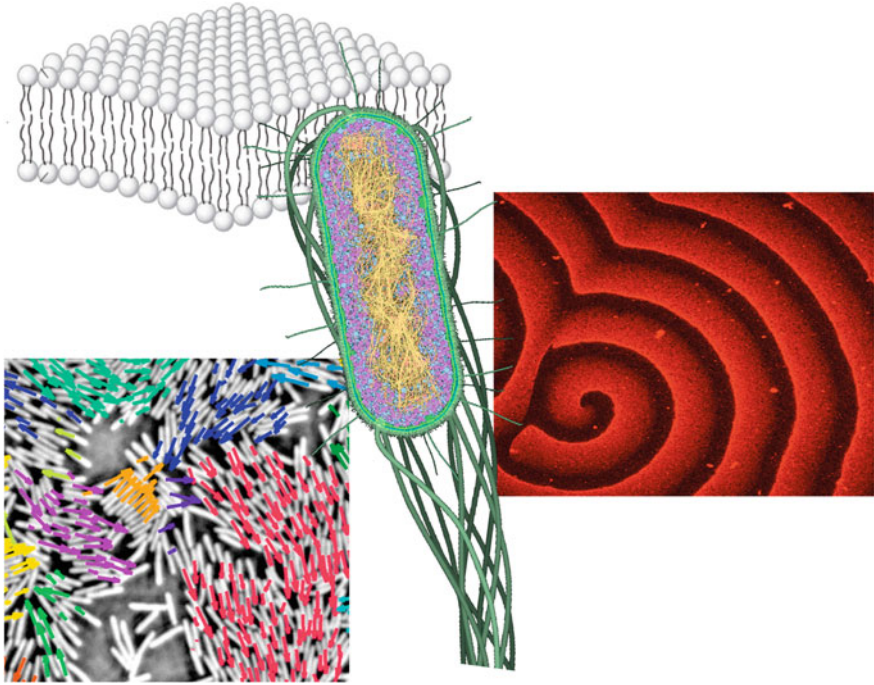
Fig. 1.1 *Center* A cartoon of a cross section through a single bacterial cell. *Clockwise from top* The cell membrane is primarily a lipid bilayer, acting as a scaffold for various proteins. Cytoplasmic bacterial proteins interact with the lipid membranes to self organize, giving rise to functions such as cell division and also a rich variety of patterns [1] Flagellar motors in the cell wall drive bacterial motion and in a group, locomoting cells spontaneously orient in swarming clusters [8] (Figures are adapted with permission from [1, 8, 9])

amounts of free energy. At the same time, chemical energy flux keeps the system sufficiently far off equilibrium to give rise to complex dynamic function, and to maintain the structural components as traits of non-equilibrium steady states. Biological cells, therefore, function as autonomous non-equilibrium soft matter systems. As a result, a physical theory of living matter, based on the principles of soft matter and non-equilibrium physics, seems plausible.

However, a complete description of the emergence of biological (in general, any self-organizing system) structure and function from its microscopic components is a long-standing and so far unsolved problem. Therefore, coarse-grained approaches are more suited and such approaches have led to a wealth of information about various soft matter systems such as granular matter, colloids, emulsions, and membranes. Similarly, significant insights into natural and model dynamical and pattern forming systems such as aggregating amoeba populations [10], the Belousov-Zhabotinsky reaction [11] and Rayleigh-Benard convection [12] have been possible.

Investigations on biological systems and their organization are naturally being inspired by physics based approaches and have followed two broad paths: (1) the application of techniques and methods developed for soft matter and non-equilibrium science to biology [6] and (2) to construct suitable minimal, biomimetic model systems from biological and soft components to test if they are capable of imitating biological function [13].

In the present work, we take the approach of constructing minimal biomimetic systems and the main concerns are investigations on membranes and active emulsions, aspects of both soft matter and non-equilibrium phenomena. We demonstrate that these minimal reconstitutions are already capable of a range of complex behaviour such as nonlinear electric responses, chemical communication and locomotion. The book is organized in two broad parts and the first part, comprising three chapters is about membranes. Demonstrations of soft functional devices based on bilayer membranes in microfluidic channels are described in Chap. 2. The reconstitution of Ca^{2+} triggered membrane fusion in vitro and the electrostatic interactions of the SNARE complex of proteins and lipids are discussed in Chap. 3. An x-ray phase contrast technique for the direct imaging of lipid membranes is then presented in Chap. 4.

The second part is comprised of Chaps. 5–7, on non-equilibrium processes in active emulsions. Chapter 5 is about chemical micro-oscillator droplets and their coupling. An artificial microscopic swimmer and its hydrodynamic flow fields are described in Chap. 6. This is followed by Chap. 8 discussing the various interactions of swimmers that lead to collective dynamics and bound states.

1.1 Membranes

We explore lipid bilayers in the first part. Lipid bilayers are nanoscopic structures that play a very important role in the hierarchical assembly of living systems. Apart from compartmentalising cellular matter, cell membranes are the sites of intense activity concerning the communication between intra- and extra-cellular environments. Transport across the membrane is regulated in multiple ways and can be either passive, i.e, occurring without the input of cellular energy, or active, requiring the cell to expend energy in transportation. The process of photosynthesis exemplifies both passive and active transport in cells, (upper panel of Fig. 1.2) in which single molecules passively transfer photo generated electrons across lipid bilayers while hydrogen ion gradients are generated by ion pumps that operate by the consumption of adenosine triphosphate (ATP) [14].

These processes are reminiscent of micro and nanotechnological elements, particular electronic devices that have motored the advancement of science and technology in the past few decades. While nature has evolved these systems to be self-assembled and very robust, serious limitations to the present top-down approach of man-made devices are rapidly becoming obvious as downscaling continues [15]. This has led to some intriguing biomimetic approaches (Fig. 1.3) to building self assembled systems
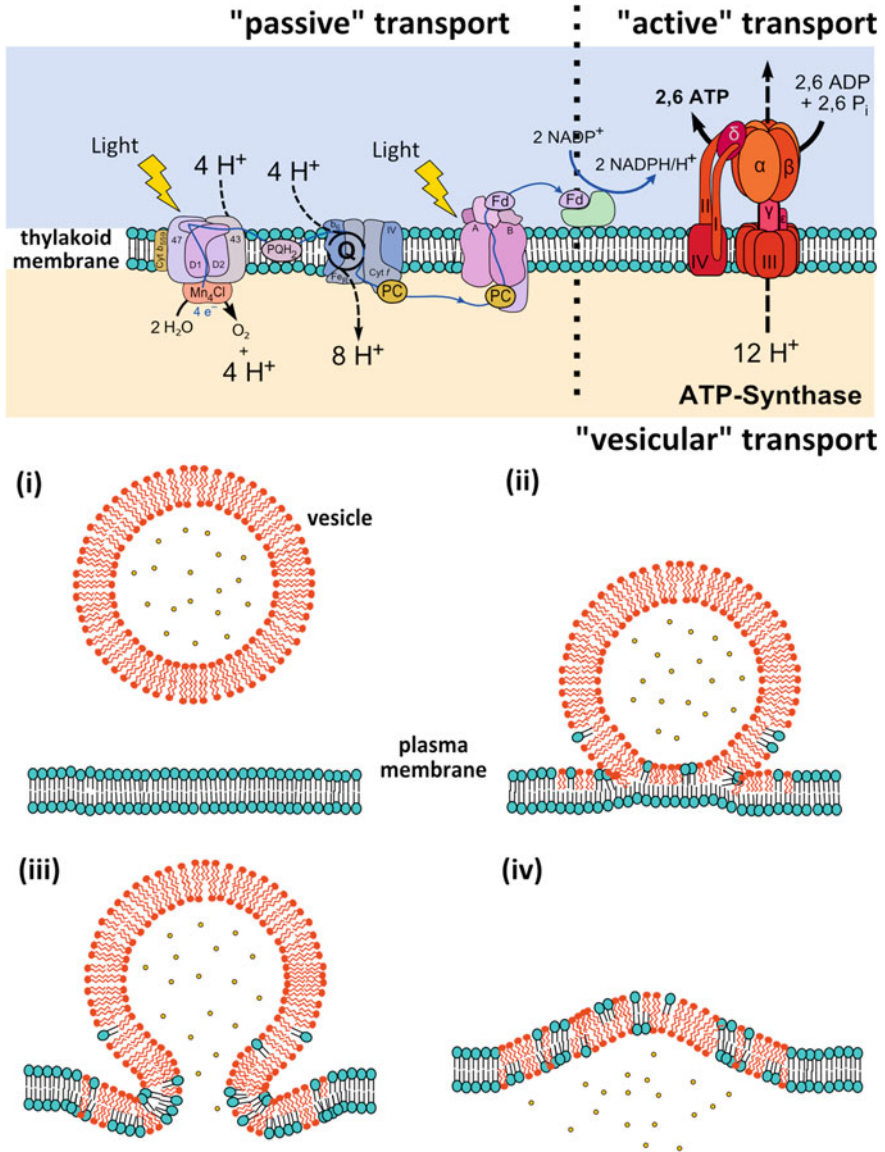
Fig. 1.2 Passive, active and vesicular traffic across membranes *Top* Schematic of electron and proton transport in photosynthesis *Bottom* Biomolecular cargo delivery via (i) fusion of bilayer membranes, which proceeds through various stages such as (ii) docking (iii) pore (stalk) formation and finally (iv) full fusion
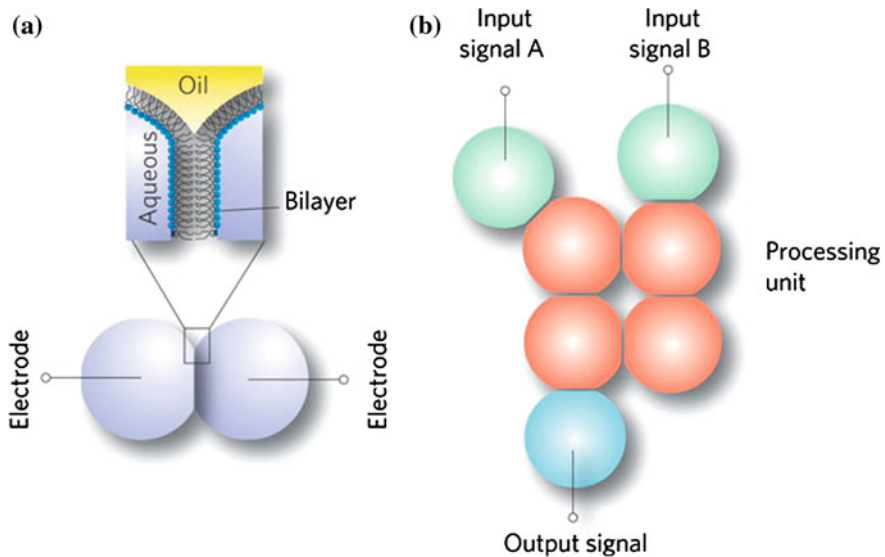
Fig. 1.3 Biomimetic circuits formed using water, oil, lipids and artificial ion pores. **a** The aqueous droplets form electrical 'solder points' and each droplet is connected to its neighbour via a lipid bilayer. **b** Different artificial functional ion pores self insert into the lipid bilayers, providing ionic connectivity in the droplet network

[16–18]. Here, aqueous droplets are immersed in an external oil phase containing lipids such that they are covered by lipid monolayers. One can form networks of such droplets, reminiscent of cellular networks, with the lipid bilayers between the droplets carrying active elements that can form a circuit. In Chap. 2, we extend some of these concepts to creating self assembled soft functional devices, with the lipid bilayer as the fundamental building block.

Another key process of membrane transport, namely, membrane fusion (lower panel of Fig. 1.2), by which small vesicles carrying biomolecular cargo fuse with the plasma membrane to release their contents to either side, is active in processes such as neural signalling. Membrane fusion is a complex physical process since it involves the overcoming of a significant energy barrier ($\sim$40 K_{BT}) for two membranes to fuse. Therefore, in most biological membrane fusion processes, the energy barrier is overcome actively by proteins. Particularly, in synaptic communication in the nervous system, a complex of proteins, known as the SNAREs, coordinate the fusion process. The proteins act like zippers bringing two membranes to fusion, with various triggers such as Ca^{2+}, cascading the processes [19, 20]. In Chap. 3, we study the influence of the electrostatic interactions due to charged lipid membranes in the SNARE-mediated fusion process.

In spite of the great advances in the understanding of both natural and artificial lipid bilayers and their processes, a fundamental limitation still lies in direct imaging of bilayers. Phase contrast microscopy [21] has been instrumental in unravelling

many of the cellular structures and processes. Light microscopy, limited by the diffraction barrier, is however restricted in the amount of structural information one can extract about nanoscopic structures. While there have been advances in breaking the diffraction barrier of light microscopy [22], it is not suitable in all situations. In Chap. 4, we develop phase contrast X-ray microscopy techniques which may potentially prove useful in imaging nanoscopic structures and particularly, in extracting the structural information of lipid bilayers and transport processes such as those described above.

1.2 Active Matter

The second part is about active matter and collective interactions that can occur in nonequilibrium systems. In particular, we use active emulsions as a model active matter system. The term active matter [23, 24] refers to dynamic open systems that constantly alter their state and are able to generate morphological changes, motion and other complex behaviour. An emulsion is a mixture of two or more immiscible liquids such that under appropriate conditions droplets of one liquid can be formed in an external phase of the other. We use microfluidic water-in-oil emulsion droplets with suitable chemical reactions running in the aqueous phase to create chemical micro-oscillators and artificial swimmers. The emulsions are thus rendered active due to the dissipation of chemical energy.

   Spontaneous oscillations and motion represent the simplest examples of complex dynamics and hence are ideally suited for a theoretical analysis of the interactions and dynamic properties of a complex active system. Active oscillators can generate spontaneous oscillations, which continue indefinitely. Spontaneous oscillations occur only in nonlinear dynamic systems that are open i.e. there is a continuous flow of energy through the system from its environment. Among the various types of oscillatory systems such as mechanical pendula, cardiac and neural cells or superconducting Josephson junctions to name just a few, a broad class of them such as chemical and biological oscillators can be categorised as so called reaction-diffusion systems. Systems such as those undergoing catalytic reactions at interfaces, the Belousov Zhabotinsky reaction and social amoeba under stress display spatio-temporal oscillatory patterns such as those shown in Fig. 1.4 which can be described by a reaction-diffusion diffusion mechanism such as

$$
\begin{aligned}
\partial_t u &= D_u \nabla^2 u + f(u, v, k_1), \\
\tau \partial_t v &= D_v \nabla^2 v + g(u, v, k_2)
\end{aligned}
\tag{1.1}
$$

which describes the evolution of the macroscopic variables, such as the concentrations u and v, undergoing reaction, f and g with reaction constants k_1 and k_2, and diffusion with diffusivities D_u and D_v respectively. In the resulting spatio-temporal patterns, the diffusion coefficients D_i ($i = u, v$) set the spatial scales while the rate
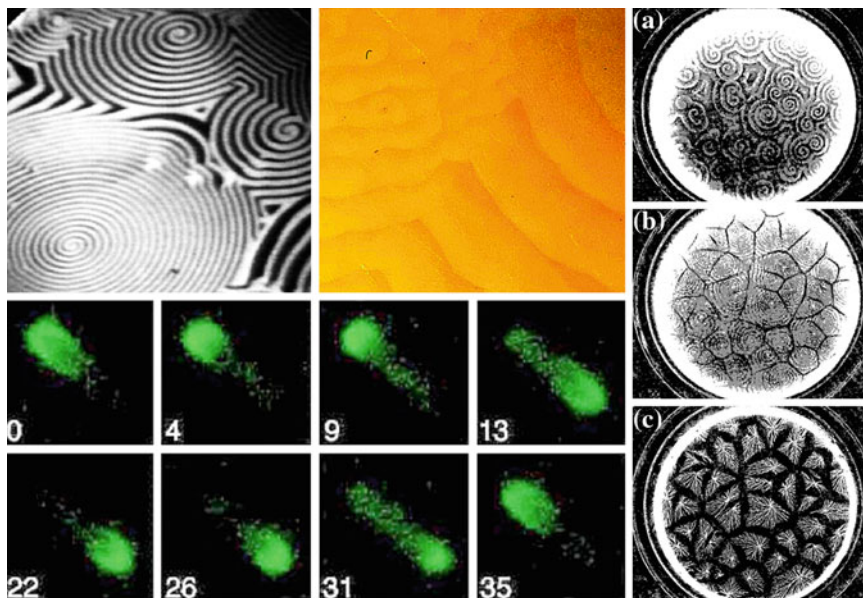
Fig. 1.4 *Clockwise from top left* Spatiotemporal patterns such as spirals and travelling waves in catalytic reactions, the Belousov-Zhabotinsky reaction, aggregating social amoeba and Min-oscillations in bacteria (Images taken from [3, 25])

constants k_i ($i = 1, 2$) set the temporal scale. When the reaction-diffusion dynamics occur in a closed volume such that the confinement is smaller than the typical wavelength of the spatial pattern, the spatial dynamics are suppressed. The closed volume can be considered homogeneous in the diffusive limit and the dynamics within the volume appear as strictly temporal oscillations. We enclose the Belousov-Zhabotinsky (BZ) reaction in emulsion droplets of a few tens to hundreds of microns diameter to form chemical oscillators. In Chap. 5, we describe the properties of these oscillators and their synchronization behaviour mediated by coupling across bilayer membranes as those described in the previous part.

Similarly, co-ordinated motion (swarming) leads to pattern formation of a different type at various length scales as seen in Fig. 1.5. Different kinds of interactions—biochemical, hydrodynamic and volume exclusion—mediate the co-ordination between the movements of various individuals. While in bird and animal flocks there can be visual and olfactory cues, swimming at the microscale is dominated by chemical and hydrodynamic interactions. However, unlike the reaction-diffusion mechanism for oscillators, there are no general principles known, yet, that are applicable in a wide range of swarming behaviour, particularly due to complicated interactions. Therefore, it is important to study the relative roles of the physical and biochemical interactions in isolation. Theoretical studies of such systems have typically abstracted the individual unit, be it bird, beast or microbe, to a point like self propelled particle [23, 29]. This approach of treating flocks as large collections of particles naturally
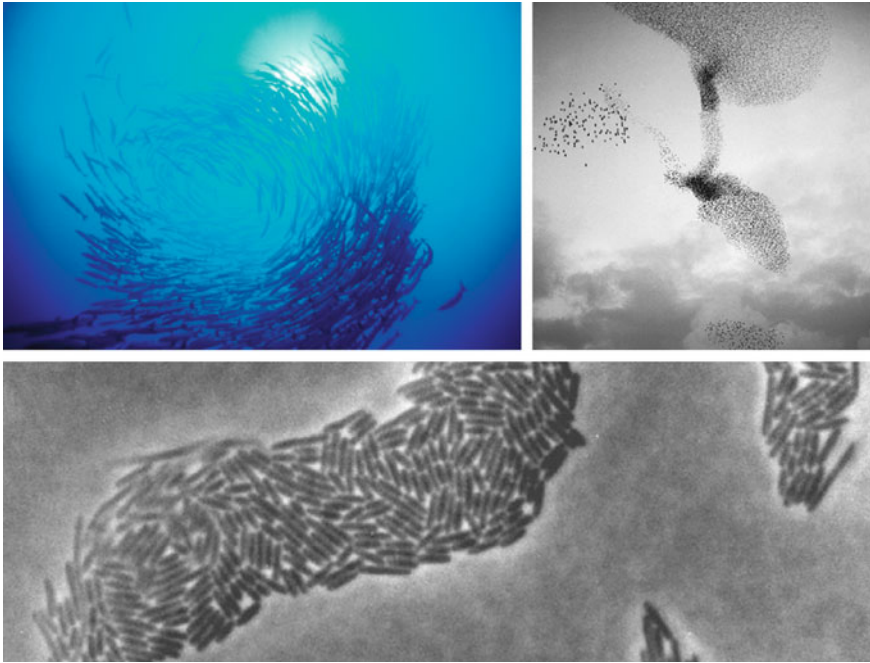
Fig. 1.5 Pattern formation at various scales due to flocking of swimming fish schools, flying starlet populations and gliding bacteria (Images taken from [26–28])

led to the idea of applying the ideas of scaling theories, common in statistical physics, to the description of the collective behavior of populations of organisms [23].

There are strong motivations [30–33] to think that the same patterns of collective motion apply to systems ranging from the molecular to the organismic scales. This suggests that there must be some (still undiscovered) governing dynamics of such systems, from which the above observation follows. Naturally, observations/experiments have to be intimately linked with theoretical modelling for better progress. Indeed, the past few decades, have witnessed an increasing flurry of attempts to both observe and describe flocking as well as simulate the most striking features of natural systems. Current experimental inferences, however, mainly rely on those drawn from biological systems such as those described above. A well characterised and controllable self propelled object would aid greatly is testing some of the theories that are being developed. The self propelled object should not only mimic the main features of natural motion, but also be available in sufficient numbers to draw systematic and statistically relevant conclusions.

In Chap. 6, we investigate swimming at the microscale of an artificial microswimmer made from droplets running the BZ reaction. The interactions in this system are purely physical i.e. hydrodynamic and therefore we probe the hydrodynamic influences on the various collective effects for such swimmers in Chap. 7.

We anticipate that the studies presented in this work will provide a step in the direction of gaining fundamental understanding of complex systems by reconstituting key aspects of their form and function in simple model systems. Further, we foresee that these might also serve as the first technological steps towards synthetic soft functional matter.

References

1. M. Loose, E. Fischer-Friedrich, J. Ries, K. Kruse, P. Schwille, Spatial regulators for bacterial cell division self-organize into surface waves in vitro. Science **320**, 789–792 (2008)
2. V. Gorodetskii, J. Lauterbach, H.H. Rotermund, J.H. Block, G. Ertl, Coupling between adjacent crystal planes in heterogeneous catalysis by propagating reaction-diffusion waves. Nature **370**, 276–279 (1994)
3. S. Nettesheim, a von Oertzen, H.H. Rotermund, G. Ertl, Reaction diffusion patterns in the catalytic co-oxidation on Pt(110): front propagation and spiral waves. J. Chem. Phys. **98**(12), 9977 (1993)
4. M. Nagy, Z. Akos, D. Biro, T. Vicsek, Hierarchical group dynamics in pigeon flocks. Nature **464**, 890–893 (2010)
5. T. Gregor, W. Bialek, R.R. de Ruyter van Steveninck, D.W. Tank, E.F. Wieschaus, Diffusion and scaling during early embryonic pattern formation, in Proceedings of the National Academy of Sciences of the United States of America, vol. 102, Dec. 2005
6. E. Karsenti, Self-organization in cell biology: a brief history. Nat. Rev. Mol. Cell Biol. **9**, 255–262 (2008)
7. H. Meyer-Ortmanns, S. Thurner, *Principles of Evolution from the Planck Epoch to Complex Multicellular Life*. The Frontiers Collection (Springer, New York, 2011)
8. H.P. Zhang, A. Be'er, E. Florin, H.L. Swinney, Collective motion and density fluctuations in bacterial colonies. Proc. Nat. Acad. Sci. **107**(31), 13626–13630 (2010)
9. D.S. Goodsell, *The Machinery of Life* (Springer New York, New York, 2009)
10. T. Gregor, K. Fujimoto, N. Masaki, S. Sawai, The onset of collective behavior in social amoebae. Science **328**, 1021–1025 (2010)
11. I.R. Epstein, J.A. Pojman, *An Introduction to Nonlinear Chemical Dynamics: Oscillations, Waves, Patterns, and Chaos* (Oxford University Press, USA, 1998)
12. K.E. Daniels, O. Brausch, W. Pesch, E. Bodenschatz, Competition and bistability of ordered undulations and undulation chaos in inclined layer convection. Int. J. Fluid Mech. **597**, 261–282 (2008)
13. M. Loose, P. Schwille, Biomimetic membrane systems to study cellular organization. J. Struct. Biol. **168**, 143–151 (2009)
14. G. Karp, *Cell and Molecular Biology: Concepts and Experiments* (John Wiley, New York, 2008)
15. G.E. Moore, Cramming more components onto integrated circuits. Proc. IEEE **86**, 82–85 (1998)
16. W. Hwang, M. Holden, S. White, H. Bayley, Electrical behavior of droplet interface bilayer networks: experimental analysis and modeling. J. Am. Chem. Soc. **129**, 11854–11864 (2007)
17. M.A. Holden, D. Needham, H. Bayley, Functional bionetworks from nanoliter water droplets. J. Am. Chem. Soc. **129**, 8650–8655 (2007)
18. A.J. Heron, J.R. Thompson, A.E. Mason, M.I. Wallace, Direct detection of membrane channels from gels using water-in-oil droplet bilayers. J. Am. Chem. Soc. **129**(51), 16042–16047 (2007)
19. A.T. Brunger, K. Weninger, M. Bowen, S. Chu, Single-molecule studies of the neuronal SNARE fusion machinery. Annu. Rev. Biochem. **78**, 903–928 (2009)
20. R. Jahn, R.H. Scheller, SNAREs-engines for membrane fusion. Nat. Rev. Mol. Cell Biol. **7**, 631-643 (2006)

21. A.H. Bennett, H. Osterberg, H. Jupnik, O.W. Richards, *Phase Microscopy* (John Wiley & Sons, New York, 1951)
22. S.W. Hell, Far-field optical nanoscopy. Science **316**, 1153–1158 (2007)
23. S. Ramaswamy, The mechanics and statistics of active matter. Ann. Rev. Condens. Matter Phys. **1**, 323–345 (2010)
24. K. Kruse, F. Jülicher, Oscillations in cell biology. Curr. Opin. Cell Biol. **17**, 239-342 (2005)
25. N. Kleckner, Mesoscale spatial patterning in the Escherichia coli min system: reaction-diffusion versus mechanical communication. Proc. Nat. Acad. Sci. **107**, 8053–8054 (2010)
26. Philip twu's research. http://www.prism.gatech.edu/~ptwu3/research.html
27. R.M. Harshey, Bacterial motility on a surface: many ways to a common goal. Annu. Rev. Microbiol. **57**, 249–273 (2003)
28. Murmur - today and tomorrow. http://www.todayandtomorrow.net/2009/02/02/murmur/
29. J. Toner, Y. Tu, S. Ramaswamy, Hydrodynamics and phases of flocks. Ann. Phys. **318**, 170–244 (2005)
30. K. Bhattacharya, T. Vicsek, Collective decision making in cohesive flocks. New J. Phys. **12**, 093019 (2010)
31. V. Schaller, C. Weber, C. Semmrich, E. Frey, A.R. Bausch, Polar patterns of driven filaments. Nature **467**(7311), 73–77 (2010)
32. V. Guttal, I.D. Couzin, Social interactions, information use, and the evolution of collective migration. Proc. Nat. Acad. Sci. **107**(37), 16172–16177 (2010)
33. P. Romanczuk, I.D. Couzin, L. Schimansky-Geier, Collective motion due to individual escape and pursuit response. Phys. Rev. Lett. **102**, 010602 (2009)

Chapter 2
Microfluidic Membrane Networks

A concept of self-assembled soft matter devices based on micro-fluidics, which use surfactant bilayer membranes as their main building blocks, arrested in geometric structures provided by top-down lithography, is outlined.

2.1 Introduction

The miniaturization of technical components and machines has been one of the most powerful motors of advancement in both science and technology for the past four decades. Feature sizes in modern electronic circuits have come down to the scale of 45 nm, and single transistors are meanwhile routinely made smaller than 100 nm [1]. As a consequence, the density of components placed on micro-chips has seen a roughly exponential increase over many years. This development, which for its practical robustness has received the colloquial term 'Moore's law', is at the heart of, the enormous recent increase of widely available computer power [2]. All this has been reached by means of 'top-down' lithographic techniques, which are capable of structuring solid state materials into arbitrary shapes with amazing accuracy by sophisticated lithographic procedures.

However, it is clear that there will soon be an end to this development of ever smaller structuring. Well before the structures come of molecular size ($\sim$1 nm), interfacial diffusion will lead to their rapid destruction. Other transport processes directly linked to the function of the device, such as electro-migration in electronic chips, are even much more effective. Since the lithographic approach necessarily leads to a structure which is very far from thermal equilibrium, this must be seen as

a fundamental problem to the top-down concept. The large interfacial energy stored in these systems directly drives transport phenomena which are likely to lead to their destruction. Building devices with feature sizes even close to molecular scales therefore appears prohibitively difficult in a top-down approach. Any successful concept for exploiting the full scale down to molecular sizes would have to master the balancing act of stepping far enough out of equilibrium to make sustained dynamical functions possible, but staying close enough to equilibrium to avoid the destructive force of large gradients in free energy.

Yet we know that such systems exist abundantly on earth: all living matter has dynamic functional units on a hierarchy of length scales, down to molecular size. This has been possible only because evolution has used more than three billion years of genotype experience to master the key task posed above on the phenotype level. The building blocks, chiefly lipids, proteins, and nucleic acids, are designed such that they either self-assemble into the desired structure or function, or can be assembled at the expense of only small amounts of free energy, such as in the case of chaperonins assembling the 'correct' tertiary structure of proteins [3]. At the same time, chemical energy supply keeps the system sufficiently far off equilibrium to give rise to complex dynamic function, and to maintain structural components as traits of non-equilibrium steady states [4]. If we are to build devices with building blocks of molecular size, it therefore appears advisable to follow a similar path exploiting the self-assembly concept [5–8].

It suggests itself to use components similar to those which have been so successfully 'tested' by nature for eons. Soft matter, such as the materials of living systems, is governed by typical interaction energies on the thermal scale ($\sim$ few kT), such that non-trivial functions are possible preferentially at room temperature. It exhibits high molecular mobilities as compared to classical solid state materials, like semiconductors, thus enabling sufficiently rapid self-assembly (and re-assembly) processes. Furthermore, the dispersion interactions dominating the structure and dynamics of soft matter systems are small compared to chemical binding energies. As a consequence, all molecules taking actively part in the functional processes stay intact. This opens an almost unlimited variety of building blocks. Finally, the use of building blocks similar to those of living matter appears particularly promising for devices to be interfaced with living organisms, such as for modern orthotic or prosthetic technology.

However, we cannot rely entirely on self-assembly, since the goal of any design is to reach a certain 'phenotype', the idea of which is at the start of the whole endeavor. Coding the full complexity of the desired device into the molecular building blocks, such that the desired structure emerges completely out of self-assembly, would require full control of non-equilibrium states out of their microscopic conditions; this is a long-standing and so far unsolved problem. Even if a solution was at hand, the task would be still tremendous, and probably impossible to complete. It will thus be necessary to provide a sufficiently strict pre-selection of configurations which are 'allowed' to the system for its assembly. A conceptually straightforward implementation of such pre-selection is some solid scaffold, which provides enough
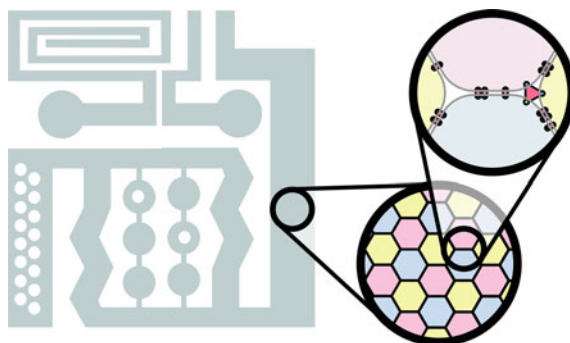
Fig. 2.1 Sketch of a concept combining top-down lithographic design of liquid channel structures (*left*, *grey* pattern) with complex gel emulsions forming self-assembled droplet and membrane arrangements within these channels (*right*, shown in a two-step magnifying glass style to bridge the differences in length scales). The active components can be amphiphilic molecules or complexes residing in the bilayer membranes forming between adjacent droplets, and carefully chosen contents of the droplets themselves

of the desired geometry to subtly 'convince' the soft components to assemble the way one would like them to as envisaged in Fig. 2.1.

The concept which thus emerges, and on which we will dwell in the present chapter, is as follows. We create a system of microfluidic channels, compartments, posts, orifices and so on, on length scales which are well manageable by conventional top-down lithography. This system is then filled with soft molecular materials, which self-assemble within the prescribed geometry, forming well-defined structures down to much smaller scales. To be more explicit, we envisage the use of monodisperse water-in-oil emulsions, with a small volume fraction of the oil phase and a suitable surfactant (e.g., a lipid) for stabilization. This type of emulsions, where the continuous phase is very dilute, are commonly called gel-emulsions [9]. In an externally predefined channel geometry, the water droplets will form well-oriented crystalline arrangements [10, 11]. Under suitable conditions, the interfaces of every two adjacent droplets will form molecular surfactant bilayers. These can serve, by means of dispersion forces and wetting, as nanoscopic tweezers for holding active components, such as ion channels or smaller molecules with non-trivial electronic properties. For molecular electronic circuitry, the water droplets take the role of the 'solder points'.

It is thus inherent to the concept outlined above that we are using self-assembly processes on two completely different scales: the scale of the droplets within the prescribed geometry of the micro-fluidic channel structures, and the nanoscopic scale of the membrane thickness and the functional molecular building blocks. On both scales, self-assembly is then purely driven by wetting forces. As will be discussed below, these forces can not only be used for maintaining certain membrane structures, but also for their controlled manipulation.

Clearly, there won't be any gain over conventional 'top-down' devices unless the self-assembled soft matter structures attain length scales below 50 nm or so. In the present study, we still keep far away from this scale, in order to facilitate the production and observation of the structures and processes at this very preliminary stage. The present chapter rather aims at identifying basic mechanisms and conceptional elements which appear promising, but are still to be scaled down considerably. It should be noted, however, that one of the major potential problems of the concept, the instability of emulsions against coalescence, has been found to fade away as size is reduced. Some results pointing in this direction will be briefly discussed.

2.2 Experimental Techniques

A few key notes about the microfluidic setup (Fig. 2.2) used for the experiments in this chapter are presented here. Microfluidic step emulsification devices [12, 13], formed in poly-dimethyl-siloxane (PDMS, Dow Chemicals) by standard soft lithographic techniques, are used with an inverted fluorescence microscope (Olympus, IX81). Flow through the microfluidic devices are controlled by home built syringe pumps. Electrodes, made from glass micropipettes are used to electrically connect the microfluidic device to a patch clamp amplifier (HEKA, EPC10), which is used to both excite and measure currents. Micropipettes are pulled using a micropipette pulle (Sutter Instruments) from borosilicate glass capillaries with an outer diameter of 1 mm and inner diameters of 500 μm. The micropipette tip is then broken to create an opening of $\sim$1μm. The capillary is then filled with an agarose gel (1 wt%) of 150 mM NaCl electrolyte and sealed at the back after the insertion of a chlorided silver wire.

2.2.1 Patch Clamp Amplifier

We use the patch clamp amplifier in a voltage clamp mode, so that a fixed voltage is applied across the membrane. All the currents reported here are due to the resistive contributions of the membrane. The lock-in method, a commonly used technique to measure capacitance C_m, is used to measure the capacitance of the lipid bilayer. Briefly, a sinusoidal wave excitation $V_m(t)$ is applied across the membrane and the current response I_m is measured. The membrane is excited by a sinusoidal voltage

$$V_m(t) = V_0\sin(\omega t) \tag{2.1}$$

with an angular frequency ω. The response of a membrane system consists of a resistive current $I_R = V_m(t)/R_m$, as well as a capacitive current $I_C = C_m dV_m(t)/dt$. At the peak of the sine wave, where $dV_m(t)/dt = 0$, only a resistive current is obtained and R_m can be derived. The contributions to R_m from electrodes and buffer
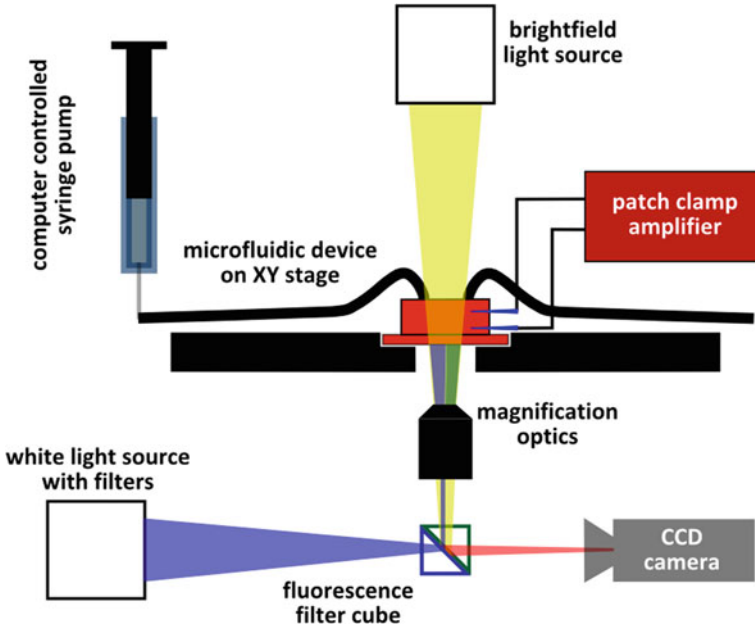
Fig. 2.2 A patch clamp amplifier is integrated to a microfluidics station on inverted microscope to make electrical recordings in microfluidic devices

solution can be corrected for out immediately. At the inflection points of the sine wave, where $V_m(t) = 0$, only I_C is measured and by using the derivative of Eq. 2.1 we obtain:

$$I_C = C_m dVm(t)/dt = C_m \omega V_0 \cos(\omega t) \tag{2.2}$$

From knowledge of the experimental parameters, ω, I_C and V_0, the membrane capacitance C_m is calculated.

2.3 Results

It has been recognized long ago that for micro-fluidics to unfold its full power, it is advantageous to use two immiscible liquids as the working medium instead of a single liquid phase [14]. Not only can isolated droplets immersed in a continuous liquid be used as compartments for controlled reactions [15], but the complex interplay of the liquid/liquid interface with the channel geometry and hydrodynamic pressure gradients gives rise to an abundance of effects which can be harnessed into the engineering of functional devices. So far, this has been mainly limited to the use of isolated aqueous droplets in an oily continuous phase, as containers for chemical, biochemical, or biological processes. In these devices, the droplets are transported

within the channel mainly due to their hydrodynamic drag in the surrounding oil
phase. Contact between adjacent droplets was not desired, in an effort to keep droplet
coalescence and other cross-talk effects to a minimum.

The situation becomes completely different if the volume fraction of the oil phase
is reduced such that droplets maintain mutual contact throughout. The transport of
the droplets in the device is then not anymore determined by the streamlines of the
oil phase, but by the (dynamically varying) geometry of optimum packing of the
droplets within the channel geometry [12, 16]. In fact, the arrangement of spherical
droplets has been reported to change from random to crystalline as their volume
fraction becomes large. In a square channel with a lateral dimension of about four
droplet diameters, a volume fraction of 0.75 shows a crystalline order, while a random
arrangement is observed at 0.55 [12].

It is clear that this opens up qualitatively new possibilities of droplet manipulation.
In particular, the existence of several meta-stable configurations gives rise to strong
hysteresis effects in the droplet geometry. Droplet motion may thus not be reversible,
and become strongly history dependent. If the droplets are all of the same size, i.e.,
if a mono-disperse gel emulsion is used, these effects can in principle be exploited
to dynamically access a large variety of droplet configurations in the device [10, 11,
17, 18]. Furthermore, these configurations are geometrically rather stable, because
the wetting forces determining the angles of contact of the oil lamellae spanning
between the droplets, give rise to substantial energy barriers for any spontaneous
rearrangement.

A simple example is displayed in Fig. 2.3, which shows regular configurations of
droplets with different content. We used squalane with 15 mg/ml of 1,2-diphytanoyl-
sn-glycero-3-phosphocholine (DPhyC, Avanti Polar Lipids) plus 15 mg/ml of
cholesterol as the oil phase, which enters the emulsification unit [13] from the left.
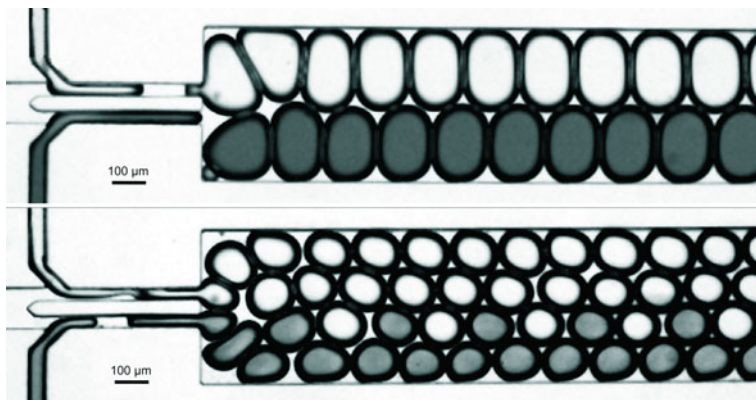
Fig. 2.3 Gel emulsions of water in oil generated by step emulsification, forming rafts in a wider
channel. The channel width is 500 μm, the volume fraction of the aqueous phase is 0.75. The elemen-
tary cells of such rafts can be quite complex, as the lower example shows. Controlled rearrangement
of these configurations are possible by appropriately chosen channel geometries [12, 18, 20]

For coloring the aqueous phase injected in the lower side channel, we used 2 mM DPhyPC doped with 2 molar % of 1,2-dioleoyl-sn-glycero-3-phosphoethanolamine-*N*-(carboxy fluorescein) in the upper picture, and 1,2-dipalmitoyl-sn-glycero-3-phosphoethanolamine-*N*-(lissamine rhodamine B sulfonyl) (both dyes from Avanti Polar Lipids) in the lower picture. The dye lipid was sonicated in the aqueous phase to create liposomes. We see that the droplets form a periodic structure with an 'elementary cell' withstanding transport along the channel. The relative positions of the droplets within the arrangement are fixed, as is obvious due to the droplet color.

Most of the results discussed here were obtained with channel dimensions on the order of 100 microns or more, for the sake of simplicity of generating the devices and optical transparency. However, we repeated some of the experiments with channels etched in silicon which were much narrower (down to 20 μm wide). We found that the smaller the droplets and channel dimensions were, the more stable were the membranes. A straightforward explanation is that the Laplace pressure, which scales as the inverse of the droplet radius, sets the energy scale for any disturbance leading to substantial rearrangements of deformations of membranes, and thus potentially to coalescence. Extrapolating this general trend, further down-scaling is expected to yield emulsion structures which are even much more stable. It should be noted that the formation of stable, mono-disperse emulsions with droplet diameters of 50 nm or less is routinely possible by suitable methods [19].

2.3.1 Formation and Stability of Membranes

Spontaneous membrane formation is well known to occur if two surfactant-laden oil/ water interfaces are brought in intimate contact on their lipophilic sides [21]. Recently, this has also been demonstrated with aqueous drops placed on a substrate next to each other in an oil background phase [22, 23]. The stabilization of the oil-water interface is limited by the diffusion of the amphiphiles to the interface. This means that the droplets have to be "pre-stabilized" in the oil phase to obtain sufficient surface coverage before they are brought together to prevent coalescence of the droplets and a destruction of a lipid bilayer. The waiting times for this are on the order of 10's of minutes and the operations are done manually. We found that when there is a flow of the lipids around a stationary aqueous droplet, the surface coverage of the oil-water interface occurs rapidly, thus stabilizing the droplets (Fig. 2.4). It is to be expected that a similar process will occur if droplets are formed in flow within a microfluidic channel, such that the droplets are stable against coalescence almost immediately after formation. Subsequently when a suitable gel emulsion, thus formed in a microfluidic channel, is at sufficiently low continuous phase volume fraction, we expect spontaneous membrane formation. That this is indeed the case is demonstrated in Fig. 2.5. Here we have produced a zig–zag structure of mono-disperse aqueous droplets by step emulsification [13].
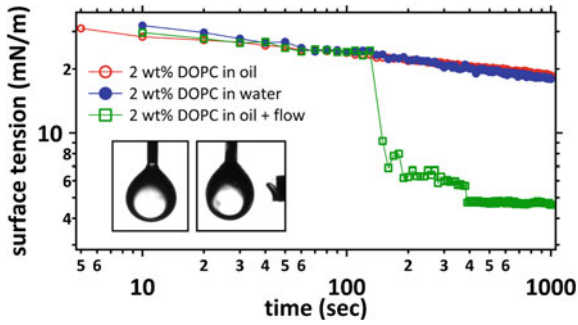
Fig. 2.4 Effect of flow on the evolution of interfacial tension. Data: courtesy of Jean-Baptiste Fleury
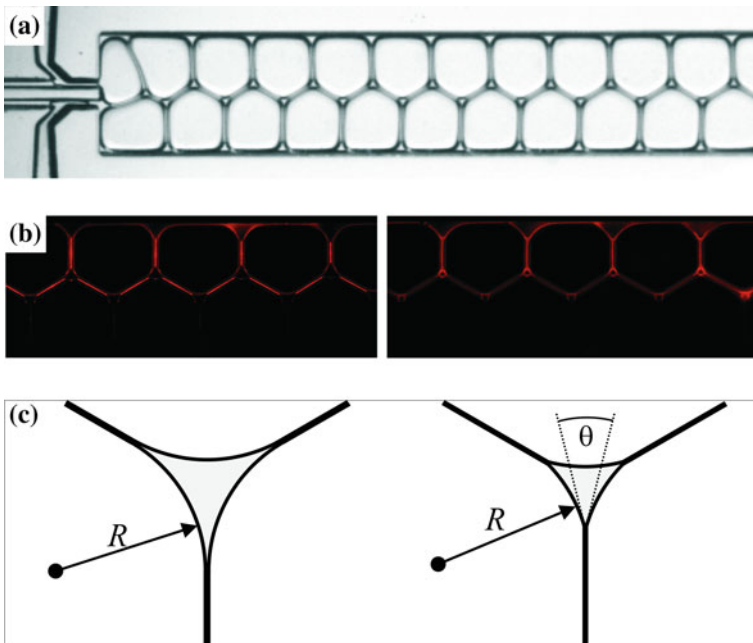
Fig. 2.5 **a** Gel emulsion in a channel (500 μm wide) at very low volume fraction of the continuous oil phase (below 10 %). **b** Micrograph of an emulsion like the one shown in a, taken at the fluorescence wavelength of the dye (di-4-anepps) which was fed into the upper row of droplets. Illumination is by UV light. *Left*: as prepared. *Right*: a few seconds later, when membranes have formed. **c** Geometry of Plateau borders, where three oil lamellae (or membranes) meet at 120°. *Left* as prepared. The droplet surfaces meet tangentially. *Right* after membranes have formed. The contact angle, θ, at the end of each membrane has attained a finite value

   The oil is squalane, with the lipid mono-olein as the surfactant at a concentration of 25 mM, which is well above the critical micelle concentration (CMC). The droplets in the upper row contained a fluorescent dye (di-4-ANEPPS, Invitrogen) which preferentially enters the central lipophilic zone of a lipid bilayer. In Fig. 2.5a, which was taken immediately after the formation of the droplets, bright lines of fluorescence are visible in the oil layers extending between the droplets of the upper row. Fig. 2.5b is taken a few seconds later. Clearly, some of the bright lines have disappeared, indicating the expulsion of the majority of the oil from between the droplets. The transition from the bright line to this faint glow occurs abruptly, and for each oil layer independently. It suggests itself to interpret this transition as the formation of a lipid bilayer separating adjacent aqueous droplets.

   That this is indeed the case is shown in Fig. 2.6. For this experiment, two droplets were used which contained 150 mM/l NaCl in Millipore water, a content similar to those in Fig. 2.5 except for the dye. These were gradually approached, in an oil phase consisting of 25 mM/l mono-olein in squalane, beyond the formation of a contact between their interfaces, such that the latter formed a flat region separating the droplets. After a few seconds, the same abrupt transition was observed as reported in Fig. 2.5. This time the droplets were connected via electrodes to a patch-clamp amplifier, such that the capacitance could be continuously measured. The inset in Fig. 2.6 shows a trace of the sample capacitance for contact formation and subsequent withdrawal. From microscopic inspection of the flattened region of the interface, one can estimate the diameter of that region, and thereby its area. This allows to calculate the specific capacitance of the membrane thus formed. The histogram displayed in the main panel summarizes a series of experiments performed with the same pair of droplets. Clearly, the specific capacitance is well reproducible. The hatched region indicates estimates for a solvent-free membrane of mono-olein, and compares favorably with our results. The slight deviation may be either due to systematic errors in the estimation of the area, or to some residual oil trapped in the membrane formed.

Fig. 2.6 Measurements of the specific capacitance of a bilayer membrane of mono-olein in squalane. The *black* histogram represents the measured values. The *grey* bar indicates the literature values for oil-free mono-olein membranes. *Inset* trace of capacitance measurement upon approach and withdrawal of two droplet surface to/from each other
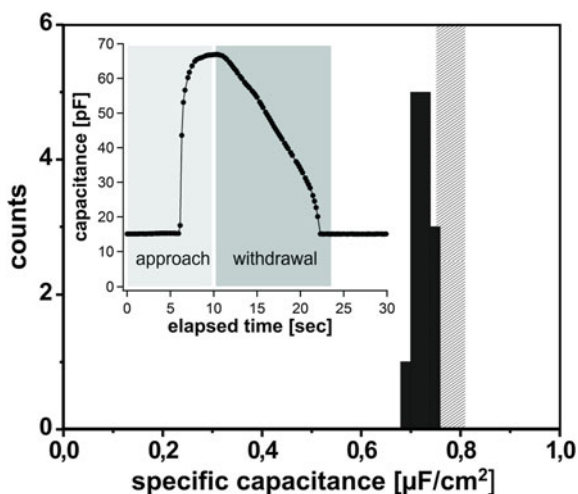
The lines at which three membranes meet, at an angle of 120° at equilibrium, is called a Plateau border [16]. These objects are clearly visible in Fig. 2.5a, b. In the central image, they show up as dark regions surrounded by the lines of glow from the surfactant layers and the oil. It is clear that as long as there is no membrane, the surfactant layers delimiting adjacent droplets will meet tangentially, i.e., at zero contact angle. This is illustrated in Fig. 2.5c, where the grey shaded area corresponds to the dark Plateau border in the fluorescence micrograph. The latter reveals that upon membrane formation, the size of this region shrinks significantly. We can use this effect to determine the contact angle at which the surfactant layers meet the membranes, as illustrated in the bottom panel of Fig. 2.5. For the shaded area, A, one readily finds

$$A = R^2 \left(\sqrt{3} \cos \frac{\theta}{2} + \frac{3}{2}(\theta - \sin \theta) - \frac{\pi}{2} \right) \tag{2.3}$$

The radius of curvature, R, is directly linked to the pressure, p, in the droplet via $p = \gamma / R$, where γ is the free energy per unit area of the surfactant-laden water/oil interface. R can thus be considered to remain unchanged as the membrane forms. It is then easy to obtain the contact angle, θ, from the size of the Plateau borders. We obtain $\theta = 48 \pm 3°$.

At the three-phase contact line, where the membrane meets the adjacent water/oil interfaces, force balance yields

$$\Gamma = 2\gamma \cos \frac{\theta}{2} \tag{2.4}$$

where Γ is the free energy per unit area of the membrane. We can thus directly infer the membrane free energy from inspection of the Plateau borders if γ is known. Using the standard pendant drop method, we obtained $\gamma = 1.77 \pm 0.11 \, \mathrm{mN/m}$. Our result for the membrane free energy is thus $\Gamma = 3.23 \pm 0.20 \, \mathrm{mN/m}$. The formation of the membrane is therefore accompanied by a gain in free energy of $\Delta F = 2\gamma - \Gamma = 0.31 \pm 0.02 \, \mathrm{mN/m}$.

The interfacial free energies involved are of interest for the potential performance of devices designed in the way proposed here. In order to take full advantage of the concept, droplets have to be formed and moved relative to the geometry provided by the micro-fluidic channel structure. The excess free energy of the droplet interfaces sets the scale for the pressures to be applied in these processes. The Laplace pressure is given by $p_L \approx \gamma / l$, where l is the size of the smallest orifice to be passed. For $\gamma = 3 \, \mathrm{mN/m}$, we obtain $p_L = 1$ bar for a 30 nm orifice, which appears well feasible.

As the sharp rise in the capacitance trace shown in the inset of Fig. 2.6 suggests, the formation of the membrane is a rapid process. Figure 2.7a displays a series of images captured with a high speed camera (1000 frames per second, Photron SA 3). The zipper-like transition is clearly discernible, although details on the scale of the membrane thickness are of course not accessible to optical imaging. The total time of formation in this run was about 150 ms. Figure 2.7b shows the membrane diameter as a function of time, as observed during a single formation event. The approximate

Fig. 2.7 Time-resolved
micrograph of membrane
formation in a micro-fluidic
system. *Top* time-lapse images
of three-phase contact line
moving across the oil lamellae
while membrane is form-
ing. The total diameter of
the membrane is 300 μm.
Bottom Three-phase contact
line position as a function of
time. The slope of the *dotted
line* is 1.9 mm/s
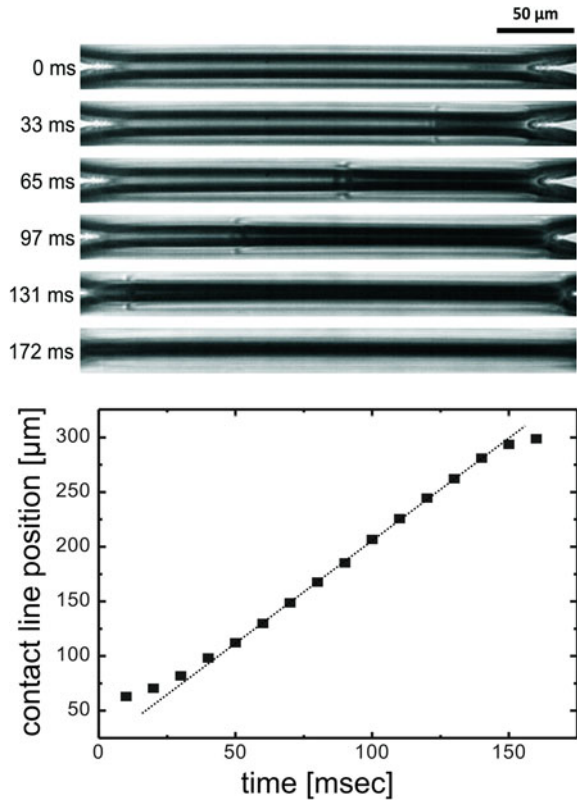
constancy of the contact line velocity (i.e., the first derivative of the diameter with
respect to time) suggests a constant power of dissipation, which is due to the viscous
friction in the vicinity of the edge of the membrane, where the two aqueous phases
and the oil phase meet. More specifically, we can compare the contact line velocity
of about 1.9 mm/s with the capillary velocity, $v_c = \gamma/\eta = 4.1$ cm/s , where η is the
viscosity of the liquid (in this case Squalane which has a viscosity of 43.4 mPa.s). This
is a natural velocity scale for the system, corresponding to the balance of interfacial
and viscous forces. Clearly, the measured contact line velocity is much less than v_c,
which can be attributed to the diverging viscous stress near the three-phase contact
line [24].

For an effective manipulation of the droplet configuration within the micro-fluidic
setup, it may be necessary to move the emulsion through the micro-fluidic device.
This can be done either externally by pressure or volume control (e.g., syringe
pumps), or internally by means of suitable local mechanisms. In any case, it is
of central importance that these manipulation steps do not lead to the destruction
of membranes. One might anticipate that this constraint poses a serious conceptual

Fig. 2.8 Addressing a single
droplet with a pipette
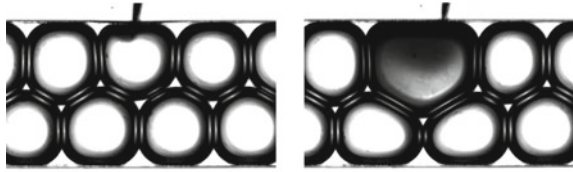
Fig. 2.9 Contacting droplets
(150 mM/l NaCl in Millipore
water) electrically by means of
micro-pipettes poked through
the walls of the PDMS-
micro-device. The pipettes
are equipped as Ag/AgCl$_2$
electrodes and connected to
a patch-clamp amplifier. The
oil phase consists of squalane
plus 25 mM mono-olein. The
channel is 100 μm wide
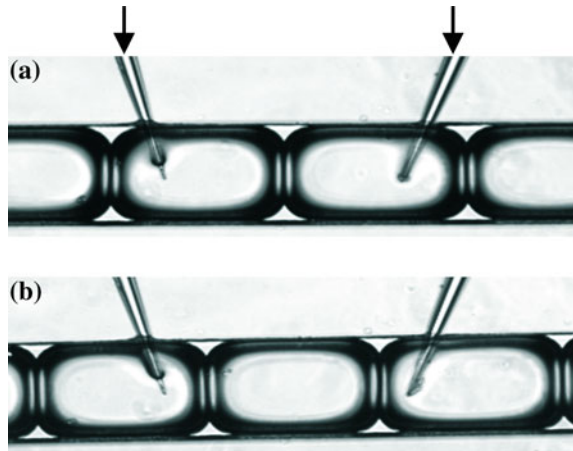
problem, since the membranes are objects of minute thickness (about 4.5 nm in the
case of mono-olein) and relatively small energy of formation (see above).

Quite remarkably, we found the bilayer membranes to be very stable against
mechanical stresses, such as those exerted on them in micro-fluidic flow. A partic-
ularly striking example is shown in Figs. 2.8 and 2.9. Glass micro-pipettes can be
inserted through thin walls (100 μm) created in the PDMS directly into the droplets.
This is important for establishing ohmic contacts to the aqueous droplet content by
means of standard Ag/AgCl$_2$ electrodes, as used in electro-physiology. In order to
isolate the droplets hydrodynamically from the inside of the pipettes, the latter were
filled with Millipore water plus 150 mM/l of NaCl and a small amount of agarose
to form a gel. Electrical contact was established by inserting a 500 μm diameter
Ag wire into the pipette, which was chlorided before electrochemically with 3 M
KCl. The droplets were pumped through the channel at a rate of about three droplets
per second. As seen from Fig. 2.9a, b, the membranes survive their motion past the
inserted glass pipettes: coalescence is not induced. We found that the stability of
the membranes against such mechanical stress depended on the type of intruder.
While the glass pipette electrodes did not seem to affect the membranes in any way,
a tungsten wire (100 μm diameter, sharpened to a 30 μm tip) induced immediate
coalescence.

2.3.2 Electrical Contacts and Characteristics

Let us now turn to the possibility of constructing electrical circuitry out of gel emulsions in micro-fluidic systems. The first thing we have to demonstrate is that the aqueous droplets, which are now to be considered the 'solder points' of potential self-assembled circuits, can be suitably connected to external leads. The setup shown in Fig. 2.9 can indeed be used to measure the electrical properties of the membranes spanned between adjacent droplets. Figure 2.10a shows typical traces obtained upon applying a square wave to a single membrane through the pipettes, which were configured as $Ag/AgCl_2$ electrodes. Both the current and the voltage are recorded using a standard patch clamp amplifier (HEKA, EPC 10). We clearly see the loading current of the membrane capacitance, as well as an ohmic current persisting as long as the voltage is applied.

Fig. 2.10 Electrical properties of mono-olein membranes formed and suspended in a micro-fluidic channel. **a** A square wave voltage is applied (*top*). The current trace (*bottom*) shows distinct peaks indicating the charging current of the membrane capacitance. **b** The small offset observed in the current trace in **a** is plotted as a function of applied voltage. We clearly see an ohmic behavior, which probably stems from ionic impurities
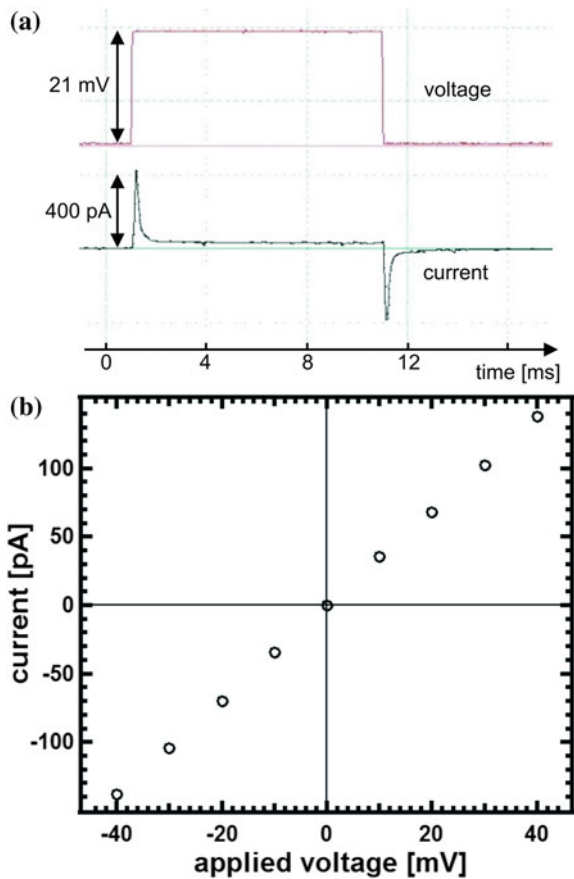
While the capacitive signal is unambiguously due to the membrane capacitance and corresponds to the specific capacitance of about $0.7\,\mu F/cm^2$ (c.f. Fig. 2.6), the ohmic resistance is masked by the resistance of the ionic conductance of the surrounding aqueous solution. Comparing the traces obtained with the configurations displayed if Fig. 2.9a, b, we obtain the 'pure' ohmic characteristic of a single membrane, as displayed in Fig. 2.10b. This conduction is probably due to ionic impurities which are sufficiently lipophilic to cross the membrane [25] in a thermally activated process.

Next we want to demonstrate that the capability of membranes to incorporate active components, as it is well known from experiments in membrane physiology [22, 26], also pertains to the micro-fluidic setting. We have therefore added gramicidin ion pores to the liquid phase in the device, in order to see whether the presence of the channel walls might hamper their performance noticeably. Figure 2.11 shows the current-voltage relationship of a membrane doped with gramicidin A ion pores (Sigma-Aldrich). The gramicidin is added to the aqueous phase at a concentration of $1.1\,\mu M$. Clearly, there is now a dramatically increased conductance of the membrane, which we attribute to the ionic conductivity of the pores. From the unit conductance of the gramicidin A ion pore [27], we estimate the number of pores in our membrane to be in the order of 10^6. Since the membrane is now significantly conducting as compared with the native state, voltages of 500 mV (and even up to 1 V) can easily be applied without rupturing the membrane. In the native state, we found that applied voltages beyond roughly 300 mV ruptured the membrane.

Along with the applied voltage, the width of the applied voltage pulse is also crucial in studying the current/voltage characteristic of a membrane. The result of such an experiment on a native membrane similar to the one described above is displayed in Fig. 2.12. In comparion with the previous experiment (pulse width of 10 ms), here the applied pulse is much shorter and is of 1 ms duration. We observe a clearly defined threshold voltage above which the current rises sharply. We interpret this as reversible electroporation due to electric-field induced formation of nano-scale

Fig. 2.11 Current/voltage characteristic of a mono-olein membrane doped with Gramicidin A ion pores
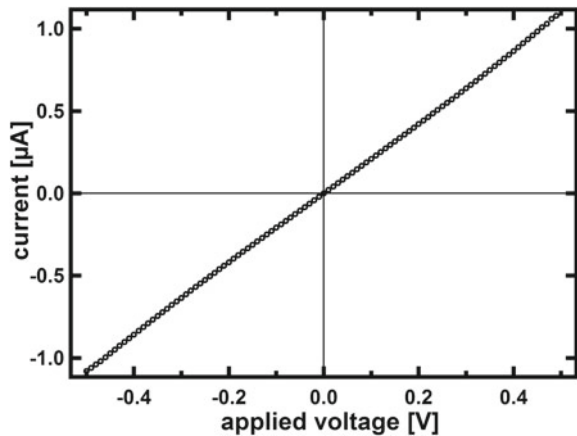
Fig. 2.12 Current/voltage characteristic of a mono-olein membrane. Aside from an ohmic central part, there is a pronounced rise in the current at a threshold voltage of about 500 mV. This is attributed to reversible electroporation. The solid curve corresponds to what would be expected theoretically in that case
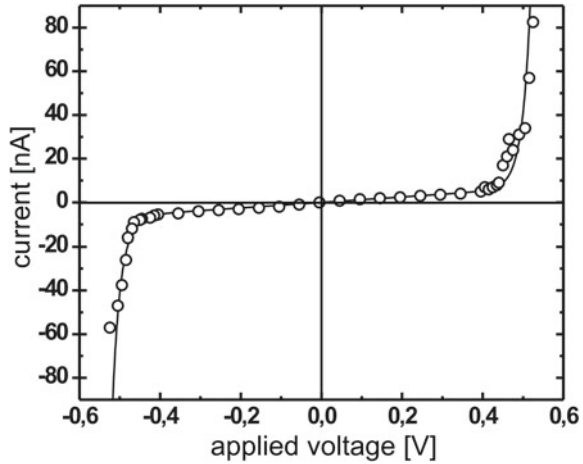
liquid necks within the membrane [28, 29]. Also, it is known from studies on cells that pore formation is favoured when the electric pulses are relative short and typically below 1 ms [30]. The rate of creation of (transient) nano-pores due to the applied electric field is believed to scale as $\exp(U^2/kT)$, where U is the applied voltage [29]. Accordingly, the solid curve has the form

$$I = aU + I_0 \sinh\left(\frac{bU^3}{|U|}\right) \tag{2.5}$$

where a accounts for impurity-induced ohmic conductance. For the constant b, we obtain $49\,kT/V^2$, which is a reasonable value for bilayer membranes [29]. The sharp rise of the current at the critical voltage of about 500 mV shows that the membrane can be used as a voltage stabilization device, similar to a Zener diode, without further manipulation.

2.4 Summary and Outlook

Self assembled surfactant bilayer networks in microfluidic channels may provide a crucial first step towards complex dynamical functions comprising nanoscale or molecular units. More specifically, native surfactant bilayers already offer a range of different electrical behaviour that can be exploited to create wet circuitry. The stability of these objects in micro-fluidic systems is quite encouraging, both in static and in dynamic settings. Their employment as externally controlled scaffolds for synthetic functional molecular units thus appears feasible. The peculiar permeation properties of bilayer membranes for messenger molecules, such as those occuring in systems of chemical oscillators (discussed in Chap. 5), furthermore suggests the

development of multi-functional, self-assembling dynamic nanoscale systems which open up novel types of soft matter technology, which is conceptually influenced by the physical building principles of living matter, but relies on simple components apt to synthesis and thorough control.

Clearly, there is still a long way to go before emulsion-based self-assembled functional systems superior to conventional top-down devices can be produced. This does not only concern the problem of length scales (which appears favorably addressable, as discussed above), but also the question of how to direct many different droplet contents and membrane compounds into the desired patterns. First steps have been undertaken, but the majority of an exciting pathway is still ahead.

References

1. H.S. Bennett, Will future measurement needs of the semiconductor industry be met? J. Res. Natl. Inst. Stand. Technol. **112**, 25–38 (2007)
2. G.E. Moore, Cramming more components onto integrated circuits. Proc. IEEE **86**, 82–85 (1998)
3. G.M. Altschuler, K.R. Willison, Development of free-energy-based models for chaperonin containing TCP-1 mediated folding of actin. J. Royal Soc., Inter. Royal Soc. **5**, 1391–1408 (2008)
4. E. Ben-Jacob, Bacterial self-organization: co-enhancement of complexification and adaptability in a dynamic environment. Philos. Trans. Series A, Math. Phys. Eng. Sci. **361**, 1283–1312 (2003)
5. P. Alivisatos, P.F. Barbara, A.W. Castleman, J. Chang, D.A. Dixon, M.L. Klein, G.L. McLendon, J.S. Miller, M.A. Ratner, P.J. Rossky, S.I. Stupp, M.E. Thompson, From molecules to materials: current trends and future directions. Adv. Mat. **10**(16), 1297–1336 (1998)
6. J.-M. Lehn, Toward self-organization and complex matter. Sci. (New York) **295**, 2400–2403 (2002)
7. D.G. Kurth, P. Lehmann, M. Schütte, A route to hierarchical materials based on complexes of metallosupramolecular polyelectrolytes and amphiphiles. Proc. Nat. Acad. Sci. USA **97**, 5704–5707 (2000)
8. C.M. Drain, Self-organization of self-assembled photonic materials into functional devices: Photo-switched conductors. Proc. Nat. Acad. Sci. **99**, 5178–5182 (2002)
9. B. P. Binks, F. Adams, P. Walstra, B. W. Brooks, H. N. Richmond, *Modern Aspects of Emulsion*. 1st edn. (Royal Society of Chemistry, Cambridge, 1998)
10. P. Garstecki, I. Gitlin, W. DiLuzio, G.M. Whitesides, E. Kumacheva, H.A. Stone, Formation of monodisperse bubbles in a microfluidic flow-focusing device. Appl. Phys. Lett. **85**(13), 2649 (2004)
11. M. Seo, Z. Nie, S. Xu, P.C. Lewis, E. Kumacheva, Microfluidics: from dynamic lattices to periodic arrays of polymer disks. Langmuir: ACS J. Surf. Colloids **21**, 4773–4775 (2005)
12. C. Priest, S. Herminghaus, R. Seemann, Generation of monodisperse gel emulsions in a microfluidic device. Appl. Physi. Lett. **88**(2), 024106 (2006)
13. V. Chokkalingam, S. Herminghaus, R. Seemann, Self-synchronizing pairwise production of monodisperse droplets by microfluidic step emulsification. Appl. Phys. Lett. **93**(25), 254101 (2008)
14. G. M. Whitesides, The origins and the future of microfluidics. Nature **442**, 368–373 (2006)
15. H. Song, D.L. Chen, R.F. Ismagilov, Reactions in droplets in microfluidic channels. Ang. Chem. Int. Ed. **45**, 7336–7356 (2006)
16. W. Drenckhan, S. Cox, G. Delaney, H. Holste, D. Weaire, N. Kern, Rheology of ordered foams: on the way to discrete microfluidics. Colloids Surf. A: Physicochemical Eng. Aspects **263**, 52–64 (2005)

17. M. J. Fuerstman, P. Garstecki, G. M. Whitesides, Coding/decoding and reversibility of droplet trains in microfluidic networks. Science (New York) **315**, 828–32 (2007)
18. E. Surenjav, S. Herminghaus, C. Priest, R. Seemann, Discrete microfluidics: reorganizing droplet arrays at a bend. Appl. Phys. Lett. **95**(15), 154104 (2009)
19. K. Landfester, Miniemulsion polymerization and the structure of polymer and hybrid nanoparticles. Ang. Chem. Int. Eng. **48**, 4488–4507 (2009)
20. E. Surenjav, C. Priest, S. Herminghaus, and R. Seemann, Manipulation of gel emulsions by variable microchannel geometry. Lab. Chip. **9**, 325–30 (2009)
21. O.S. Andersen, Ion movement through gramicidin A channels. Single-channel measurements at very high potentials. Bio. J. **41**, 119–133 (1983)
22. M. A. Holden, D. Needham, H. Bayley, Functional bionetworks from nanoliter water droplets. J. Am. Chem. Soc. **129**, 8650–8655 (2007)
23. A.J. Heron, J.R. Thompson, A.E. Mason, M.I. Wallace, Direct detection of membrane channels from gels using water-in-oil droplet bilayers. J. Am. Chem. Soc. **129**(51), 16042–16047 (2007)
24. E.B. Dussan, On the spreading of liquids on solid surfaces: static and dynamic contact lines. Ann. Rev. Fluid Mech. **11**, 371–400 (1979)
25. J. P. Dilger, R. Benz, Optical and electrical properties of thin monoolein lipid bilayers. J. Membr. Biol. **85**, 181–189 (1985)
26. W. Hwang, M. Holden, S. White, H. Bayley, Electrical behavior of droplet interface bilayer networks: experimental analysis and modeling. J. Am. Chem. Soc. **129**, 11854–11864 (2007)
27. S.B. Hladky, D.A. Haydon, Ion transfer across lipid membranes in the presence of gramicidin A. Biochim. Biophys. Acta (BBA) **274**, 294–312 (1972)
28. J.C. Weaver, Electroporation of biological membranes from multicellular to nano scales. IEEE Trans. Dielectr. Electr. Insul. **10**, 754–768 (2003)
29. Z. Vasilkoski, A. Esser, T. Gowrishankar, J. Weaver, Membrane electroporation: the absolute rate equation and nanosecond time scale pore creation. Phys. Rev. E **74**, 1–12 (2006)
30. T.D. Xie, T.Y. Tsong, Study of mechanisms of electric field-induced DNA transfection III. Biophys. J. **63**, 28–34 (1992)

Chapter 3
Electrostatic Interactions in Membrane Fusion

The role of electrostatic interactions in SNARE-mediated lipid bilayer fusion and the putative function of synaptotagmin-1, the Ca^{2+} trigger of fusion, are investigated.

3.1 Introduction

Presynaptic nerve terminals convert electrical signals into chemical signals that target other neurons or somatic cells. The chemical signalling molecules are contained in synaptic vesicles and the conversion is mediated by a depolarisation of the plasma membrane, which causes an influx of Ca^{2+} through voltage activated Ca^{2+}-channels. The increase of the local cytoplasmic Ca^{2+} concentration triggers the submillisecond fusion of synaptic vesicles with the plasma membrane resulting in neuronal exocytosis i.e. release of neurotransmitters. Membrane fusion is mediated by the assembly of SNARE proteins (Fig. 3.1) including the R-SNARE synaptobrevin-2 on the synaptic vesicle and the Q-SNAREs syntaxin-1A and SNAP-25 on the plasma membrane [1, 2]. SNARE assembly involves the conserved, membrane-adjacent SNARE motifs, proceeds from the N-terminus towards the C-terminal membrane anchors, and results in the formation of a tight coil–coil structure which pulls the membranes together and overcomes the energy barrier of membrane fusion. Though there is no direct evidence, membrane fusion itself is widely speculated to proceed via a sequence of steps involving increased membrane curvation, hemi-fusion i.e. fusion of only the outer lipid leaflet, pore formation and finally complete fusion as shown in the lower panel of Fig. 3.1.
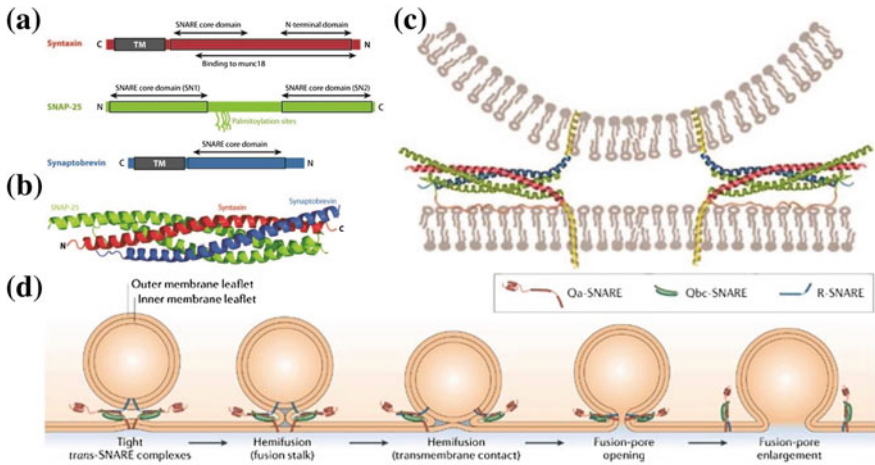
Fig. 3.1 SNARE protein complex and SNARE-mediated membrane fusion. **a** Schematic of the three components of the SNARE complex: Syntaxin, SNAP-25 and Synaptobrevin. Syntaxin and Synaptobrevin have transmembrane domains (TM) at their C terminals. The TM domains embed into the lipid bilayer. SNAP-25 and Syntaxin are present on the plasma membrane. Synaptobrevin is present on the vesicle. **b** The coil–coil structure of the SNARE proteins. The coiling proceeds from the C terminals towards the N terminals. **c** When the proteins coil, the two lipid bilayers of the plasma membrane and the synaptic vesicle are pulled close together. **d** Once the membranes are close enough, the lipid bilayers fuse through a sequence of events such as hemifusion, formation of a fusion pore and finally complete fusion (Figures reproduced with permission from [1, 2])

Another key player in the fusion process is synaptotagmin-1, the Ca^{2+}-trigger for fast exocytosis in neurons. It promotes the interaction of SNARE proteins between the synaptic vesicles and the plasma membrane, which results in membrane fusion and release of neurotransmitter. Synaptotagmin-1 is a 65 kDa integral membrane protein present on synaptic vesicles, which functions as a major Ca^{2+}-sensor for neuronal exocytosis [3, 4]. As shown in the cartoon sketch of Fig. 3.2, it contains a single transmembrane domain followed by a large cytoplasmic domain consisting of a 61 residue unstructured linker and tandem C2-type phospholipid and Ca^{2+}-binding domains. The C2-domains, called the C2A and C2B domain, bind 2 and 3 Ca^{2+} ions, respectively, with low affinity (60 µM–1 mM) [5, 6]. The C2-domains interact with membranes containing anionic lipids and with SNARE proteins. Synaptotagmin-1 can bind to anionic lipids both in the absence of Ca^{2+} via a so-called polybasic patch consisting of four lysines located on the C2B domain [7–9] and in the presence of Ca^{2+} via its Ca^{2+}-binding sites [5, 8–13]. Anionic lipids such as phosphoserine (PS) and phosphatidylinositol 4,5-biphosphate ($Pi(4, 5)P_2$) complete the Ca^{2+}-binding sites of the C2-domains and thereby increase the affinity of synaptotagmin-1 for Ca^{2+}-binding [5, 7, 8, 14].

However, while the zippering process of the SNARE proteins is reasonably well established, the role of synaptotagmin-1 in the membrane fusion process is not fully clear. The exact mechanism by which it acts as a Ca^{2+} trigger is poorly understood. The sequence of events in the membrane fusion is problematic too. If the SNARES
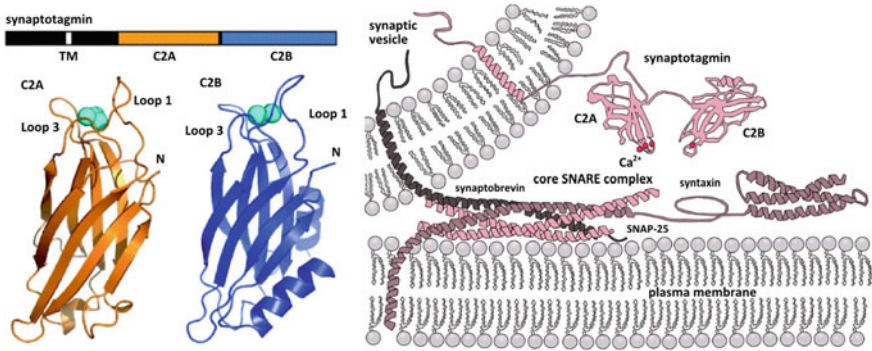
Fig. 3.2 Synaptotagmin-1 is the Ca^{2+} sensor for membrane fusion. *Left* Synaptotagmin has a single transmembrane domain (TM) which embeds into the lipid bilayer of the synaptic vesicle. This is followed by a large cytoplasmic domain, which 'sticks out' into the cytoplasm of the cell. This domain is comprised of two parts the C2A and C2B which have 2 and 3 sites, respectively, for binding Ca^{2+} ions. *Right* By the current understanding of the fusion process, the SNARE proteins are nucleated i.e. they are primed for fusion via coiling but fusion is somehow arrested. In this picture of fusion, the synaptotagmin acts downstream of the SNARE coiling (Reproduced with permission from [15])

are already close enough to zipper even before the Ca^{2+} influx, then membrane fusion should proceed rapidly by the SNARE action. If they are not close enough, then what are the mechanisms by which they stay apart? And how exactly does the interplay of Ca^{2+} and synaptotagmin-1 bring them close enough for fusion to occur rapidly? In this chapter we seek to answer some of these questions. We show that the electrostatic repulsion between the lipid membranes due to their charged lipid components, is sufficient to keep membranes too far apart for fusion to occur. We then show that the conformational change in synaptotagmin-1 due to the binding of Ca^{2+} helps to overcome this electrostatic repulsion, thus bringing the membranes close enough for fusion. First, we present a description of the current understanding of synaptotagmin-1 and its role in membrane fusion.

3.1.1 Current Understanding of the Role of Synaptotagmin-1

Membrane binding of Ca^{2+}-synaptotagmin-1 has recently been proposed to locally increase membrane curvature, suggesting that synaptotagmin-1 might act by increasing the membrane tension at the sites of fusion [16, 17]. Synaptotagmin-1 also binds directly to SNAP-25, syntaxin-1A, and the binary and ternary SNARE complexes [4, 18]. Some of the earlier studies showed that the polybasic patch and the Ca^{2+}-binding sites bind to the SNAREs, but the relevance of this observation was questioned since these are the same regions that bind to lipid membranes [8, 19, 20]. This discrepancy was recently overcome by a single molecule Förster Resonance Energy Transfer (FRET) study showing binding of the C2B domain to the ternary

SNARE complex in an orientation that leaves both the polybasic patch and the Ca^{2+}-binding sites free to interact with the membrane [21, 22]. All together, a model is emerging where synaptotagmin-1 structurally changes both the SNARE complex and the membranes in a Ca^{2+}-dependent manner, thereby levering the protein and/or bending the membrane which induces membrane fusion [3, 9, 11, 16, 17, 21–25]. Importantly, in these models, synaptotagmin-1 acts after SNARE nucleation, i.e. at state where the membranes are already tethered by a trans SNARE-complex in which at least part of the cytoplasmic SNARE domains, but not the C-terminal transmembrane helices, are already coiled up as depicted in the right panel of the cartoon sketch of Fig. 3.2. This is referred to as a fusion-arrested state.

A large number of studies aimed to reconstitute Ca^{2+}-synaptotagmin-1 triggered membrane fusion in vitro used SNARE-containing artificial membranes. Synaptotagmin-1 was then added either in the form of soluble cytoplasmic C2-domains of synaptotagmin-1 (C2AB fragment; residues 97–421) or by inserting full length membrane anchored synaptotagmin-1. A major limitation in these studies is that SNAREs alone are sufficient to induce fusion of liposomes [26]. Indeed, membrane fusion is relatively efficient when artificial membranes, containing even a single copy [27] of synaptobrevin-2 together with a combination of syntaxin-1A and SNAP-25, are allowed to fuse. The addition of the soluble C2AB fragment of synaptotagmin-1 makes membrane fusion somewhat Ca^{2+}-sensitive and results in an increase of fusion efficiency between $100\,\mu M$ and $10\,mM$ Ca^{2+} [3, 10, 11, 16, 17, 23, 24, 28–32]. However, in these studies, membrane fusion still proceeds in the absence of the C2AB fragment and the increase in fusion efficiency upon Ca^{2+}-addition was usually less than 10-fold compared to the over 18,000-fold increase in vivo [33]. Recently, it was reported that fusion in the presence of membrane-anchored synaptotagmin-1 was about 3–5-fold increased at $10\,\mu M$ Ca^{2+} but decreased again at higher concentrations of Ca^{2+} [30], presumably because under these conditions synaptotagmin-1 binds to its own membrane and thus cannot facilitate membrane docking and fusion by interactions with the plasma membrane [28, 30]. The Ca^{2+}-dependency was strongly influenced by the lipid composition of both liposome populations: increasing the fraction of anionic lipids in the Q-SNARE or R-SNARE membranes resulted in higher or lower Ca^{2+}-sensitivities, respectively. Therefore, in spite of its significance, the mechanism by which synaptotagmin-1 promotes this interaction is controversial, and the massive increase in membrane fusion efficiency of Ca^{2+}-synaptotagmin-1 has not yet been reproduced in vitro.

However, it is clear that the interactions of synaptotagmin-1 with membranes and SNAREs are predominantly of an electrostatic, i.e. ionic, nature. Indeed, binding of synaptotagmin-1 both to anionic lipid membranes [5, 7] and to SNARE molecules [21, 22, 25] is heavily influenced by the ionic strength of the solution in which the proteins, vesicles and membranes are present. Thus, it is surprising that the influence of ionic interactions on membrane fusion in the presence of synaptotagmin-1 has not been investigated. All the aforementioned in vitro synaptotagmin-1 membrane fusion studies were performed in solutions which had a relatively high ionic strength of typically 100–150 mM KCl or NaCl in solution. These ionic strengths are a natural choice for the experiments since the in vivo physiological conditions of a cell are

at these ionic strengths. However, at these high salt concentrations the binding of synaptotagmin-1 to SNAREs and anionic membranes is strongly reduced or even absent [5, 7, 21, 22, 25]. Furthermore, these high concentrations potentially screen important electrostatic interactions which might very well be expected due to the charged lipids that are ubiquitously present in membranes.

We sought to address this important issue—what happens when the electrostatic interactions are not screened? We do this by reducing the ionic strength of the buffer solution. When the charges are not screened, the electrostatic interactions due to the charged lipids in the membranes play a very important role, as we will see. In the following sections, we show that under such conditions, in the presence of anionic lipids, SNARE-dependent membrane fusion is completely blocked. Further, we show that the fusion strictly depends on the presence of Ca^{2+} and synaptotagmin-1 when the ionic strength of the medium is reduced. It is then demonstrated that synaptotagmin-1, by regulating the distance between the membranes in a Ca^{2+}-dependent manner, acts even before SNARE nucleation occurs, which is a significant departure from the current understanding of its role.

3.2 Experimental Techniques

In vitro experiments help to understand the minimal model for membrane fusion by controlled trials. A typical assay for studying membrane fusion in vitro is to reconstitute functional proteins in liposomes that are formed by fluorescently tagged lipids. Vesicles containing the complementary fusion proteins are respectively tagged with fluorescent tags that form a FRET pair. When the vesicles are separate, there is no resulting FRET signal due to the large distance between them. However, as the vesicles fuse, their constituent lipids mix in the newly formed membrane, thus bringing them close enough to get a FRET signal. The efficiency of the fusion between the complementary vesicles is then followed by recording the FRET fluorescence signal over time. As the fusion proceeds, the donor fluorescence decreases and the acceptor fluorescence correspondingly increases.

Liposomes with a size in the range of 30–40 nm are prepared using size exclusion chromatography as described extensively [25]. Briefly, Lipids (Avanti, Alabaster, AL) were mixed in chloroform to yield (molar ratios): phosphatidylcholine (5), l phosphatidylethanolamine (2), phosphatidylserine (1), phosphatidylinositol (1), cholesterol (1). After drying, they were resuspended in hybridization buffer (HB100) solution containing 5 % (wt/vol) cholate at a total lipid concentration of 13.5 mM. SNARE-proteins in 1.5 % cholate were added (lipid to protein ratio of 100:1 n/n), followed by chromatography on Sephadex G-50 superfine equilibrated in HB100 buffer by using a sample-to-column volume ratio of 1:30. For the preparation of liposomes containing Synataxin and SNAP-25, the proteins were preincubated for 1 h before addition to the phospholipid mixture.

Q-SNARE population of liposomes contained 1:2,000 (protein:lipid molar ratio) of syntaxin-1A and SNAP-25 and a synaptobrevin-2_{49-96} fragment. R-SNARE population of liposomes contained a 1:1,000 (protein:lipid molar ratio) synaptobrevin-2.
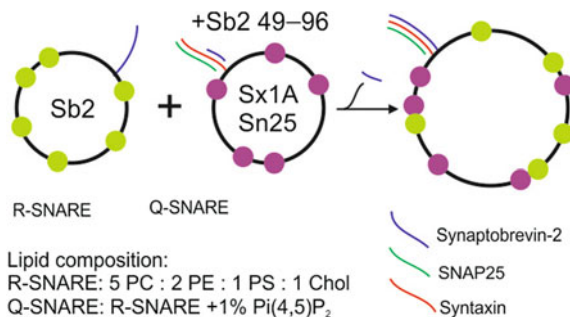
Fig. 3.3 The cartoon sketch above indicates the liposomes conditions used in the experiment. Large *black circles* indicate the liposomes. Sb2 stands for Synaptobrevin2, Sx1A is Syntaxin 1A and Sn25 is SNAP25. The *green* and *purple dots* indicate the *green* donor fluorophore and the *red* acceptor fluorophore, of the FRET pair, respectively. A tiny fragment (residues 49–96) of synaptobrevin-2 is added to the Q-SNAREs to prevent spontaneous fusion. Fusion is then triggered by cleaving this fragment from the Q-SNAREs by the addition of an appropriate enzyme. The lipids and their ratio used in the preparation of the liposomes are shown below. PC, PS, and PE are abbreviations for the lipid head groups. *PC* Phosphatidylcholine, *PS* Phosphatidylserine and *PE* Phosphatidylethanolamine, *Chol* cholesterol

R-SNARE liposomes had a lipid composition of 5:2:1:1 ratio of phosphatidyl-choline (PC), phosphatidylethanolamine (PE), phosphatidylserine (PS) and choles-terol (chol) (all lipids from Avanti Polar Lipids) to mimic the composition of synaptic vesicles. Q-SNARE liposomes mimicking the plasma membrane had the same composition except that $1\,mol\%$ PC was replaced with the plasma membrane lipid $Pi(4, 5)P_2$. Further, the R-SNARE liposomes were labelled with $1.5\,mol\%$ of OG-PE (Invitrogen), the donor fluorophore. $1.5\,mol\%$ 1,1'-dioctadecyl-3,3,3',3'-tetramethylindodicarbocyanine perchlorate (DiD; Invitrogen; emission 670 nm) was chosen as the acceptor fluorophore in the Q-SNARE liposomes.

The synaptobrevin-2_{49-96} fragment in the Q-SNARE population allows us to provide a trigger for the fusion process. As we discussed earlier, a coil-coil structure is formed between the three SNARE proteins which helps the membrane fusion to occur. However, when only a fragment of the synaptobrevin-2 is added, a full coil is not formed, thus preventing fusion to occur. To trigger the fusion between the R and Q-SNARES, an enzyme is added to cleave the synaptobrevin-2_{49-96} fragment such that the full synaptobrevin-2 from the R-SNARE can complete the SNARE coil and fusion proceeds normally. A schematic of this process is shown in Fig. 3.3. This schematic is shown in the experimental section together with the data to show the precise conditions used for that particular experiment.

3.2.1 Microfluidic Assay for Liposome Fusion

Typically in vitro experiments for fusion studies are performed in a cuvette, with sample volumes in the range of a few milliliters. While a small sample size is crucial for experiments involving purified synaptic vesicles, a further disadvantage of the

"bulk" measurements is the lack of easy integration of a triggered release of Ca^{2+}. Therefore, in conjunction with experiments performed in a cuvette, a microfluidic technique was developed for the investigation of the Ca^{2+} triggered SNARE fusion.

Microfluidic techniques offer the advantage of reduced sample volume and controlled mixing of fluids. Microfluidic devices are made using standard photolithographic techniques as described in the appendix. Two CCD cameras with appropriate optical filters were integrated with an inverted microscope (Olympus, IX81) as shown in Fig. 3.4 as a means to measure FRET efficiency. A microfluidic device is mounted on an X-Y stage and the donor fluorescence is excited by the appropriate use of an optical filter (480 nm) and the resulting images from the donor (540 nm) and acceptor (610 nm) fluorescence are simultaneously recorded in two separate CCD cameras (PCO 1200).
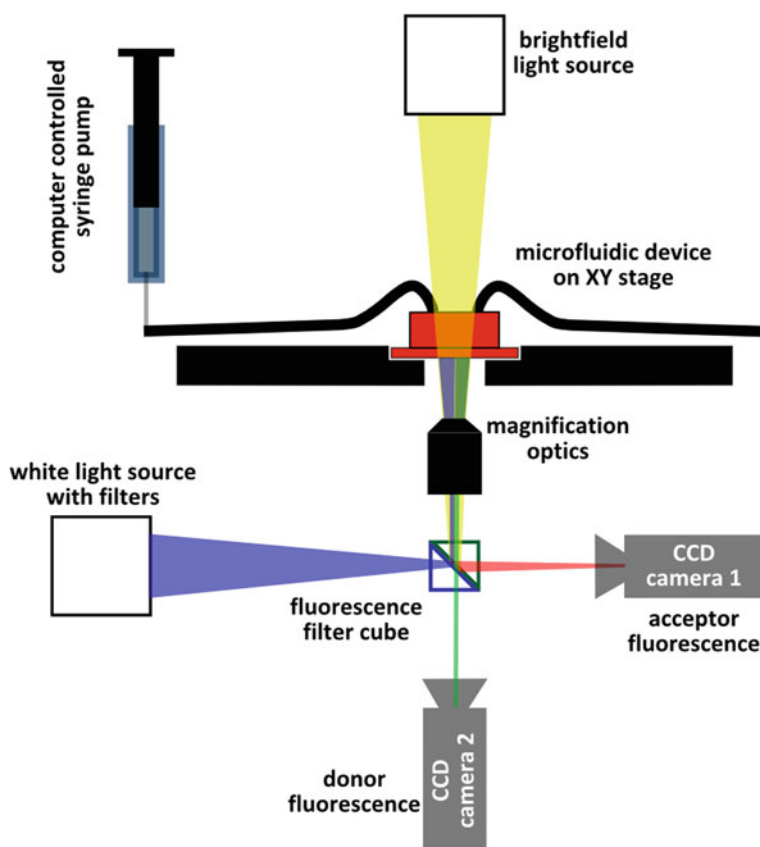
Fig. 3.4 Experimental setup for performing microfluidic FRET experiments to study membrane fusion. A microfluidic device made using PDMS soft lithography is mounted on an inverted microscope. The flow through the device is regulated by computer controlled syringe pumps. The FRET fluorescence is recorded on two seperate CCD cameras, one for the donor and the other for the acceptor fluorescence wavelengths respectively. The donor fluorescence is excited by using filtered light from a white light source
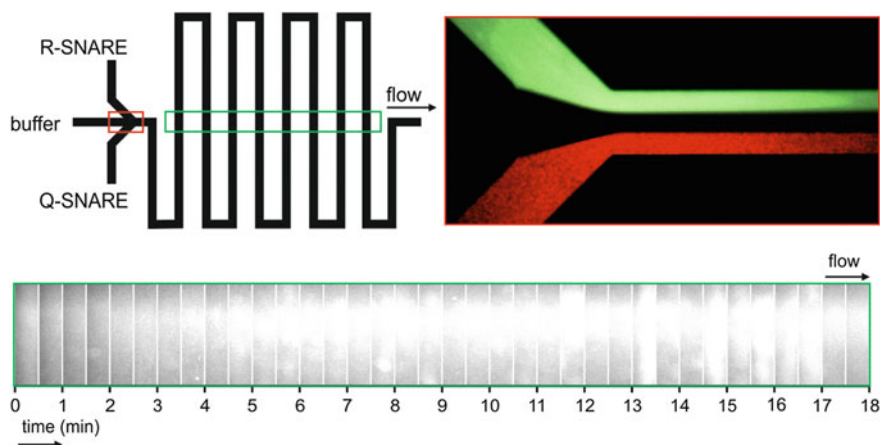
Fig. 3.5 Channel geometry of a microfluidic device for membrane fusion. *Top left* It consists of a cross geometry when the two SNARE populations are mixed. *Top right* Mixing of SNARE liposome populations is achieved by hydrodynamic flow focussing. *Bottom* Images of the acceptor flourescence in the different turn segments of the channel are recorded as shown. The fusion is monitored by recording the average intensity of each time window. It can be clearly seen that as time proceeds (i.e. in the direction of the flow), the brightness of the images increases. This is due to the increase in the FRET signal that follows the fusion event

A microfluidic device geometry as shown in the top left panel of Fig. 3.5 is used to mix the two SNARE populations on the chip. A cross channel geometry where flow can be focussed is a well known method to provide controlled mixing on a microfluidic chip as shown in the top right panel of Fig. 3.5. The well controlled flow rates in the channel can be used to provide a precise calibration of time along the length of the channel, i.e., the length along the channel at which the two SNARE populations first come into contact is regarded as $t = 0$ and time proceeds linearly along the channel length. Therefore one can take snapshots of the fluorescence intensity at various points along the length of the channel as shown in the bottom panel of Fig. 3.5. When the intensity of the recorded images is plotted as a function of the length of the channel i.e. time, the changes in fluorescence intensity and thus the FRET signal due to the membrane fusion can be reconstructed as shown in Fig. 3.6.

Each of these liposome populations were flown through the microfluidic device and the resulting donor fluorescence was recorded as described earlier. The microfluidic channel had a cross sectional area of $0.025\,mm^2$ and length of 445.5 mm. There are 40 'turns' in the channel and each turn segment provides one time window at which the images are recorded. For different volumetric flow rates in the channel, the reaction time point changes along the channel linearly with the flow rate. Figure 3.6 shows fluorescence of the acceptor fluorophore as a function of the reaction time along the channel at different flow rates. As expected, when the fusion of the membranes occurs, the fluorescence of the acceptor increases as seen. Further, when we control the flow rate and thus the time points along the channel, we see the linear
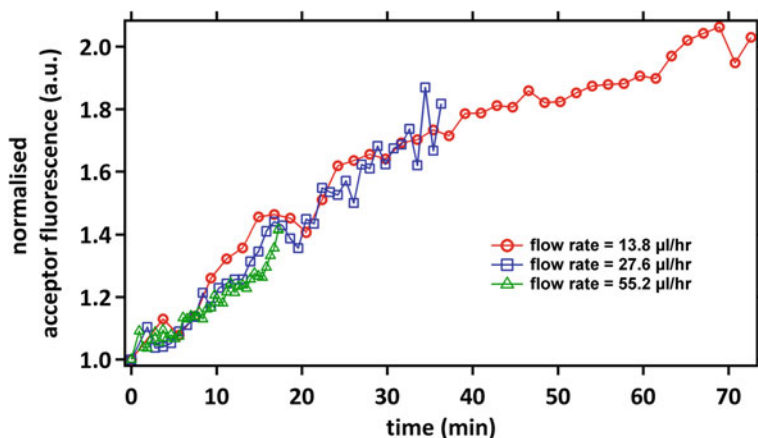
Fig. 3.6 Flow rate control of time axis in the microfluidics experiments. As we increase the flow rate, thus shortening the time along the channel, we see that the fusion of the membranes proceeds only until that time point (*green curve*). We then see that these time points depend linearly on the flow rate within the channel

dependance of the reaction time on the volumetric flow rate in the channel. The donor fluorophore shows a corresponding drop in fluorescence intensity due to the FRET coupling. The fusion kinetics are similar to those in measurements in bulk and thus the microfluidic technique forms a reliable platform to carry out fusion experiments. Furthermore, a controlled Ca^{2+} trigger can be provided by introducing an appropriate side channel in the microfluidic network at the required distance along the main reaction channel.

In the next sections, using an appropriate combination of microfluidic and bulk experiments, the electrostatic interactions and the role of the Ca^{2+} trigger synaptotagmin-1 are further investigated.

3.3 Results

3.3.1 Electrostatic Repulsion Blocks Membrane Fusion

As we mentioned before, SNARE mediated liposome fusion is typically studied at physiological ionic strength, with NaCl or KCl concentrations ranging between 100 and 150 mM. At these salt concentrations, the debye charge screening length is typically only ∼7 Å. Therefore, molecules need to be within a few times this distance to interact via charge effects. First, we study the effect of lowering the ionic strength of the buffer solution, on SNARE-mediated fusion, in the absence of synaptotagmin-1. This is measured by employing the FRET-based lipid mixing assay described above.

As expected, and as already shown in numerous studies [3, 10, 11, 16, 17, 23, 24, 26–32, 34–41], mixing the liposomes at normal ionic strength (20 mM K-Hepes pH 7.4, 150 mM KCl) resulted in robust lipid mixing. This is shown in Fig. 3.7 by the plotting the fluorescence intensity of the donor fluorophore of the FRET pair as a function of time. Clearly, if fusion proceeds, this signal decreases with time. As the ionic strength was lowered progressively, substantial decrease in the lipid mixing kinetics is seen (left panel of Fig. 3.7) and membrane fusion is almost completely blocked at low ionic strength (20 mM K-Hepes pH 7.4, 5 mM KCl, 300 mM sucrose). In low ionic strength buffers, osmolarity differences lead to disruption of liposomes and therefore the osmolarity is compensated by adding sucrose to the buffer, which increases the viscosity of the solution. However, the reduction in diffusion at higher viscosities does not account for the complete blocking of membrane fusion. Indeed, at an ionic strength of 5 mM KCl, the debye screening length is about 25 Å compared to ~7 Å at normal ionic strengths.

Since the liposomes contained a high fraction of anionic lipids, the electrostatic repulsion might be too high for the lipid membranes to come close enough for SNARE-mediated membrane fusion to occur at low ionic strength. The experiments were repeated with liposomes composed of pure zwitterionic lipids and also with liposomes composed of a reduced (9:1) ratio of uncharged:charged lipids. As seen in the right panel of Fig. 3.7, membrane fusion does occur at lower ionic strengths.
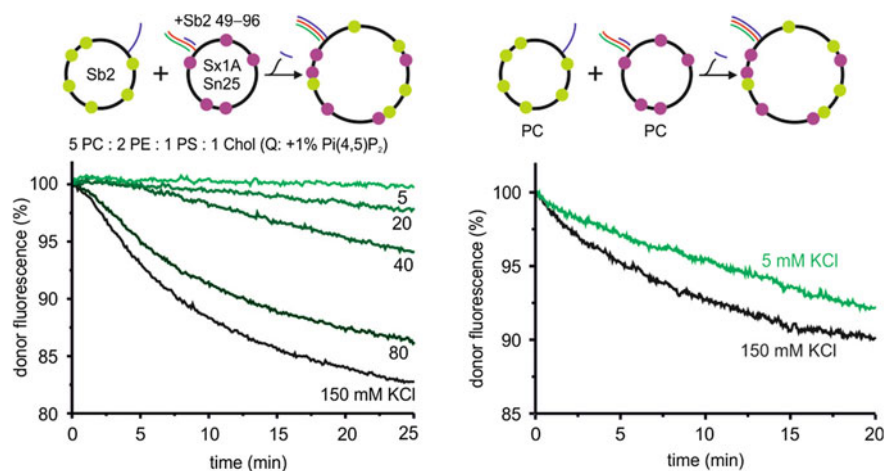
Fig. 3.7 SNARE mediated membrane fusion is blocked at low ionic buffer strengths due to repulsion between charged lipids comprising the liposomes. *Left panel* Liposomes contain charged lipids PS and Pi(4,5)P$_2$. With the progressive reduction of the salt (KCl) concentration in the buffer solution, the fusion is reduced, until it is almost completely blocked at a concentration of 5 mM KCl (low ionic strength). The experimental conditions are shown on the *top*. *Right panel* When only uncharged lipids are used, the fusion proceed normally even when charges are not screened at low ionic strengths of the buffer solution. The reduced kinetics at 5 mM KCl concentration is due to the increased viscosity of the buffer as described in the main text

However, the fusion rate is slower due to the reduced diffusion of the liposomes (due to the higher viscosity of the buffer as described above). Electrostatic repulsion at low ionic strength therefore increases the energy barrier of membrane fusion.

As discussed earlier, according to the current picture of SNARE-mediated fusion, the SNARE nucleation occurs even before any action of Ca^{2+} or synaptotagmin-1. We therefore investigated if this is still true when there are repulsive interactions between the liposomes, when the ionic strength of the buffer is lowered. This is done by tagging the complementary SNARE proteins by FRET pair fluorophores rather than the lipids in a vesicle as shown in the schematic in Fig. 3.8. It can be seen in the bottom panel of Fig. 3.8 that SNARE nucleation does not occur when electrostatic repulsion between the vesicles is high. When the buffer contains 150 mM KCl (normal ionic strength), the donor fluorescence reduces significantly with time, indicating that the SNARE proteins come close enough to nucleate and form a coil–coil structure. However, when the buffer salt concentration is reduced to 5 mM KCl (low ionic strength), SNARE nucleation does not take place. Further, the addition of 1 mM Ca^{2+} to this solution did not cause any SNARE-nucleation either.

In the absence of liposomes that house the SNARE proteins, it can be checked if SNARE nucleation itself is affected by electrostatic interactions. SNARE nucleation is not expected to be affected since the interactions are not mediated by charges. Indeed, when we repeat the above experiment, now without the R-SNARE or the Q-SNARE respectively, SNARE nucleation does proceed. In the first case (R_{sol}), the fluorescent tagged synaptobrevin-2 is present in solution, while the SNAP25 and
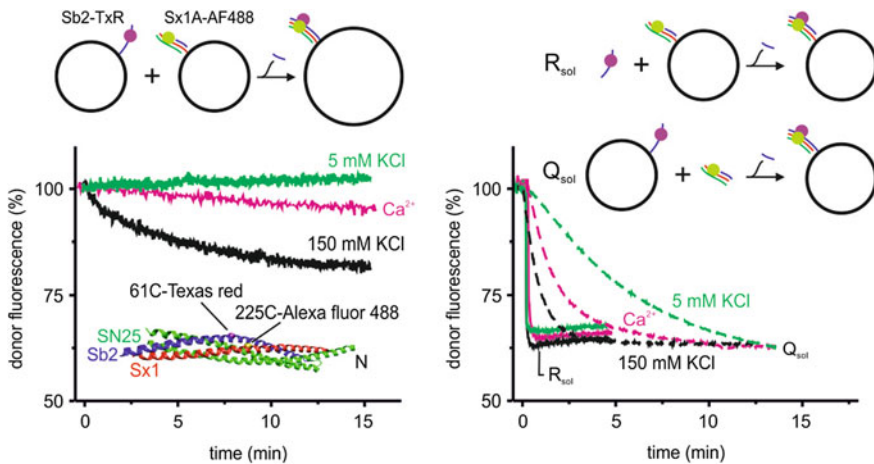
Fig. 3.8 SNARE nucleation is blocked at low ionic buffer strengths. *Left panel* When the fluorescently labelled SNARE proteins are present in their respective liposomes, reducing the ionic strength leads to a complete blocking of SNARE nucleation. The addition of 1 mM Ca^{2+} does not change the situation. *Right panel* In the absence of the repulsive interactions caused due to the lipids in the liposomes, SNARE nucleation proceeds normally irrespective of the ionic strength of the buffer used

syntaxin are present in a liposome. In this situation, we clearly do not expect the repulsive interactions that are mediated by the lipids. It can be seen that the SNARE nucleation proceeds normally regardless of the ionic strength of the solution, as indicated by the decrease in the donor fluorescence signal. Again in the second case (Q_{sol}), when the SNAP25 and syntaxin are in solution with the synaptobrevin-2 on a liposome, SNARE nucleation proceeds normally without any electrostatic effects. In this case, the kinetics are somewhat reduced compared to the first case of R_{sol} probably because of the reduced diffusion of the larger SNAP25-syntaxin complex.

All together, with these experiments we conclude that the high electrostatic repulsion between the liposomes blocks not only the fusion of the liposomes but also SNARE nucleation, even though SNARE nucleation itself is not charge dependant. This already indicates a clear departure from the current picture of SNARE-mediated fusion. When charge repulsion effects are in place, SNAREs are probably not already in a coil-coil structure before the action of Ca^{2+}-synaptotagmin-1. Under such conditions, it now allows us to clarify the role of synaptotagmin-1, the Ca^{2+} trigger of fusion.

3.3.2 Ca^{2+}-Synaptotagmin-1 Rescues Membrane Fusion

Having established that electrostatic repulsion of lipid membranes blocks their fusion, we introduced the Ca^{2+} trigger synaptotagmin-1 to the process. For these experiments, full-length synaptotagmin-1 is reconstituted at a protein-to-lipid ratio of 1:4,000 in the R-SNARE liposomes. The ratio of synaptotagmin-1 to synaptobrevin-2 in these liposomes is 1:4, which is similar to that in synaptic vesicles [42]. As in previous studies, at normal ionic strength, the kinetics of lipid mixing were increased very little compared to the liposomes without synaptotagmin-1 and did not or only weakly depended on the Ca^{2+} concentration [28, 32].

In contrast, at low ionic strength the lipid mixing was almost completely blocked in the absence of Ca^{2+}, in spite of the presence of synaptotagmin-1. The addition of 1 mM Ca^{2+} from a side channel in the microfluidic chip dramatically increases the fusion kinetics (Fig. 3.9). This liposome fusion is strictly dependent on the presence of both synaptotagmin-1 and the SNAREs. This can be seen the left panel of Fig. 3.10, which shows the fusion experiments under different conditions of ionic strengths, presence or absence of Ca^{2+} and the presence or absence of synaptotagmin-1. The fusion efficiency can be controlled by different amounts of added Ca^{2+} and a roughly linear behaviour is found as evidenced in the right panel of Fig. 3.10. This was further tested with synaptic vesicles, extracted from rat brains, that contain a large fraction of about 15 % anionic lipids, which yielded similar results. Membrane fusion at low ionic strength is found to be largely Ca^{2+}-dependent. Thus, at low ionic strength Ca^{2+}-synaptotagmin-1 triggers lipid mixing not only of liposomes, but also of native synaptic vesicles.

Because the FRET assay due to the mixing of lipids does not distinguish between hemifusion and full membrane fusion, it is conceivable that the membrane fusion
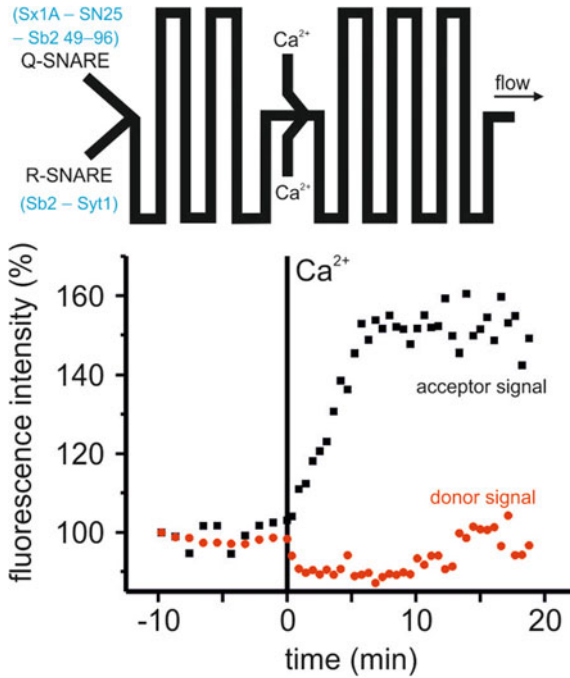
Fig. 3.9 Microfluidic triggering of membrane fusion at low ionic strengths by mediating Ca^{2+}-synaptotagmin-1 interactions. *Top panel* The channel geometry to study the Ca^{2+} triggering. The Q-SNARE and the R-SNARE are initially mixed and their fusion kinetics can be followed by taking images at multiple turn segments. After a certain time, Ca^{2+} is introduced from a side channel from which point on, the Ca^{2+} triggered fusion kinetics can be studied. *Bottom panel* The fluorescence intensities of the donor and acceptor fluorophore are shown as a function of time. The time point of Ca^{2+} addition is taken as t $=0$. Before the addition of Ca^{2+} no fusion takes place in spite of the synaptotagmin-1 already present in the R-SNAREs. As soon as Ca^{2+} is added, fusion increases dramatically

did not progress beyond the hemifusion state. To resolve this issue, we employed a content mixing assay where liposomes with encapsulated calcein at self quenching concentrations were fused with empty (calcein-free) liposomes [25]. Content mixing results in calcein dequenching. Indeed, a SNARE and Ca^{2+}-synaptotagmin-1 specific increase in fluorescence was observed (Fig. 3.11). This content mixing was not caused by leakage of the calcein from the liposomes, as leakage was only 4–5 % of total calcein.

Synaptotagmin-1 in concord with Ca^{2+} seemingly overcomes the repulsive interactions to induce membrane fusion at low ionic strengths. What exactly is the mechanism by which this trigger is mediated? As we discussed earlier, a variety of mechanisms have been proposed in the past by which synaptotagmin-1 affects the membrane to trigger fusion. In the next sections, the putative mechanism at low ionic strengths and the interactions with Ca^{2+} is investigated.
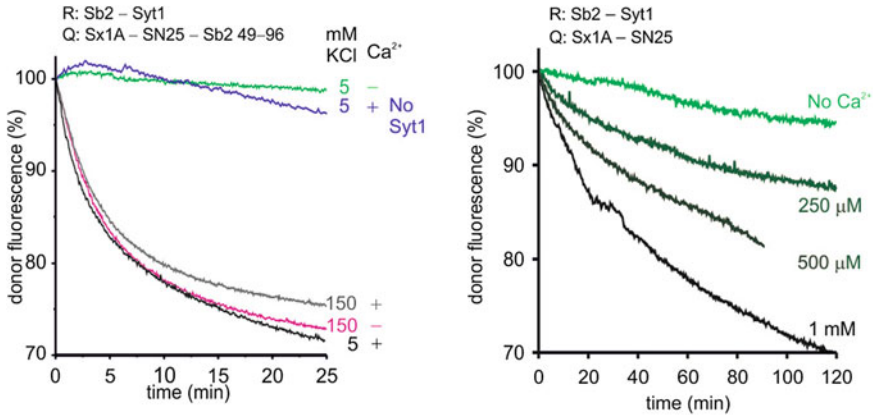
Fig. 3.10 *Left panel* Membrane fusion at low ionic strengths is strictly dependant on the presence of both Ca^{2+} and synaptotagmin-1. In the absence of either of these, fusion does not proceed. When both these are present, fusion proceeds normally even at low ionic strengths. At normal ionic stengths however, neither Ca^{2+} nor synaptotagmin-1 dramatically changes the kinetics. The + and − symbols indicate the presence and absence of Ca^{2+} respectively. *Right panel* The fusion rate depends on Ca^{2+} concentration. A roughly linear dependance is seen

3.3.3 Synaptotagmin-1 May Be a Distance Regulator

The experiments described thus far establish a clear Ca^{2+} dependant role of synaptotagmin-1 in membrane fusion at low ionic strengths. We now seek to uncover the exact mechanistic details of this interaction. As described in earlier sections, synaptotagmin-1 has one membrane anchor and two sites for Ca^{2+} binding, the C2A and the C2B domains. Indeed, when the two calcium binding are disrupted, membrane fusion does not occur at low ionic strengths even in the presence of Ca^{2+} (Fig. 3.11).

Further, previous studies have shown that the synaptotagmin-1 binds to anionic lipids both with and without Ca^{2+} and this binding leads to membrane clustering [5, 7, 18, 9–13, 26]. Indeed, negative-staining electron microscopy showed strong instantaneous clustering of the liposomes when synaptotagmin-1 liposomes were mixed with empty liposomes without SNAREs (Fig. 3.12). This clustering was $Pi(4, 5)P_2$ and synaptotagmin-1 specific and was reduced when a mutant of synaptotagmin-1 was used that does not bind electrostatically to anionic lipids. Identical results were obtained when the SNAREs were present. This was further confirmed by dynamic light scattering (DLS) experiments where the mean size of liposomes without fusion or synaptotagmin was found to be 40 ± 8 nm but that increased to 110 ± 55 nm due to liposome clustering in the presence of synanptotagmin-1.

Together, these indicate that without Ca^{2+} the polybasic patch of synaptotagmin-1 leads to the clustering of liposomes, but not to their fusion. The size of the clusters reveals that while the liposomes are not fused, they are still close together. There-
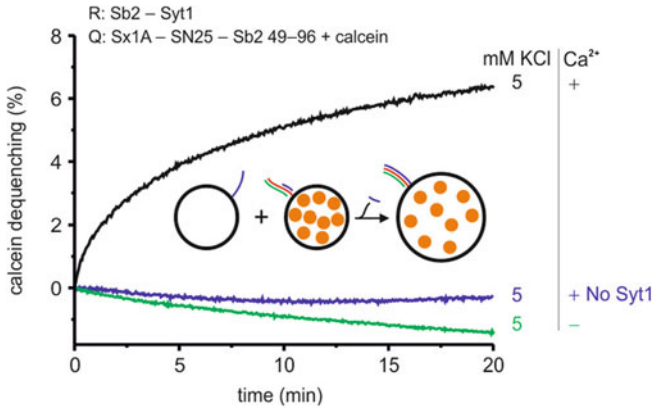
Fig. 3.11 Fluorescence quenching of calcein is used to assay content mixing to confirm liposome fusion triggered by Ca^{2+}-synaptotagmin-1
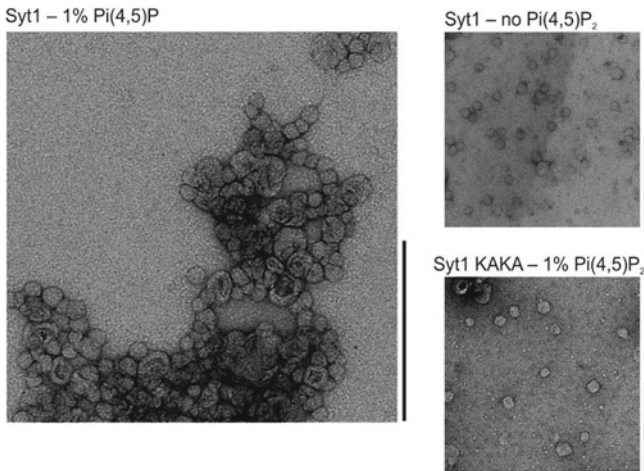
Fig. 3.12 In the absence of Ca^{2+}, synaptotagmin-1 leads to liposome clustering. This clustering is mediated by the electrostating binding of synaptotagmin-1 to anionic lipids in the liposomes

fore it can be imagined that the synaptotagmin-1 tethers the liposomes together and yet keeps them sufficiently far for SNARE nucleation to occur. We estimated how far synaptotagmin-1 could tether two membranes in various conformations with coarse-grain molecular dynamics simulations. The C2AB-domain was simulated based on the available crystal structure (PDB 1DQV). Each individual C2-domain was conformationally fixed, but had full translational and rotational mobility and was connected by a flexible linker (residues 266–273), as supported by NMR data. We then pulled pair-wise on the Ca^{2+}-binding patches, the polybasic patch and the N-terminus (Fig. 3.13). The distances between those sites reflect the maximum

length that synaptotagmin-1 can connect two membranes and are determined by
the interconnecting linker and the surface interactions between the C2-domains.
These distances are overestimates, because membrane insertion and bending are not
accounted for. The distance from the polybasic patch to the transmembrane helix is
$\sim$28 nm (including the $\sim$23 nm linker). However, the distance synaptotagmin-1 teth-
ers liposomes without Ca^{2+} is likely shorter since the debye length is only $\sim$25 Å,
but higher than the $\sim$5 nm from the FRET experiments. The maximum distances
the Ca^{2+}-bound C2AB-domain could span two membranes is $\sim$2–7.5 nm, close to
the 4 nm from cryo-electron microscopy data [9]. These distances would explain
why decreasing the ionic strength and increasing the sebye length from $\sim$7 to 25 Å
has such a dramatic effect on membrane fusion. Thus, at low ionic strength, Ca^{2+}
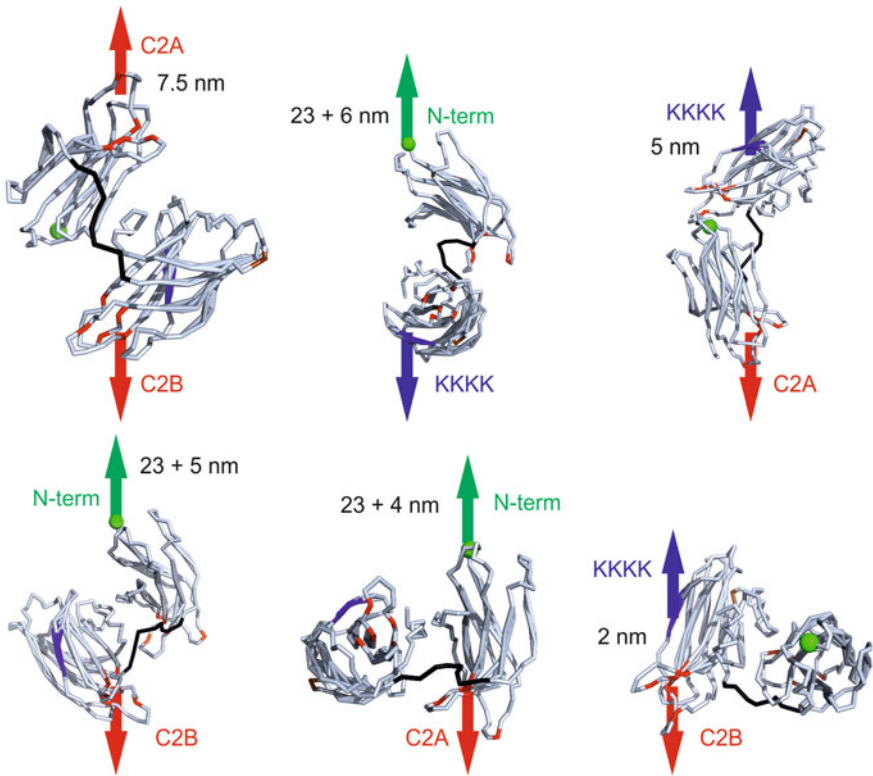
Fig. 3.13 Molecular dynamic simulations to estimate the maximal distances between the various
domains. In the simulations, we pulled pair-wise on various membrane binding sites of the C2AB-
domain: the N-terminus (*green*), the polybasic lysine patch (*blue*; KKKK) and the Ca^{2+}-binding
sites of the C2A- and C2B-domain (*red*). The two conserved arginines (R398 and R388) are shown
in *brown*; the linker is in *black*. The N-terminus is connected to the transmembrane helix with a 61
residue linker that can extent to $\sim$23 nm. Maximal distances are indicated in the figure; these are an
approximate for the tethering distances of the membranes, but do not take into account additional
interactions such as membrane insertion and bending

changes the membrane distance from 5–28 nm to below that required for SNARE complex formation (8 nm at normal ionic strength [36]) such that membrane fusion can occur.

3.4 Summary and Outlook

In this chapter we investigated SNARE mediated membrane fusion under conditions where electrostatic interactions between the component membranes are not screened. In order to study these interactions, we developed a microfluidic technique based on a standard FRET assay for membrane fusion. Our data show that in a simple reconstituted system, key elements of synaptic transmission can be mimicked if SNARE nucleation is prevented by keeping the membranes apart before Ca^{2+}-triggering. The charged lipids that constituting the bilayers result in repulsive interactions that keep the membranes too far for even SNARE nucleation to occur. However, even under such conditions, synaptotagmin-1, a Ca^{2+} trigger for membrane fusion, tethers the two lipid membranes, although the SNARE proteins are fully active. Upon addition of Ca^{2+}, the binding of Ca^{2+} to synaptotagmin-1 results in a conformational change of the protein that brings lipid bilayers close enough for SNARE nucleation to occur and thus for membrane fusion to proceed (Fig. 3.14). While we were able to reproduce, in vitro, the massive increase of membrane fusion triggered by Ca^{2+}, the condition of low ionic strength of the buffer is not a relevant physiological condition. However, it is conceivable that proteins residing in the space between the vesicle and the plasma membrane can fulfill the condition of keeping the membranes too far for fusion to readily occur. Considering that both synaptic vesicles and release sites are indeed crowded with membrane proteins [41], such a scenario is not unlikely.
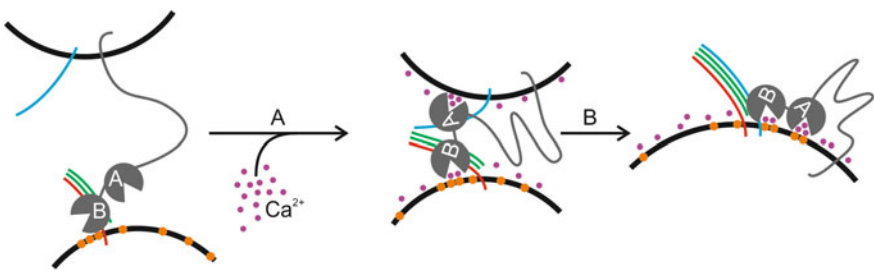
Fig. 3.14 Model for synaptotagmin-1 mediated lipid mixing. In the absence of Ca^{2+}, synaptotagmin-1 (*grey*) tethers to anionic membranes, and particularly to Pi(4,5)P_2 (*orange*) via its polybasic lysine patch. The distance is too far for SNARE formation to occur (synaptobrevin-2: *blue*; Syntaxin-1A: *red*; SNAP-25: *green*). (Step A) In the presence of Ca^{2+} (*purple*), a transitional conformation change occurs and synaptotagmin-1 binds the membrane via its calcium binding pockets and basic residues on the C2AB-domain. This drives the membranes together and SNARE complex formation can occur (Step B) The SNARE complex formation drives membrane fusion

However, further experiments are needed to determine whether under physiological conditions SNARE nucleation occurs before or after Ca^{2+}-triggering in regulated exocytosis of synaptic vesicles.

References

1. A.T. Brunger, K. Weninger, M. Bowen, S. Chu, Single-molecule studies of the neuronal SNARE fusion machinery. Annu. Rev. Biochem. **78**, 903–928 (2009)
2. R. Jahn, R.H. Scheller, SNAREs-engines for membrane fusion. Nat. Rev. Mol. Cell Biol. **7**, 631–643 (2006)
3. E.R. Chapman, How does synaptotagmin trigger neurotransmitter release? Annu. Rev. Biochem. **77**, 615–641 (2008)
4. S. Martens, H.T. McMahon, Mechanisms of membrane fusion: disparate players and common principles. Nat. Rev. Mol. Cell Biol. **9**, 543–556 (2008)
5. A. Radhakrishnan, A. Stein, R. Jahn, D. Fasshauer, The Ca^{2+} affinity of synaptotagmin 1 is markedly increased by a specific interaction of its C2B domain with phosphatidylinositol 4,5-bisphosphate. J. Biol. Chem. **284**, 25749–25760 (2009)
6. I. Fernandez, D. Araç, J. Ubach, S.H. Gerber, O. Shin, Y. Gao, R.G. Anderson, T.C. Südhof, J. Rizo, Three-dimensional structure of the synaptotagmin 1 C2B-domain: synaptotagmin 1 as a phospholipid binding machine. Neuron, **32** (2001)
7. L. Li, O. Shin, J. Rhee, D. Araç, J. Rah, J. Rizo, T. Südhof, C. Rosenmund, Phosphatidylinositol phosphates as co-activators of Ca^{2+} binding to C2 domains of synaptotagmin 1, J. Biol. Chem. **281** (2006)
8. J. Bai, W.C. Tucker, E.R. Chapman, PIP2 increases the speed of response of synaptotagmin and steers its membrane-penetration activity toward the plasma membrane. Nat. Struct. Mol. Biol. **11**, 36–44 (2004)
9. D. Araç, X. Chen, H.A. Khant, J. Ubach, S.J. Ludtke, M. Kikkawa, A.E. Johnson, W. Chiu, T.C. Südhof, J. Rizo, Close membrane-membrane proximity induced by Ca^{2+}-dependent multivalent binding of synaptotagmin-1 to phospholipids. Nat. Struct. Mol. Biol. **13**, 209–217 (2006)
10. J.D. Gaffaney, F.M. Dunning, Z. Wang, E. Hui, E.R. Chapman, Synaptotagmin C2B domain regulates Ca^{2+}-triggered fusion in vitro: critical residues revealed by scanning alanine mutagenesis. J. Biol. Chem. **283**(46), 31763–31775 (2008)
11. A. Bhalla, M.C. Chicka, W.C. Tucker, E.R. Chapman, Ca^{2+}-synaptotagmin directly regulates t-SNARE function during reconstituted membrane fusion. Nat. Struct. Mol. Biol. **13**, 813–821 (2006)
12. D.Z. Herrick, S. Sterbling, K.A. Rasch, A. Hinderliter, D.S. Cafiso, Position of synaptotagmin I at the membrane interface: cooperative interactions of tandem C2 domains. Biochemistry **45**, 9668–9674 (2006)
13. E. Hui, J. Bai, E.R. Chapman, Ca^{2+}-triggered simultaneous membrane penetration of the tandem C2-domains of synaptotagmin I. Biophys. J. **91**, 1767–1777 (2006)
14. G. Schiavo, Q.M. Gu, G.D. Prestwich, T.H. Söllner, J.E. Rothman, Calcium-dependent switching of the specificity of phosphoinositide binding to synaptotagmin, in *Proceedings of the National Academy of Sciences of the United States of America*, vol. 93 (1996)
15. J. Rizo, X. Chen, D. Araç, Unraveling the mechanisms of synaptotagmin and SNARE function in neurotransmitter release. Trends Cell Biol. **16**, 339–350 (2006)
16. S. Martens, M.M. Kozlov, H.T. McMahon, How synaptotagmin promotes membrane fusion. Science **316**, 1205–1208 (2007)
17. E. Hui, C.P. Johnson, J. Yao, F.M. Dunning, E.R. Chapman, Synaptotagmin-mediated bending of the target membrane is a critical step in Ca^{2+}-regulated fusion. Cell **138**, 709–721 (2009)

18. J. Bai, C. Wang, D.A. Richards, M.B. Jackson, E.R. Chapman, Fusion pore dynamics are regulated by synaptotagmin*t-SNARE interactions. Neuron **41**, 921–942 (2004)
19. M. Vrljic, P. Strop, J.A. Ernst, R.B. Sutton, S. Chu, A.T. Brunger, Molecular mechanism of the synaptotagmin-SNARE interaction in Ca^{2+}-triggered vesicle fusion. Nat. Struct. Mol. Biol. **17**, 318–324 (2010)
20. U.B. Choi, P. Strop, M. Vrljic, S. Chu, A.T. Brunger, K.R. Weninger, Single-molecule FRET-derived model of the synaptotagmin 1-SNARE fusion complex. Nat. Struct. Mol. Biol. **17**, 325–331 (2010)
21. J.R. Schaub, X. Lu, B. Doneske, Y. Shin, J.A. McNew, Hemifusion arrest by complexin is relieved by Ca^{2+}-synaptotagmin I. Nat. Struct. Mol. Biol. **13**, 748–750 (2006)
22. M. Xue, C. Ma, T.K. Craig, C. Rosenmund, J. Rizo, The janus-faced nature of the C(2)B domain is fundamental for synaptotagmin-1 function. Nat. Struct. Mol. Biol. **15**, 827–835 (2008)
23. J. Tang, A. Maximov, O. Shin, H. Dai, J. Rizo, T.C. Südhof, A complexin/synaptotagmin 1 switch controls fast synaptic vesicle exocytosis. Cell **126**, 1175–1187 (2006)
24. T. Weber, B.V. Zemelman, J.A. McNew, B. Westermann, M. Gmachl, F. Parlati, T.H. Söllner, J.E. Rothman, SNAREpins: minimal machinery for membrane fusion. Cell **92**, 759–772 (1998)
25. G. van den Bogaart, M.G. Holt, G. Bunt, D. Riedel, F.S. Wouters, R. Jahn, One SNARE complex is sufficient for membrane fusion. Nat. Struct. Mol. Biol. **17**, 358–364 (2010)
26. A. Stein, A. Radhakrishnan, D. Riedel, D. Fasshauer, R. Jahn, Synaptotagmin activates membrane fusion through a Ca^{2+}-dependent trans interaction with phospholipids. Nat. Struct. Mol. Biol. **14**, 904–911 (2007)
27. M.C. Chicka, E. Hui, H. Liu, E.R. Chapman, Synaptotagmin arrests the SNARE complex before triggering fast, efficient membrane fusion in response to Ca^{2+}. Nat. Struct. Mol. Biol. **15**, 827–835 (2008)
28. H. Lee, Y. Yang, Z. Su, C. Hyeon, T. Lee, H. Lee, D. Kweon, Y. Shin, T. Yoon, Dynamic Ca^{2+}-dependent stimulation of vesicle fusion by membrane-anchored synaptotagmin 1. Science **328**(5979):760–763 (2010)
29. K.L. Lynch, R.R.L. Gerona, E.C. Larsen, R.F. Marcia, J.C. Mitchell, T.F.J. Martin, Synaptotagmin C2A loop 2 mediates Ca^{2+}-dependent SNARE interactions essential for Ca^{2+}-triggered vesicle exocytosis. Mol. Biol. Cell, **18**, 4957–4968 (2007)
30. W.C. Tucker, T. Weber, E.R. Chapman, Reconstitution of Ca^{2+}-regulated membrane fusion by synaptotagmin and SNAREs. Science **304**, 435–438 (2004)
31. J. Rhee, L.Y. Li, O. Shin, J. Rah, J. Rizo, T.C. Südhof, C. Rosenmund, Augmenting neurotransmitter release by enhancing the apparent Ca^{2+} affinity of synaptotagmin 1, in *Proceedings of the National Academy of Sciences of the United States of America*, vol. 102 (2005)
32. M. Margittai, D. Fasshauer, S. Pabst, R. Jahn, R. Langen, Homo- and heterooligomeric SNARE complexes studied by site-directed spin labeling. J. Biol. Chem. **276**, 13169–13177 (2001)
33. D. Fasshauer, M. Margittai, A transient N-terminal interaction of SNAP-25 and syntaxin nucleates SNARE assembly. J. Biol. Chem. **279**, 7613–7621 (2004)
34. A.V. Pobbati, A. Stein, D. Fasshauer, N- to C-terminal SNARE complex assembly promotes rapid membrane fusion. Science **313**,673–676 (2006)
35. T.J. Siddiqui, O. Vites, A. Stein, R. Heintzmann, R. Jahn, D. Fasshauer, Determinants of synaptobrevin regulation in membranes. Mol. Biol. Cell, **18**, 2037–2046 (2007)
36. F. Li, F. Pincet, E. Perez, W.S. Eng, T.J. Melia, J.E. Rothman, D. Tareste, Energetics and dynamics of SNAREpin folding across lipid bilayers. Nat. Struct. Mol. Biol. **14**, 890–896 (2007)
37. D.J. James, C. Khodthong, J.A. Kowalchyk, T.F.J. Martin, Phosphatidylinositol 4,5-bisphosphate regulates SNARE-dependent membrane fusion. J. Cell Biol. **182**, 355–366 (2008)
38. G. van den Bogaart, N. Hermans, V. Krasnikov, A.H. de Vries, B. Poolman, On the decrease in lateral mobility of phospholipids by sugars. Biophys. J. **92**, 1598–1605 (2007)
39. C. Cerjan, R.E. Barnett, Viscosity dependence of a putative diffusion-limited reaction. J. Phys. Chem. **76**, 1192–1195 (1972)
40. J. Knight, A. Vishwanath, J. Brody, R. Austin, Hydrodynamic focusing on a silicon chip: mixing nanoliters in microseconds. Phys. Rev. Lett. **80**, 3863–3866 (1998)

41. S. Takamori, M. Holt, K. Stenius, E.A. Lemke, M. Gronborg, D. Riedel, H. Urlaub, S. Schenck, B. Brügger, P. Ringler, S.A. Müller, B. Rammner, F. Gräter, J.S. Hub, B.L.D. Groot, G. Mieskes, Y. Moriyama, J. Klingauf, H. Grubmüller, J. Heuser, F. Wieland, R. Jahn, Molecular anatomy of a trafficking organelle. Cell **127**, 831–846 (2006)
42. M. Holt, D. Riedel, A. Stein, C. Schuette, R. Jahn, Synaptic vesicles are constitutively active fusion machines that function independently of Ca^{2+}. Curr. Biol. **18**, 715–722 (2008)

Chapter 4
Phase Contrast X-Ray Imaging of Lipid Membranes

A propagation based phase contrast X-ray imaging technique is developed and is used to study the structure and interfacial properties of microfluidic lipid membranes and the fusion of the monolayers they consist of.

4.1 Introduction

The investigations of membranes and associated processes in Chaps. 2 and 3 clearly point to very important phenomena at the nanoscale. For example, electroporation of lipid membranes is expected to occur via nanoscopic orifices that open up in the bilayer under the influence of an electric field [1–3]. The intermediate structures of membrane fusion viz. the hemifusion and stalk formation states, if they exist, are certainly of nanometer scales. While the combination of a variety of techniques help to understand many aspects of such phenomena, direct visualization of the nanoscale structures is still a far away goal.

For light of a given wavelength λ, diffraction sets the limit on the resolution, d of observation in far field optical microscopy as $d \sim \lambda/2n \sin\alpha$, where $n \sin\alpha$ is the numerical aperture of the system. Therefore for visible light, resolutions below a few hundreds of nanometers are not achievable easily. While electron microscopy is capable of resolving nanostructures, its adaptability to the study of dynamics and the cumbersome sample preparation involved [4], limit its usage. Fluorescence microscopy techniques such as STED and STORM [5, 6] can reach resolutions of down to a few tens of nanometers, but this is still not sufficient to resolve the structural details of a lipid bilayer, for instance, which is only a few nanometers thick.

X-ray wavelengths can be used to probe even sub-nanometer length scales and the specific advantages of X-rays concern (i) the resolution, (ii) the kinematic nature of the scattering process enabling quantitative image analysis, (iii) element specific contrast variation and (iv) the potential of high time resolution. While on the one hand, scattering techniques such as grazing incident diffraction/small angle X-ray scattering (GID/GISAXS), X-ray reflectometry (XRR) and anomalous scattering have been widely used to study lipid membranes, they are not suitable for structure resolution in a functional context. This must be probed *in situ* via direct imaging techniques and all direct X-ray microscopy techniques are limited in spatial resolution to a few 10 nm (~2 orders of magnitude away from the classical diffraction barrier) [7, 8] due to aberratons and the limited numerical aperture of today's X-ray optics. The fabrication of high resolution lenses currently poses severe technological challenges. Lensless coherent X-ray diffractive imaging (CXDI) [9] has been proposed to circumvent these practical limitations, but its full potential is yet to be realized.

Recently, a technique based on hard X-ray Fresnel diffraction (propagation imaging) was used to image free standing lipid bilayers, with phase contrast arising from free space propagation of the beam traversing through the lipid bilayer [10]. A simple, yet extendable model was used to quantitate the information from the phase contrast image and a resolution down to ~5 nm in one dimension, could be obtained [11] by using a focussed beam instead of a parallel beam. In this chapter, we extend the scope of this technique by imaging the lipid membranes formed in microfluidic channels, where the depth and planarity of the membrane are of potential importance in increasing the phase contrast, thus improving resolution.

4.2 Experimental Techniques

4.2.1 Synchrotron Setup

Divergent beam imaging experiments were performed at the insertion device 22NI undulator station at ESRF (Grenoble, France). The beamline includes a U42 undulator, which is operated at the third harmonic to deliver a so called 'pink X-ray beam' with photons of 17.5 keV energy and a corresponding wavelength of 0.708 Å. The source size at the undulator is 700 μm (h) $\times$ 30 μm (v) (FWHM) with a divergence of 28 μrad (h) $\times$ 5 μrad (v). A set of slits defines a secondary source size of 25 μm in the horizontal direction. For additional focusing a Kirkpatrick-Baez (KB) mirror-pair is located in the experimental hutch [12, 13]. The microfluidic device is placed in the focus of the KB system that coincides with the focus of the on-axis microscope (OAM). The focus is located 30 mm downstream the KB mirrors and has a diameter of 130 nm (v) and 140 nm (h), which was measured by performing knife edge scans in both directions. A drilled mirror allows for the simultaneous detection of light microscope and X-ray images and thus a faster alignment of the sample in the beam.

The detector is a Fast-Readout, Low-Noise (FRELON 2000; ESRF, Grenoble) CCD camera [14]. It is combined with a 24 μm thick LSO:Tb (Terbium doped Lutetium-Oxoorthosilikat, Lu_2SiO_5) scintillator, optimized for high resolution imaging, that converts the X-rays into visible light photons of 550 nm wavelength and is supported by a 170 μm YSO (Ytterbium-Oxoorthosilicate, Yb_2SiO_5) substrate [15, 16]. It is placed 526 mm behind the KB focus. The image is magnified by a 10× objective and a 2.5× eyepiece to fit the dimension of the 14-bit Kodak KAF4320 CCD chip with a physical pixel size of 24 μm and a resolution of 2048 × 2048 pixels. Consequently, the theoretical pixel size of the images is 0.96 μm. The effective pixel size depends on the position z of the sample and was varied in a range of defocusing distances 3 mm ≤ z ≤ 200 mm, with respect to the KB mirror focus.

### 4.2.2 Microfluidic Devices and Membrane Preparation

Microfluidic devices made out of PDMS (Sylgard 184, Dow Chemicals) are not suitable for X-ray studies due to the scattering from the crosslinked PDMS matrix. We developed a new technique for use in the X-ray imaging studies. The design of the SU8-silicon masters (positive) simply consists of two crossed channels in different widths of 300 μm, 500 μm or 1 mm. To reproducibly prepare a large amount of microfluidic channels a positive PDMS master is created for the preparation of microfluidic chips made from UV-curable glue (Norland Optical Adhesive No. 81, Edmund Optics; Karlsruhe, Germany). This fast curing UV glue is used due to its transparency, weak X-rays scattering properties and its stiffness (compared to PDMS) after intense curing. Therefore the SU8-silicon master (Fig. 4.2a) is placed in a Petri dish and the PDMS-crosslinker solution is poured in (Fig. 4.2b). Degassing is performed in a vacuum chamber to get rid of the air that is trapped underneath the silicon wafer. Subsequently, the PDMS is cured at 85 °C for 1 h or more and then a scalpel is used to cut out the negative copy. This part is put in a sealed glass beaker, together with a vial filled with hexamethyldisilazane (HMDS, Fluka; Germany), for approximately 15 min. The negative PDMS copy is placed in a Petri dish lined with aluminium foil and PDMS solution is poured onto it (Fig. 4.2c). After curing the PDMS, as described previously, everything is peeled of the aluminium foil and both PDMS parts are separated by cutting with a scalpel—leaving the negative copy and a positive secondary master of PDMS (Fig. 4.2d). The latter one is cut in a way that smooth edges are left and is subsequently laid on top of a very flat stamp of PDMS (Fig. 4.2e). A drop of UV glue is applied that crawls towards the channel cross by capillary forces. Glue is added for as long as the whole space between PDMS master and stamp is filled and no air bubble is left. The UV glue is exposed for 5–10 min to UV light (PolyluxPT, Dreve; Unna, Germany) and the final MF chip is carefully peeled off the PDMS under addition of Isopropanol (Fig. 4.2f). These devices offer the advantage that they are inert, very robust and can be used several times.

The membranes are prepared by running a pump (Fig. 4.1) which is connected to the oil channel for approximately 10 min to flush the channels with the lipid solution. This procedure has an additional hydrophobizing effect helping to promote
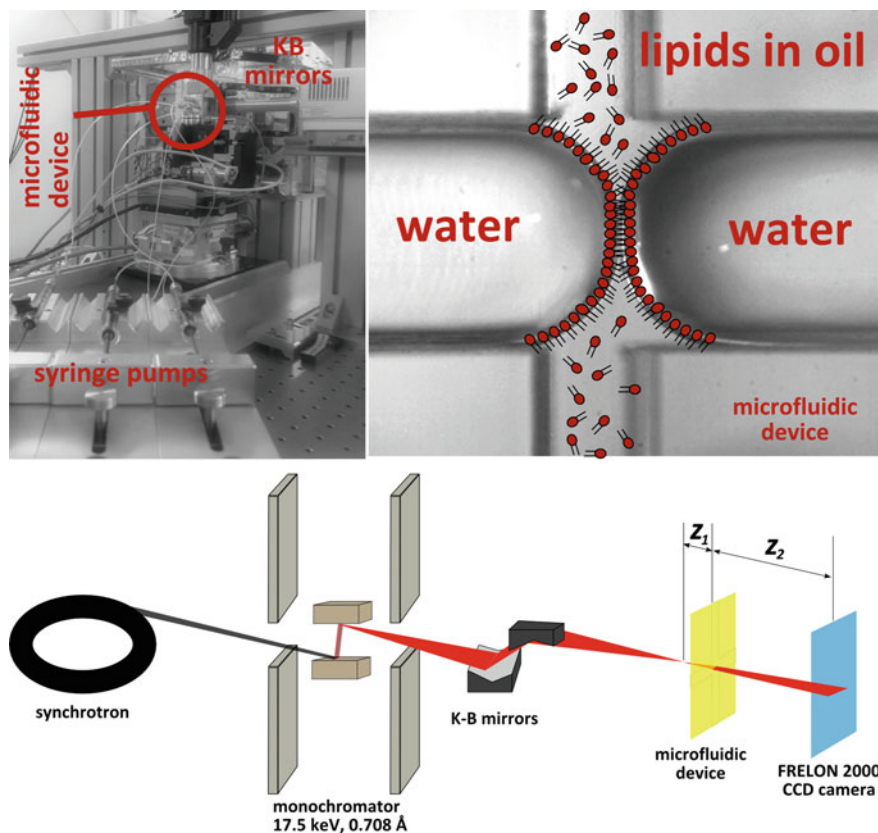
Fig. 4.1 A schematic of the synchrotron setup, at the ID22 (ESRF) beamline, for imaging a microfluidic lipid bilayer. A microfluidic device in which a lipid bilayer can be formed by two water droplets suitably covered by a monolayer of lipid

the formation of convex water interfaces (also called "water fingers"). Subsequently, the oil flow is stopped and the water fingers are slowly brought into contact in the channel cross region. When the two monolayers approach each other, intense Fresnel fringes appear in the visible light microscope before the monolayers fuse and form a bilayer. The size of the bilayer patch can be controlled by variation of the pressure in the water channels. Presence of a single bilayer is checked by insertion of electrodes in the aqueous channels to measure the capacitance of the interface. The orientation and geometry of the microfluidic lipid bilayers shows a great advantage compared to bulged black lipid membranes that were investigated in [10, 11]. As the phase contrast signal of a transparent object increases proportionally to the path length L of the X-rays inside the sample, the microfluidic bilayers offer an improved geometry for imaging experiments. L is in the range of a few micrometers in the case of a thin, bulged BLM. The diameter of a bilayer can equal the depth of the channel when it spans it fully. Consequently, the penetration depth becomes
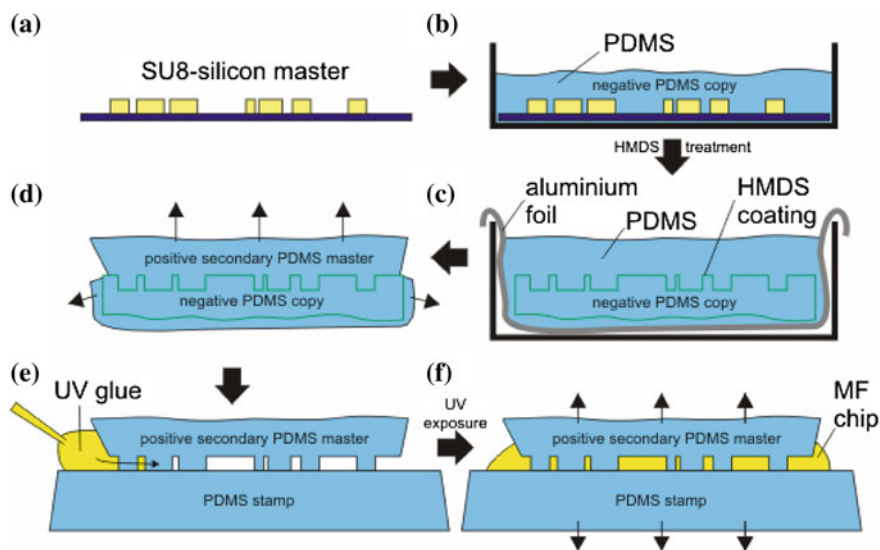
Fig. 4.2 To protect the SU8 masters (**a**) a three step copying technique is used for the microfluidic chip production. After preparing a negative PDMS copy of the channel structure (**b**) its surface is treated with HMDS and a secondary (positive) PDMS master is taken (**c**). This secondary master is separated from the surrounding PDMS (**d**) and placed on a flat PDMS stamp (**e**). The spaces in between are filled with UV curable glue and after 5–10 min of UV light exposure the microfluidic chip can be peeled off (**f**)

a few hundred micrometers assuming a planar orientation, i.e. no curvature, of the film. Nevertheless, these reconstituted membranes also show the drawback that the Plateau Gibbs border (PGB), the oil containing reservoir surrounding the membrane patch, will always be in the path of the X-rays. Due to the strong diffractive index contrast between the water and the PGB it is likely to give an additional contribution to the diffraction pattern. This is expected to make the theoretical modeling more complicated—however, for the work shown here, we do not yet include this effect into the model. It must be noted that this is not the case for the bulged interface of the BLMs where the theoretical modeling of the interface is thus less complicated.

4.3 Results

4.3.1 Phase Contrast Imaging Model

Quantitative structural and dynamical studies of microfluidic lipid membranes were performed by using a direct imaging method, namely propagation based X-ray phase contrast imaging (PCI). To this end a simplified model is introduced that explains
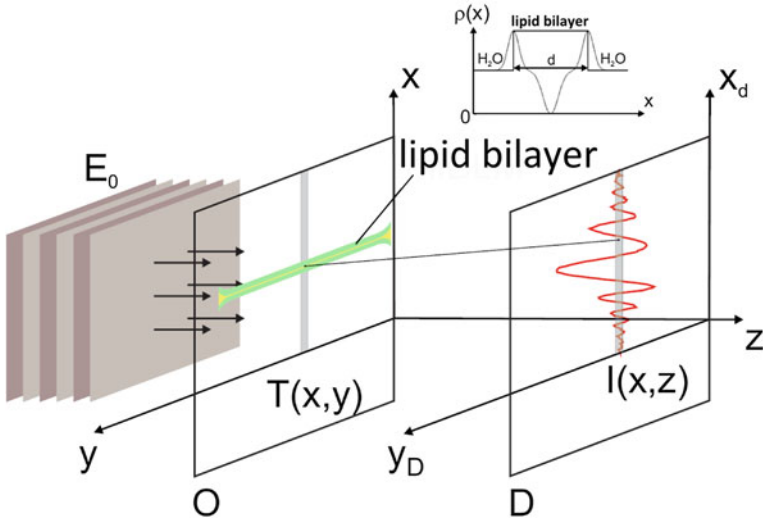
Fig. 4.3 The mfBLM at position O is described by a transmission function $T(x, y)$ obtained by projection of the electron density $\rho(x)$ along the z-axis. After free space propagation of the exit wave over a distance z along the optical axis, a Fresnel interference pattern $I(x)$ is recorded in the detector plane D, representing a phase contrast image of the projected density profile

the image formation of lipid membranes.[1] It is instructive to first study the problem in the context of a parallel beam geometry and extend the same to a divergent beam setup in the next section. We describe the propagation of wave fields interacting with this model system in the case of the Fresnel regime, comparable to Gabor's in-line holography.

We now consider a simplified scheme of the membrane that can be included in the underlying equations being elucidated later. This model is shown in Fig. 4.3. In the case of a swollen membrane of thickness d, that still includes organic solvent, we assume the electron density ρ to be constant across the membrane. It is regarded as the most relevant parameter describing the scattering properties of X-rays in an object. In the following the dispersive part δ of the complex refractive index $n = 1 - \delta + i\beta$, instead of the electron density ρ, will be used. Both parameters are related as follows [17, 18]:

$$\delta = \frac{\lambda^2 n_e r_0}{2\pi} n_e = \frac{N_A Z \rho}{A} \tag{4.1}$$

with the wavelength λ, classical electron radius r_0, Avogadro's number N_A, atomic number Z, atomic weight A, and the electron density number n_e (including the material's density ρ). In the following the phase shift ϕ, that is induced by the propagation of the X-rays through the membrane, shall be derived. Based on the definition of thin phase objects, which is given in [19–21], we assume the extension of the membrane

---

[1] Model developed by Michael Mell

along the z-axis and the interaction of the sample with the traversing photons to be very small. We consider no further propagation inside the object to occur, and thus the electron density can be projected into a plane behind the object.

The phase profile $\phi(x)$ is then written as

$$\phi(x) = -\frac{2\pi}{\lambda}\Delta\delta \int_{L_0} dz = -k\,\Delta\delta\,L(x), \tag{4.2}$$

with $\Delta\delta < 0$ the refractive index difference with respect to the surrounding water.

The formation of an image $E(x_d, y_d, z_d)$ at a position z_d in the detector plane D is given by propagating the impinging planar wave field (illumination function) $E(x, y, 0) = E_0$ interacting with the complex-valued optical transmission function of the sample [22, 23] $T(x, y) = B(x, y) \cdot e^{i\phi(x,y)}$ along the direction z of the beam (see Fig. 4.3). Here $B(x, y)$ represents the absorption and $\phi(x, y) = -k\,\Delta\delta\,L(x)$ the phase, which is defined by the refractive index contrast $\Delta\delta$ (between sample and surrounding water) and the phase accumulation length L(x) inside the sample, i.e. the diameter of the lipid bilayer patch. For a membrane inside a microfluidic channel this length can range from a few microns in the moment of monolayer fusion up to several hundred microns depending on the microfluidic channel height.

In the following discussion we will assume $B=1$ since lipid bilayers can be considered as weak phase objects. Furthermore, we are only interested in the intensity I(x,z) along a single axis in dependence of the electron density distribution $\rho(x)$. Thus we will restrict our discussions to the one-dimensional case in the following calculations and so for the wave field E_{in} in the plane behind the object:

$$E_{in}(x) = E_0 \cdot T(x) = E_0 \cdot e^{i\phi(x)} \tag{4.3}$$

For a parallel beam or a beam of small divergence (illumination function considered as a plane wave) and scattering signals at small momentum transfers, the imaging process is described by the Kirchhoff diffraction integral using the paraxial Fresnel approximation [24, 25]:

$$E(x_d, z) = \sqrt{\frac{i}{\lambda z}} \int_{-\infty}^{\infty} E_{in}\, e^{\frac{ik}{2z}(x-x_d)^2}\, dx. \tag{4.4}$$

By inserting $\sqrt{i} = e^{i\frac{\pi}{4}}$, $k = \frac{2\pi}{\lambda}$ and Eq. 4.3 into Eq. 4.4 it transforms to

$$E(x_d, z) = E_0 \sqrt{\frac{k}{2\pi z}}\, e^{-i\frac{\pi}{4}} \int_{-\infty}^{\infty} e^{i\phi(x)}\, e^{\frac{ik}{2z}(x-x_d)^2}\, dx. \tag{4.5}$$

The detected intensity is given as $I(x, z) = |E(x_d, z)|^2$ for each propagation (defocus) distance z. For numerical computation of the Fresnel intensity profile $I(x, z)$,

a simple box model of $\phi(x)$ can be used for the central interval of the object plane $[x_{min}, x_{max}]$, where the phase shift $\phi(x)$ is non-zero. To simplify matters the phase contrast is a constant value given by the the electron density contrast of the oil and the surrounding water. This simplification holds for planar membranes which have not thinned yet and contain an interlayer of solvent/oil.

To obtain the complete field $E(x) = E_c(x) + E_l(x) + E_r(x)$, the fields $E_l(x)$ and $E_r(x)$ due to the source points in the left and right half-planes (bordering the object interval $[x_{min}, x_{max}]$ in the sample plane) have to be added. For these regions constant (in practice often zero) relative phase shifts ϕ_l and ϕ_r can be assumed.

From the above equations we see that the intensity will increase as the wavelength λ and the propagation distance z decrease. In terms of λ this improvement will be compensated by less interaction between photons and the sample with higher photon energies. Regarding z, the fringe distance will shrink on reduction of the propagation distance and finally lead to a loss in resolution. Since the energy is mostly fixed at synchrotron beams, we can overcome the limits in resolution for small z by using a divergent beam geometry.

4.3.2 Divergent Beam Imaging

In this work we apply divergent beam propagation imaging to the presented membrane system. By using the geometry of a divergent beam, yielding a magnified phase contrast image of the object [26, 27], one can compensate for wavelength and propagation distance dependent effects. This leads to an increasing phase contrast at the expense of fringe distance and, consequently, less resolution, as discussed before. Thus, it allows one to circumvent the limited resolution, which is mainly defined by the detector and is, in the best case, in the range of $1\,\mu m$ [diameter of the point spread function (PSF)] [16]. Especially in the case of Fresnel fringes originating from the bilayer, the resolution of high spatial frequencies at high diffraction angles is increased. Thus, the propagation distance can be reduced without further loss in resolution. It was shown [28] that a divergent beam experiment is equivalent to a parallel beam geometry when introducing an effective pixel size p_{eff}, which is the physical pixel size p_s divided by the magnification M. Furthermore, the propagation distance z is replaced by an effective propagation distance z_{eff}. M and z_{eff} are defined as follows [28, 29]:

$$M = \frac{z_1 + z_2}{z_1}, \quad z_{eff} = \frac{z_1 z_2}{z_1 + z_2} \tag{4.6}$$

where z_1 is the distance from the focal point of the beam to the sample and z_2 is the distance from the sample to the detector as shown in Fig. 4.1. Experimentally, a divergent beam geometry can be achieved in different ways. It has been described for hard X-ray synchrotron radiation using wave guides (WG) [28–30], compound refractive lenses (CRL) [31–33] and Kirkpatrick-Baez-mirrors (KB) [26, 27]. For
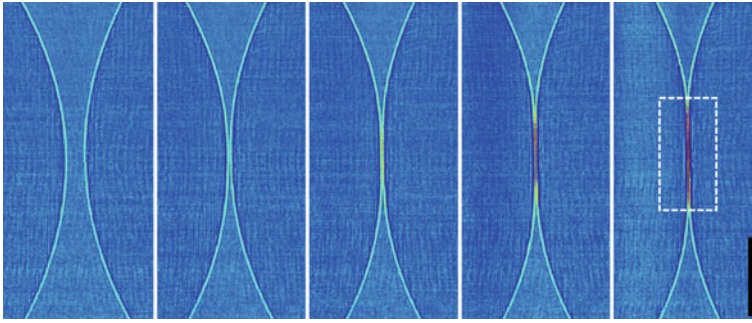
**Fig. 4.4** Two lipid monolayers are brought together by controlled pumping through the microfluidic channel. The contrast between the aqueous and oil phase can be clearly seen in the leftmost image. The structure in the dashed box is of interest in the current investigation. The scale bar is 50 microns

point-like, also called micro-focus, lab sources various approaches are presented in literature [34–36].

4.3.3 Data Analysis and Fitting

The images resulting from the process of lipid membrane formation by bringing two oil-water interfaces are shown in Fig. 4.4. It can already be seen that a single oil-water interface decorated by a lipid monolayer leads to a significant phase contrast. While the diffraction due to this single lipid monolayer can be analysed using an asymmetric phase slit model [37], the focus of this present investigation is the lipid membrane. The diffraction pattern due to such a membrane can also be seen with a maximum in the center with symmetric peaks on either side of this maxima. This is to be expected from the symmetry of the bilayer structure that is formed in the microfluidic channel.

From such an image, a one-dimensional profile of the diffraction intensity is constructed by taking an average over a certain region of interest as shown in Fig. 4.5. Data fitting is then performed in MatLab using a χ^2-minimization algorithm called "Nelder-Mead simplex method" [38]. The image formation, as described earlier is determined by a few main parameters viz. the thickness of the lipid membrane d, the refractive index difference $\Delta\delta$ and the effective propagation distance z_{eff}. While the difference in the refractive indices $\Delta\delta = \delta_{BLM} - \delta_{H_20}$ is calculated using the literature electron density values of water, solvent, and lipids, giving $\Delta\delta \sim -1.23 \times 10^{-7}$. The propagation distance z_{eff} is defined by the experimental setup as discussed earlier. The computational details and the source codes of the algorithms used in the fitting procedure are described in an earlier thesis [37].
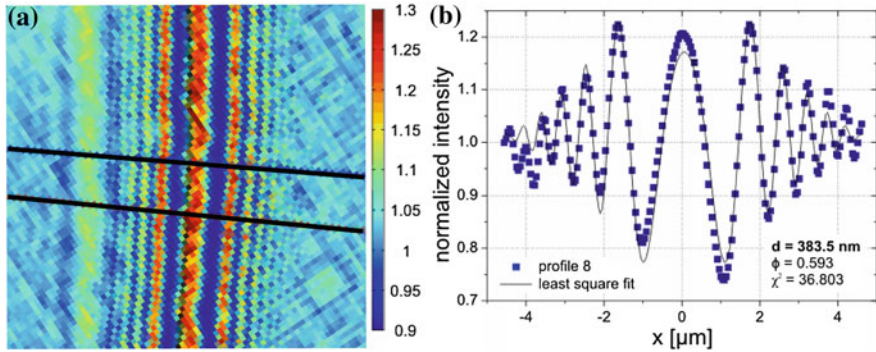
Fig. 4.5 a Diffraction pattern of a microfluidic bilayer membrane prepared from a Monoolein-squalene solution/water at an effective propagation distance of 29.67 mm. The Fresnel fringes are highly visible at high deflection angles. Glue residues at the surface of the self-adhesive kapton window material produce parasitic features in the image. **b** The profile between the black lines is extracted from the region of interest (ROI) in **a**. Due to planar sample geometry it can be fitted using a symmetric phase slit model [11], which is characterized by the phase shift ϕ and the thickness d.

The state of the membrane is such that there is a lot of solvent remaining between the lipid monolayers and the visibility of Fresnel fringes is therefore relatively high. A one-dimensional diffraction profile is extracted by averaging over the region between the two black lines as shown in Fig. 4.5a. A least-squares fit together with the extracted profile is depicted in 4.5b.

The symmetry of the intensity profile can be explained by the geometry of the lipid membrane, as mentioned earlier. A pressure gradient Δp across the membrane induced by the two pumps driving the aqueous fingers will always cause the membrane shift inside the channel. When the pumps are stopped, removing any pressure difference i.e. $\Delta p = 0$, the membrane stays at a fixed position and in this position it reaches a planar orientation in order to minimize its surface tension. Since it is composed of symmetric monolayers, we can explain the symmetry of the intensity pattern in the same way, as for parallel beam thinning series by using a symmetric phase slit approach [10]. The membrane thickness extracted from the fitting procedure gives $d = 383.5$ nm and is large, as expected due to the interstitial oil between the lipid monolayers. The fit result of $\phi = 0.593$ can be used to calculate the path length of the X-rays through the membrane. According to Eq. 4.2 we get

$$L = \frac{\phi}{-k\,\Delta\delta} = \frac{0.593}{8.872 \times 10^4 \cdot 1.23 \times 10^{-7}}\ \mu m = 54.3\ \mu m, \qquad (4.7)$$

which at the same time corresponds to the diameter of the membrane patch, considering that the contact area of the two fingers leads to a flat circular membrane patch. This value appears to be quite reasonable for a channel depth of 300 μm as also seen in Fig. 4.4. It can be seen in Fig. 4.5b that the fit shows slight deviations from the actual profile in the central region. It is also not able to catch the slight asymmetry of
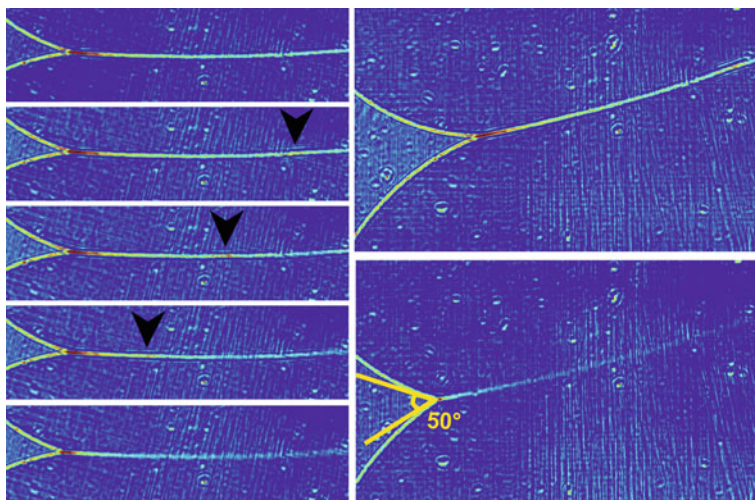
Fig. 4.6 *Left* Image series of the "zipper-like" effect, which occurs during the transformation from a bulk film to a bimolecular membrane from *top* to *bottom*. *Right* The migration of solvent and the formation of a bilayer membrane leads to a change in the opening angle between the lipid monolayers at the start of the lipid bilayer as shown

the first order minima. The phase contrast image in Fig. 4.5a reveals structures which are related to residues of glue on the self-adhesive kapton foil. These can induce parasitic scattering, which contributes to the diffraction pattern of the membrane and leads to deviations from the theoretical intensity profile, as obtained in the extracted profile. In the absence of glue on the kapton surface, i.e. in previous experiments where bulged BLMs [10] were investigated, such features were not observed.

Next, we look at the zipping process of bilayer formation as discussed in Chap. 2. A sequence in Fig. 4.6, shows the phase contrast images of the zipping process. A droplet of oil (marked by the black arrow), traverses rapidly, forming a molecular bilayer in its wake. The final state of the bilayer is characterised by the opening angle at the Plateau-Gibbs border, and as discussed in Chap. 2, this depends on the interfacial tension at the oil-monoolein-squalane interface. As we found previously in Chaps. 2 and 5, this opening angle is found to be $\sim 50^\circ$ from the phase contrast images.

Figure 4.7 shows the transition region between the Plateau-Gibbs border (PGB) and the bimolecular region of a lipid membrane, which has recently formed as described above. We now seek to quantitate the thickness variations during this process. The fresnel fringes close to the PGB are much more strongly pronounced than in the thinner regions. *Profile 9* in Fig. 4.7b is extracted from a position in Fig. 4.7a, where a domain of residual organic solvent just migrates towards the PGB. Figure 4.7c shows *profile 10*, which is extracted from a ROI in the transition region. Here the fringe visibility is already poor.
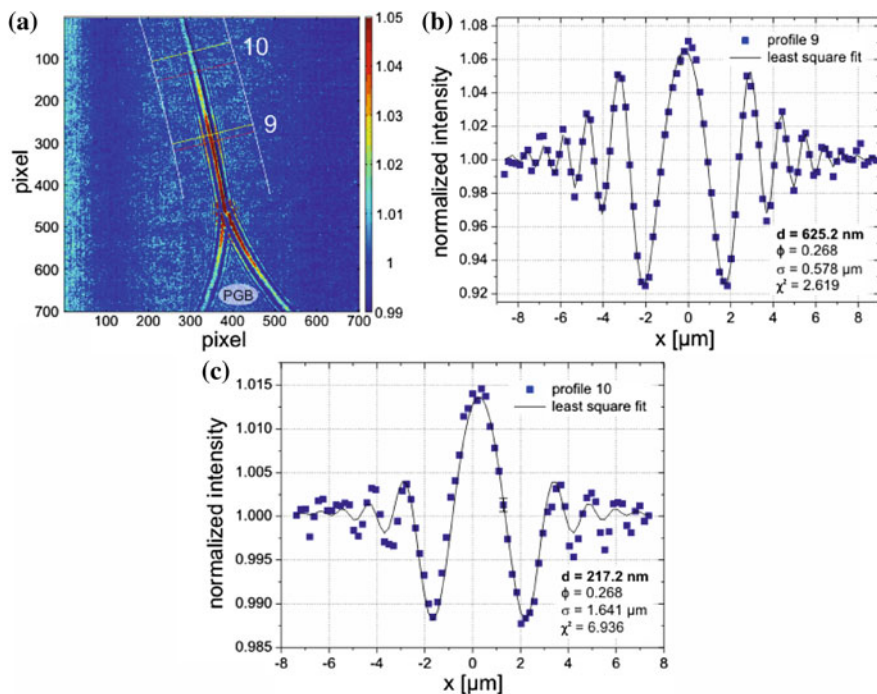
Fig. 4.7 **a** Diffraction pattern of the transition region during the "zipper-like" effect of a microfluidic lipid membrane close to the Plateau-Gibbs border (PGB) (Monoolein-squalane/water, $z_{eff} = 94.21$ mm). The Fresnel fringes disappear in regions where the membrane has already thinned and only a single maximum is left. **b** *Profile 9*, along with a reasonable least-squares fit, showing a large thickness at the position of a thick, domain of residual solvent. **c** *Profile 10*, which is located close to the bimolecular membrane region, cannot be fitted comparably accurately due to a notable contribution of the PGB to the diffraction pattern
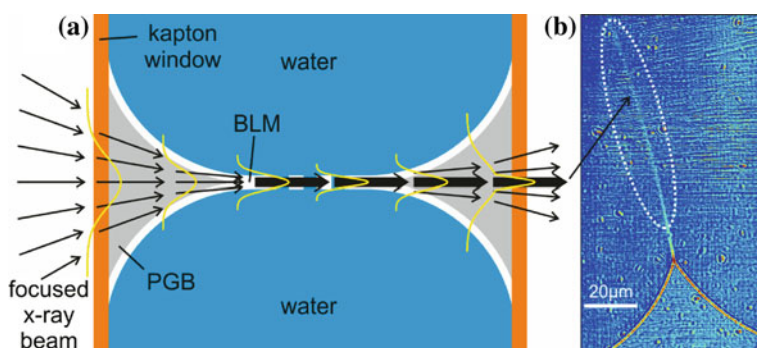
Fig. 4.8 **a** Schematic representation of the "focusing" effect of the Plateau-Gibbs border. This results in an intensity maximum in (**b**) at the position of the thinned membrane. Images of **b** data: *hunt01-7150*, background: *hunt01-10049*

Regarding the fit result of $d = 625.2$ nm for *profile 9*, it is much larger than for the profile extracted in Fig. 4.5. This is due to the smaller $\phi = 0.268$, which only gives a path length $L = 24.559\,\mu$m for the X-rays to travel through the film. Regarding *profile 10*, which is depicted in Fig. 4.7c, we obtain a dominant contribution of the central maximum. Compared to this the higher order oscillations only have little intensity. To match this strong decay the fit algorithm increases the Full Width at Half Maximum (FWHM) of the Lorentzian up to $\sigma = 1.614$, while it is only $\sigma = 0.578$ in *profile 9*. Consequently, the intensity is strongly decreased, which can only be compensated by an increase in the thickness. A value of $d = 217.2$ nm is unexpectedly high for a profile at a position so close to the bilayer part of the film. However, when *profile 10* is fitted with the σ value of *profile 9*, we obtain a reasonable thickness of 78.4 nm. Except for the central maximum, the higher order fringes are fitted much more accurately with this constraint. The schematic representation in Fig. 4.8a gives a possible explanation for the intensity observed after the membrane has thinned (see Fig. 4.8b). We consider it as a "focusing" effect of the Plateau-Gibbs border. The impinging X-rays are reflected at the PGB-water interface, to be guided to the contact region of the two monolayers where they are concentrated. The resulting image at the detector can be considered as a superimposition of the diffraction pattern and the central intensity peak. The dominance of the latter is the reason why the thinned state of the lipid bilayer, which will show intensity variations of only 0.1 %, cannot be observed in any of the diffraction patterns.

4.4 Summary and Outlook

Direct imaging of lipid bilayers in both their native and reconstituted environments is a significant challenge with wide ranging implications. The work described in this chapter demonstrates a first step towards imaging lipid bilayers reconstituted in microfluidic channels. The wide applicability of the techniques of microfluidics in a variety of interdisciplinary studies makes such an investigation vital. Our data shows that it is possible to image an unthinned lipid membrane with resolutions down to $\sim$200 nm in one dimension. It should be pointed out that the reconstituted bilayers did not undergo any beam damage during the experiments. This is remarkable in spite of the high photon flux in the focused beam experiments, with a flux density of $\sim 10^{19}\frac{\text{photons}}{\text{mm}^2\text{s}}$. Further, the Plateau-Gibbs border limits the the resolution of a native bilayer membrane using the current simple theoretical model of the lipid bilayer in such a setting. However, a modification to the model to include the possible focussing effect of the PGB might lead to a more detailed extraction of the relevant structural information from the images. An interesting possibility in the future would be to incorporate giant unilamellar vesicles (GUVs), as a solvent free membrane system within microfluidic channels for high resolution studies of the interactions and fusion of lipid bilayers. The control and precision offered

by microfluidic techniques would indeed provide a significant advantage to such studies.

References

1. J.C. Weaver, Electroporation of biological membranes from multicellular to nano scales. IEEE Trans. Dielectr. Electri. Insul. **10**, 754–768 (2003)
2. Z. Vasilkoski, A. Esser, T. Gowrishankar, J. Weaver, Membrane electroporation: the absolute rate equation and nanosecond time scale pore creation. Phys. Rev. E **74**, 1–12 (2006)
3. T.D. Xie, T.Y. Tsong, Study of mechanisms of electric field-induced DNA transfection III. Biophys. J. **63**, 28–34 (1992)
4. R. Egerton, *Physical Principles of Electron Microscopy: An Introduction to TEM, SEM, and AEM* (Springer, New York, 2005)
5. B. Huang, H. Babcock, X. Zhuang, Breaking the diffraction barrier: super-resolution imaging of cells. Cell **143**, 1047–1058 (2010)
6. J. Lippincott-Schwartz, S. Manley, Putting super-resolution fluorescence microscopy to work. Nat. Meth. **6**, 21–23 (2009)
7. C. Bergemann, H. Keymeulen, J.F. van der Veen, Focusing X-ray beams to nanometer dimensions. Phys. Rev. Lett. **91**, 204801 (2003)
8. C. Schroer, B. Lengeler, Focusing hard X-rays to nanometer dimensions by adiabatically focusing lenses. Phys. Rev. Lett. **94** 054802 (2005)
9. C.G. Schroer, P. Boye, J.M. Feldkamp, J. Patommel, A. Schropp, A. Schwab, S. Stephan, M. Burghammer, S. Schöder, C. Riekel, Coherent X-ray diffraction imaging with nanofocused illumination. Phys. Rev. Lett. **101**(9), 090801 (2008)
10. A. Beerlink, M. Mell, M. Tolkiehn, T. Salditt, Hard X-ray phase contrast imaging of black lipid membranes. AIP Conf. Proc. **1236**, 220 (2010)
11. A. Beerlink, *Black lipid membranes studied by X-ray phase contrast imaging, Göttingen Series in X-ray Physics*, vol. 1 (Universitätsverlag Göttingen, 2011)
12. O. Hignette, Submicron focusing of hard X-rays with reflecting surfaces at the ESRF, in *Proceedings of SPIE*, San Diego, 2001, pp. 105–116
13. A. Rommeveaux, Mirror metrology and bender characterization at ESRF, in Proceedings of SPIE, San Diego, 2005, pp. 59210N–59210N-8
14. J. Labiche, O. Mathon, S. Pascarelli, M.A. Newton, G.G. Ferre, C. Curfs, G. Vaughan, A. Homs, D.F. Carreiras, The fast readout low noise camera as a versatile X-ray detector for time resolved dispersive extended X-ray absorption fine structure and diffraction studies of dynamic problems in materials science, chemistry, and catalysis. Rev. Sci. Instrum. **78** (2007)
15. A. Cecilia, A. Rack, D. Pelliccia, P.A. Douissard, T. Martin, M. Couchaud, K. Dupre, T. Baumbach, Studies of LSO:Tb radio-luminescence properties using white beam hard X-ray synchrotron irradiation. Radiat. Eff. Defects Solids **164**, 517–522 (2009)
16. T. Martin, P. Douissard, M. Couchaud, A. Cecilia, T. Baumbach, K. Dupre, A. Rack, LSO-based single crystal film scintillator for synchrotron-based hard X-ray micro-imaging. IEEE Trans. Nucl. Sci. **56**, 1412–1418 (2009)
17. L.G. Parratt, Surface studies of solids by total reflection of X-rays. Phys. Rev. **95**, 359 (1954)
18. J. Als-Nielsen, D. McMorrow, *Elements of Modern X-ray Physics*, 1st edn. (Wiley 2001)
19. P. Cloetens, *Contribution to Phase Contrast Imaging Reconstruction and Tomography with Hard Synchrotron Radiation*. Ph.D., Vrije Universiteit Brussel, 1999.
20. D. Paganin, *Coherent X-ray Optics* (Oxford University Press, USA, 2006)
21. K.A. Nugent, Coherent methods in the X-ray sciences. Adv. Phys. **59**(1), 1 (2010)
22. M. Born, E. Wolf, *Principles of Optics: Electromagnetic Theory of Propagation, Interference and Diffraction of Light*, 7th edn. (Cambridge University Press, Cambridge, 1999)

23. P. Cloetens, R. Barrett, J. Baruchel, J. Guigay, M. Schlenker, Phase objects in synchrotron radiation hard X-ray imaging. J. Phys. D: Appl. Phys. **29**, 133–146 (1996)

24. J. Cowley, *Diffraction Physics*, 3rd edn., North-Holland Personal Library, Elsevier (1995)

25. A. Snigirev, I. Snigireva, V. Kohn, S. Kuznetsov, I. Schelokov, On the possibilities of X-ray phase contrast microimaging by coherent high-energy synchrotron radiation. Rev. Sci. Instrum. **66**(12), 5486 (1995)

26. R. Mokso, P. Cloetens, E. Maire, W. Ludwig, J. Buffière, Nanoscale zoom tomography with hard X-rays using Kirkpatrick-Baez optics. Appl. Phys. Lett. **90**(14), 144104 (2007)

27. P. Bleuet, P. Cloetens, P. Gergaud, D. Mariolle, N. Chevalier, R. Tucoulou, J. Susini, A. Chabli, A hard X-ray nanoprobe for scanning and projection nanotomography. Rev. Sci. Instrum. **80**(5), 056101 (2009)

28. C. Fuhse, X-ray waveguides and waveguide-based lensless imaging. Ph.D. thesis, 2006

29. S. Lagomarsino, A. Cedola, P. Cloetens, S.D. Fonzo, W. Jark, G. Soullié, C. Riekel, Phase contrast hard X-ray microscopy with submicron resolution. Appl. Phys. Lett. **71**(18), 2557 (1997)

30. S.D. Fonzo, W. Jark, G. Soullié, A. Cedola, S. Lagomarsino, P. Cloetens, C. Riekel, Submicrometre resolution phase-contrast radiography with the beam from an X-ray waveguide. J. Synchrotron Radiat. **5**, 376–378 (1998)

31. C. Raven, A. Snigirev, I. Snigireva, P. Spanne, A. Souvorov, V. Kohn, Phase-contrast microtomography with coherent high-energy synchrotron X-rays. Appl. Phys. Lett. **69**(13), 1826 (1996)

32. B. Lengeler, C.G. Schroer, M. Richwin, J. Tümmler, M. Drakopoulos, A. Snigirev, I. Snigireva, A microscope for hard X-rays based on parabolic compound refractive lenses. Appl. Phys. Lett. **74**(26), 3924 (1999)

33. C.G. Schroer, J. Meyer, M. Kuhlmann, B. Benner, T.F. Günzler, B. Lengeler, C. Rau, T. Weitkamp, A. Snigirev, I. Snigireva, Nanotomography based on hard X-ray microscopy with refractive lenses. Appl. Phys. Lett. **81**(8), 1527 (2002)

34. S. Mayo, T. Davis, T. Gureyev, P. Miller, D. Paganin, A. Pogany, A. Stevenson, S. Wilkins, X-ray phase-contrast microscopy and microtomography. Opt. Express **11**(19), 2289–2302 (2003)

35. T. Tuohimaa, M. Otendal, H.M. Hertz, Phase-contrast X-ray imaging with a liquid-metal-jet-anode microfocus source. Appl. Phys. Lett. **91**(7), 074104 (2007)

36. M. Otendal, T. Tuohimaa, U. Vogt, H.M. Hertz, A 9 keV electron-impact liquid-gallium-jet X-ray source. Rev. Sci. Instrum. **79**(1), 016102 (2008)

37. M. Mell, *Phase Contrast Imaging of Lipid Bilayer Model Membranes using Hard X-Rays*. Diploma, Göttingen University, 2009.

38. J.C. Lagarias, J.A. Reeds, M.H. Wright, P.E. Wright, Convergence properties of the Nelder-Mead simplex method in low dimensions. SIAM J. Optim. **9**, 112–147 (1998)

Chapter 5
Oscillating Droplets: Chemical Micro-Oscillators

Emulsion droplets running the Belousov-Zhabotinsky reaction form chemical micro-oscillators and their coupling / synchronization behaviour via bilayer membranes is discussed.

5.1 Introduction

The synchronization of coupled oscillators is a striking manifestation of self-organization that nature employs to orchestrate essential processes of life, such as the beating of the heart. Chemical reaction-diffusion processes have been paradigmatic systems in understanding such synchronization. The most thoroughly studied oscillating chemical reaction is the so-called Belousov-Zhabotinski (BZ) reaction [1–3]. There are several formulations which have been used. Most of them contain an autocatalytic step decomposing bromate (BrO_3^-) as the main educt, with the help of an oxidizer, such as Fe^{III} ions. The reduction of the Fe^{II} to Fe^{III} provides an optical indicator for this step, which can be enhanced by using the ferroin complex as a carrier for the Fe ions. The progress of the reaction is then accompanied by a color change from deep red to light blue. The product, BrO_2^-, acts as a catalyst, or 'promotor' in this first step. A second step involving malonic acid is coupled to this system, which by re-oxidizing the Fe^{III} to Fe^{II} produces bromine ions. The latter react with the BrO_2^- promotor to yield BrO^- as the final product. The bromine thus scavenges the promotor of the autocatalytic step, and is therefore considered as the 'inhibitor'.

After having been almost unrecognised after its discovery for many years, the BZ reaction has later become one of the paradigm systems for dynamical systems and

self-organization. In spatially extended settings, the BZ reaction gives rise to complex propagating wave patterns, which are reminiscent of spatio-temporal patterns known from other catalytic systems driven far off thermal equilibrium [4, 5]. Coupled BZ oscillators have previously been studied in the laboratory with large reactors connected directly by small channels for controlled mass exchange of bulk solution. In this case, coupling occurs via all species. In living systems, however, coupling often occurs through special signalling molecules, as in synaptic communication. Collections of neural oscillators can access a vast repertoire of coordinated behavior by utilizing a variety of topologies and modes of coupling, including gap junctions and synaptic links, which may be either excitatory or inhibitory, depending on the neurotransmitter involved. In small containers, however, where diffusive coupling across the container is strong, the BZ reaction containers behave like single homogeneous oscillators. It then suggests itself to consider larger ensembles of such coupled BZ oscillators as analogous to, e.g., systems of firing neurons.

It has been shown before that systems like that can be nicely realized by using aqueous droplets containing the BZ educts as the oscillators, and coupling them via an oil phase separating the droplets [6]. Both the promotor and the inhibitor are sufficiently hydrophobic to enter the oil phase easily, such that they can diffuse from one droplet to the other if they are sufficiently close. The delicate balance of promotive and inhibitory coupling gives rise to a wealth of oscillation patterns [7]. They strongly differ from the wave-like patterns which are well-known from continuous systems, and are as yet not fully understood. In this chapter, we investigate whether we can distinguish coupling through the bulk oil phase from coupling through a bilayer membrane (formed between droplets as discussed in Chap. 2), and to investigate what types of coupling can be achieved solely via the latter.

5.2 Experimental Techniques

Our chemical oscillators are made from incorporating the BZ reaction mixture in aqueous droplets in an external oil phase of squalane contaning mono-olein as surfactant. The droplets are for these experiments are made using a flow focussing channel geometry in a PDMS microfluidic chip as shown in Fig. 5.1. In order to prevent any pre-reaction and the formation of unwanted gaseous bubbles of carbon-di-oxide, the BZ reaction mixture is separated into two parts and they are combined on chip. The two parts are created in stock with concentrations as follows: (i) 500 mM sulphuric acid (H_2SO_4) and 280 mM sodium bromate ($NaBrO_3$) (ii) 300–800 mM malonic acid ($C_3H_4O_4$) and 3 mM ferroin ($C_{36}H_{24}FeN_6O_4S$). The concentration of the mono-olein in the squalane ranges between 25–100 mM.

As can be seen from the left panel of Fig. 5.1, the BZ reaction consists of an autocatalytic cycle in which the species $HBrO_2$ catalyses its own production via the reduction of the ferroin catalyst which changes its colour rapidly from red to blue in response. This is when the inhibitory cycle proceeds, leading to a slow production of bromine which quenches the autocatalysis. The effect of this is a gradual change
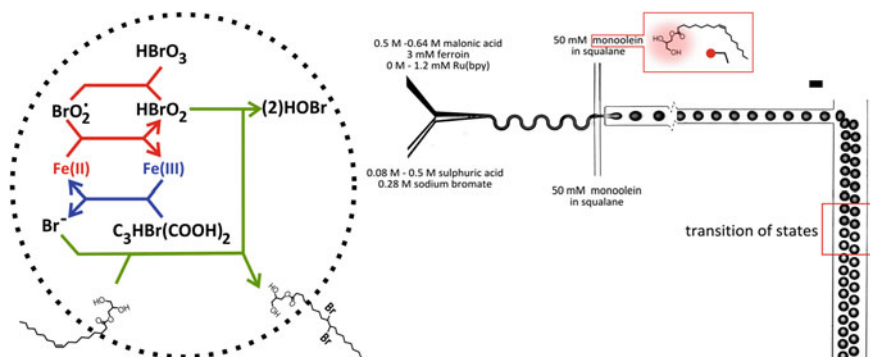
Fig. 5.1 Production of monodisperse oscillator droplets. *Left* The BZ reaction consists of two loops (i) an autocatalytic and (ii) an inhibitory cycle. The reaction state can be visualised by the colour of the ferroin catalyst. In our setting, an additional reaction with the unsaturated mono-olein surfactant occurs as shown. *Right* The contents of the BZ reaction are mixed on the microfluidic chip to prevent any pre-reaction. Seen through an optical 480/20 nm notch filter, the transition from *red colour* to the *blue colour* of the BZ reaction is seen by the change in the brightness of the droplet
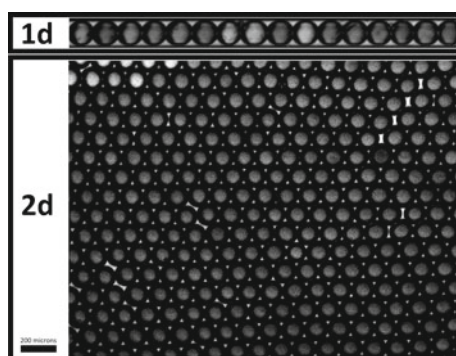
Fig. 5.2 Storage of droplet oscillations in one and two dimensional confinement for observation of their dynamics

of the catalyst back from the blue colour to red. In addition to this classical BZ reaction, in our case, due to the addition of the surfactant mono-olein to stabilise the droplets an additional side reaction occurs. Since the surfactant has an unsaturated hydrocarbon chain as shown, some of the bromine that is produced in the inhibitory cycle rapidly reacts with the unsaturated bond. As we will see below, this 'trapping' of the bromine by the surfactant significantly affects the coupling between droplet oscillators in our setup.

The droplet oscillators are stored as a monolayer in either a 1d or 2d array as shown in Fig. 5.2. The 1d array is created within a glass capillary with a square cross-section of inner width 100 μm and outer width 135 μm (Hilgenberg GmbH, Germany). The inner walls of the capillary are hydrophobised using a commerically
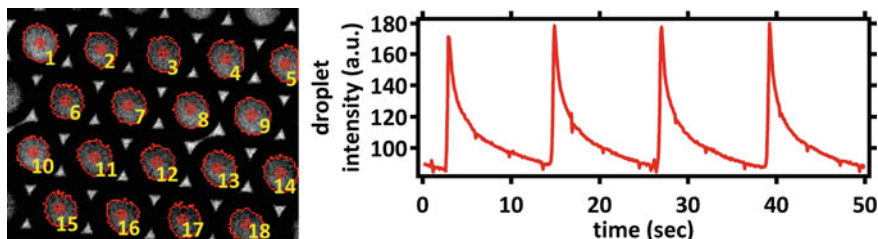
Fig. 5.3 Image processing to identify the droplet oscillators and record their dynamics

available Nano-protect coat. The 2d array is created between two hydrophobised glass slides with a PDMS spacer. The reaction dynamics are recorded by video microscopy on an inverted microscope (Olympus IX 81) through an appropriate optical filter. As described earlier, the BZ reaction dynamics can be followed by the colour of the catalyst as it changes from red to blue and vice versa. The optical filter we chose is therefore a notch filter of 480/20 nm wavelength such that the red colour of the catalyst has less transmittance through the filter. Droplets are identified from the recorded images using Image-Pro Plus (Media Cybernetics) as shown in Fig. 5.3 (left panel). The BZ oscillations within the droplet are then identified by measuring the mean intensity value of the droplet. The temporal BZ oscillations are then seen are traces similar to those of a relaxation oscillator as seen in the right panel of Fig. 5.3. The sudden rise of intensity corresponds to the autocatalytic cycle of the BZ reaction with the catalyst changing from red to blue colour and the gradual fall in intensity corresponds to the gradual release of bromine in the reaction and the changing back of the catalyst colour from blue to red. Further analysis on the obtained data as described in the results section is done using MATLAB.

5.3 Results

5.3.1 Isolated BZ Oscillators

The BZ oscillators described here are a closed reactor system i.e. there is no mass flux during the reaction. Therefore all the reactants and the resultant products remain within the droplet. As a result, the nature of the oscillations gradually changes with time. As soon as the experiment is started, the oscillation is set by the initial reaction conditions and the amplitude of the oscillations and the frequency change as time proceeds. This can be seen in Fig. 5.4. As time proceeds, the amplitude of the oscillations reduces significantly till they die out completely. The frequency of the oscillation, shown in black, gradually reduces. However, over the duration of the experiment, the frequency reduces to only with a few percent (in this case 10 %, over the observation of 50 oscillation cycles) and for the studies made in this work, can
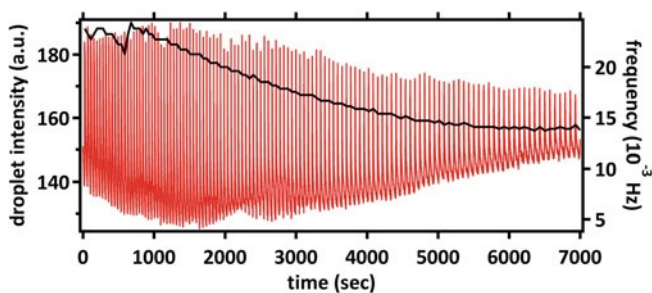
Fig. 5.4 BZ oscillations in a closed reactor. The oscillation trace and its corresponding frequency (*black*) are plotted as a function of time

be considered constant. As mentioned before, the BZ oscillations display two time scales, characteristic of a relaxation oscillator. The fast time scale in the order of 1 s corresponds to the rapid autocatalytic production of $HBrO_2$. The frequency of the oscillation is then set by the slow production of bromine resulting the the decay of the droplet intensity. Due to the presence of the surfactant mono-olein in our system, the bromine cycle is modified from the classical version of the BZ reaction and therefore, we see an effective decrease of frequency for the oscillator droplets compared to the experiments in bulk.

The BZ oscillators are suspended in an oil phase consisting of squalane, with mono-olein at concentrations well above the critical micelle concentration (CMC). The mono-olein serves two purposes. First, it forms dense surfactant layers at the oil/water interface and readily form bilayer membranes, as seen in Chap. 2. Second, the C=C double bond in the mono-olein molecule acts as an efficient scavenger for bromine, since the latter rapidly reacts with this site. The oil phase is thus expected to efficiently suppress coupling between neighboring droplets, which is mediated by the exitatory and the inhibitory species as described earlier. That this is indeed the case can be seen in Fig. 5.5 which shows a two dimensional hexagonal packing of BZ oscillators. The spherical shape of the droplets in the packing clearly shows that there is oil between the droplets and that bilayer membranes have not formed which are characterised by increased contact angle of the surfactant monolayers as described in Chap. 2. The oscillation trace of a single oscillator is shown in the lower panel of Fig. 5.5 and in our experiments we do not see a systematic dependance of the droplet size on the oscillation frequency. This could be because for a certain concentration of the BZ educts, as long as the droplet size is below the typical wavelength of the BZ wave, there should not be a change in the temporal frequency. When such isolated droplets are close to each other, in spite of the fact that the diffusion of the excitatory and inhibitory species can indeed cause coupling between droplet, they remain uncoupled. This is due to the fact that as we discussed before, they might be trapped via a reaction with the surfactant molecules.

However, bilayer membranes form spontaneously between the droplets as described in Chap. 2 and this happens in the case of the droplet oscillators too. As
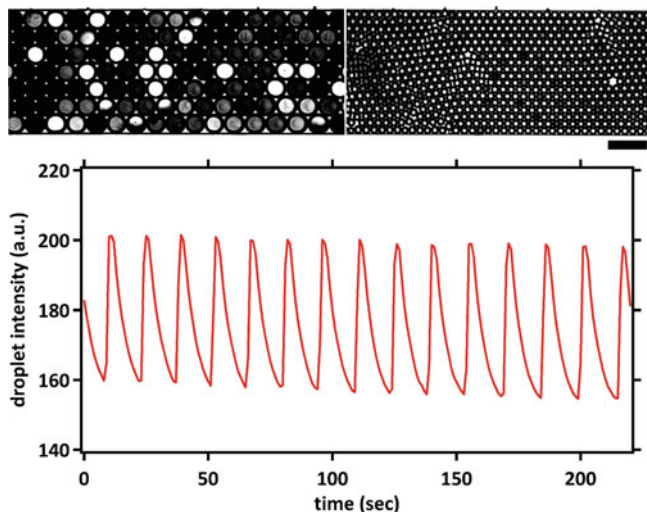
Fig. 5.5 Droplet oscillators in a hexagonal packing geometry within a PDMS microchannel. *Top* The different intensities of the droplets show the different BZ reaction states within each droplet for two different droplet sizes. Each droplet acts like an isolated individual oscillator without any coupling with its neighbours. Image contrast is enhanced for better visualization. Scale bar is 150 μ. *Bottom* The intensity trace for a single droplet is shown as a function of time. The constancy of the frequency and amplitude of the oscillations can be clearly seen

soon as bilayers form between droplets, their interfaces touch each other very closely such that the droplets are not perfectly spherical anymore. Due to this, the packing fraction increases as seen in Fig. 5.6. Once the bilayers are formed, completely different oscillatory dynamics are seen. Often, waves of synchronised activity such as travelling waves are seen as in Fig. 5.6. Therefore we see a switch from the individual to collective dynamics of the oscillators when bilayer networks are formed. We discuss this aspect in greater detail in the next section.

5.3.2 Membrane Formation Triggers Oscillator Coupling

As soon as a bilayer has formed, coupling is expected to commence rapidly. Most of the mono-olein molecules forming the membrane have been exposed to the reaction products of the BZ system before and will thus be brominated already when the membrane forms. But even if the latter was formed with fresh mono-olein, it would be readily saturated with bromine given its minute thickness, and thus would let further bromine compounds pass easily.

The strong variation in coupling strength by membrane formation can be seen most impressively in excitatory waves propagating in rafts of BZ droplets with a yet incomplete network of bilayer membrane contacts. Figure 5.7 shows snapshots
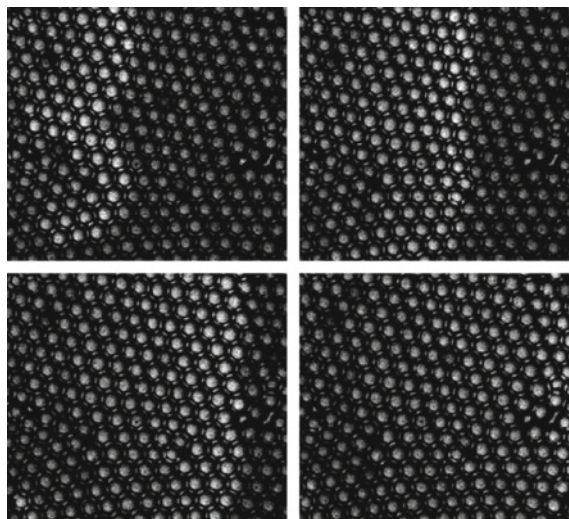
Fig. 5.6 The formation of travelling waves when bilayer membranes are formed between oscillator droplets. Each image is 5 s apart. The droplet diameter is 30 μ
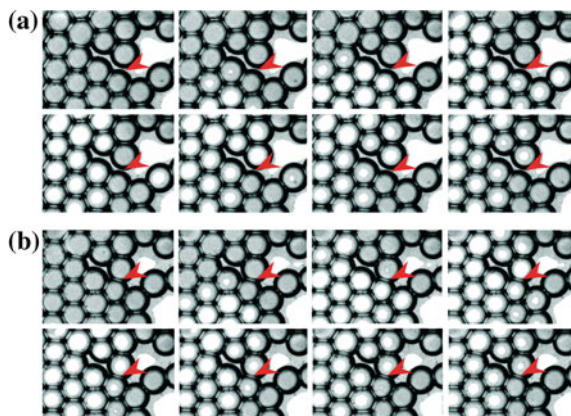
Fig. 5.7 Demonstration of the influence of membrane coupling on an excitation wave in a larger raft of droplets. The oil phase consists of squalane with 50 mM/l mono-olein. The aqueous phase is 0.5 M sulphuric acid, 280 mM sodium bromate, 0.5 M malonic acid, and 3 mM ferroin. **a** The droplet surfaces indicated by the *red arrow* are very close, but there has yet no membrane been formed. The excitation wave (coming from below) passes around the *arrow*, the excitation does not directly cross the gap between the two droplets. **b** After the membrane has formed, the excitation wave passes through the site indicated by the *arrow*

of such a wave of excitation (i.e., of a sudden increase in transmittance) which propagates from bottom to top in a moderately dense raft of droplets. The top and bottom row each shows a time lapse representation of a single excitation wave. The
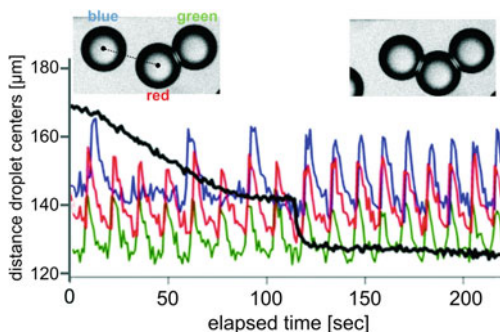
Fig. 5.8 Effect of membrane formation upon the phase coupling of chemical oscillators. The *blue*, *red*, and *green* trace represent the transmittance of the three droplets shown in the *insets* as a function of time. The *black curve* shows, on the same time axis, the distance of the '*blue*' from the '*red*' droplet (measured center-to-center). Clearly, the oscillations couple in phase as soon as the membrane is formed (jump in the *black curve*), but not before

red arrow points to a droplet/droplet contact which in the top row has not yet formed a membrane, but in the bottom row it has. A close inspection shows that in the top row, the wave travels around the point of the red arrow. In the bottom row, however, it passes this contact without noticeable hesitation.

In order to demonstrate the change in oscillator dynamics before and after coupling, we observed the oscillation behavior of BZ droplets while they were diffusively moving relative to each other, finally forming bilayer membranes. Figure 5.8 shows the transmittance traces of three droplets, exhibiting the spike pattern characteristic of the BZ oscillation. The auto-catalytic reaction step which reduces the strongly absorbing Fe^{III} to the almost clear Fe^{II} solute leads to a steep increase of the transmittance. This is followed by a smooth decrease due to the gradual re-oxidation of the Fe^{II} involving the malonic acid. Initially, only the two droplets whose transmittance traces are shown in red and green are connected by a bilayer membrane. This was known from the direct observation of the membrane forming process. The third droplet, the transmittance trace of which is shown in blue, had some distance to the first pair, with about 50 μ surface separation from the 'red' droplet. A large oil volume fraction was used in this sample, such that the droplets could diffuse freely for some distance. Clearly, the red and green transmittance traces are phase locked, while the blue trace follows its own pace, showing no sign of influence from the other two for the first ≈100 s shown. The black curve represents the distance of the centers of the 'red' and 'blue' droplets, as determined from fitting circles to their images. It shows how the 'blue' droplet gradually drifts towards the 'red'. At around 100 s, the surfaces of the droplets have come so close that the drift is stopped due to the diverging hydrodynamic resistance of the flat sphere-to-sphere contact. At about 113 s, the droplet centers are rapidly pulled together, which we interpret as the formation of the bilayer membrane (cf. Fig. 2.5).

In order to verify this interpretation, we can estimate the contact angle forming at the three phase contact line, from the height of the jump in the droplet center distance. If $\tilde{R}$ is the radius of the droplet after the membrane has formed, i.e., the radius of an ideal sphere fitted to the free droplet surface, it is easily shown that the volume of the flattened droplet is given by

$$V(\theta) = \frac{\pi \tilde{R}}{3} \left(2 + 3\cos\frac{\theta}{2} - \cos^3\frac{\theta}{2} \right) \tag{5.1}$$

where θ is defined as above. If D is the distance of the sphere centers after membrane formation, we furthermore have $D = 2\tilde{R}\cos\theta$. Denoting by R the radius of the droplets before membrane formation, we finally obtain using volume conservation

$$\frac{2}{\cos^3\theta} + \frac{3}{\cos^2\theta} = 1 + 4\left(\frac{R}{D}\right)^3 \tag{5.2}$$

From the height of the jump in the black curve in Fig. 5.8, we obtain $2R/D \approx 1.107$ and thus $\theta \approx 51°$, in reasonable agreement with the value found in Chaps. 2 and 4.

Here we are particularly interested in the change in coupling induced by the membrane formation. Clearly, we see that after the jump in the black curve, all three transmittance traces are firmly coupled. It seems that due to the presence of the mono-olein double bonds in the oil phase, an efficient transport of bromine as a messenger through the oil phase is prevented effectively. Transport through the mono-olein bilayer membrane, however, is obviously still possible.

5.3.3 Synchronization Patterns

Patterns such as pacemaker driven target waves, travelling waves and spirals are most commonly seen in large assemblies of coupled oscillators. The BZ droplet oscillators, connected by bilayer membranes, also give rise to such a rich range of collective dynamics. In the present section, we discuss, qualitatively, the various patterns that emerge in connected networks of oscillators and the dependance on the network topology of the type of behaviour that emerges. The discreteness of the droplet oscillators allows us to find clear trigger locations in the networks. All the following experiments are done with a BZ reaction mixture as described in the experimental section, with a malonic acid concentration of 500 mM.

First, we discuss the formation of target waves. Target waves are characterised by a pacemaker core which periodically tiggers excitatory waves that spread from the core center outward. In our system, we observe that pacemakers spontaneously emerge in the center of connected droplet 'islands' or 'peninsulas'. An 'island' is comprised of connected droplets as shown in the left panel of Fig. 5.9 with the outer edges of the 'island' open to the mono-olein filled oil phase. A 'peninsula' is
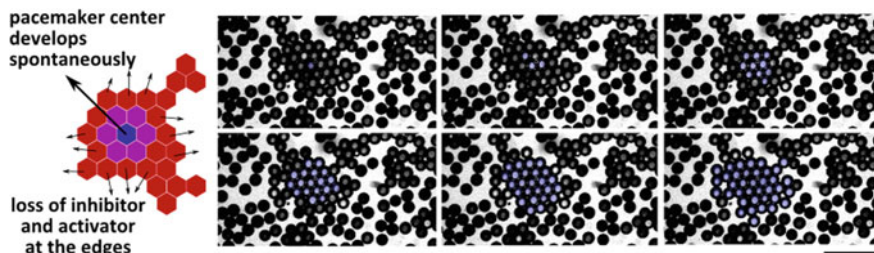
Fig. 5.9 Formation of a target pattern in a 'island' or 'peninsula' type of droplet network. *Left* A schematic of a hexagonal arrangement of droplets which form an 'island'. At the outer edges of the structure, the excitatory and the inhibitory components are lost to the oil phase (shown by the *arrows*), while in the center, they are concentrated leading to the formation of pacemaker center. *Right* A target pattern develops within a 'peninsula' of droplet oscillators. The excitation and wave pattern are shown in *blue* for easy visualization. The scale bar is 500 μ

a similar structure and is connected by a narrow bridge of one or two droplets to a neighbouring 'island'. As we discussed before, the inhibitory (bromine) and the excitatory (BrO_2) components of the BZ reaction readily diffuse into the external oil phase, where they are trapped by the surfactant. Therefore, at the edges of the island, the oscillatory droplets lose their inhibitory and excitatory components to the external oil phase. However, at the center of the island, the concentration of the BZ species increases since they come in from all sides. Depending on the relative concentrations of the inbitory and excitatory components, the center droplet can therefore either 'turn off' (i.e. oscillations are inhibited) or trigger an oscillation. For the malonic acid concentration of 500 mM together with the other concentrations as described in the experimental section, we find that an oscillation is triggered in the central droplet as can be seen in the right panel of Fig. 5.9. This trigger from the central droplet then propagates outward as a target wave throughout the 'island'. If it is a 'peninsula' the connecting bridge can couple the wave to the neighbouring 'island' as well. This pattern then repeats periodically.

Next, we sought if we could induce the pacemaker patterns by confining the oscillators droplets with a channel made of PDMS. In such a scenario as shown in Fig. 5.10, the PDMS walls of the channel, in addition to the oil phase act as sinks for the BZ reaction species. Therefore, we expect that along the length of the channel, multiple pacemaker centers form, each triggering target waves. That this is indeed the case, can be seen in the right panel of Fig. 5.10. The triggering of a wave from a core can be see in the image sequence shown. In addition, a wave can be seen coming in from the right of the images, clearly triggered by a pacemaker upstream in the channel. Indeed there were also waves coming in the from the left side, but not are not shown here.

Next, for the same concentrations, we looked at a very large network of hexagonally packed droplet oscillators, such that the edges are too far away from the cores to have a significant impact. This is shown in Fig. 5.11. In such a case, we see the spontaneous emergence of travelling waves across the network. Indeed, it may be
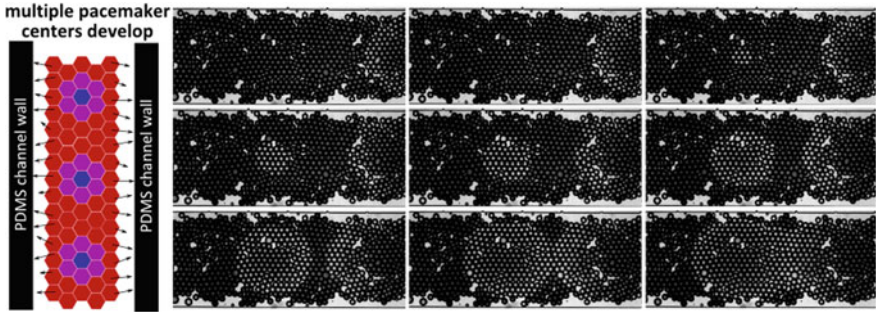
Fig. 5.10 Formation of target waves with multiple pacemaker centers in a oscillator network confined in a PDMS microchannel. *Left* Schematic of the oscillators in a PDMS channel. PDMS, in addition to the oil phase, absorbs the excitatory and inhibitory components of the BZ at the edges (shown by the *arrows*). *Right* Two target wave patterns seen in the channel. One target wave is forming at a pacemaker center clearly visible. The center of target pattern coming in from the right is not visible
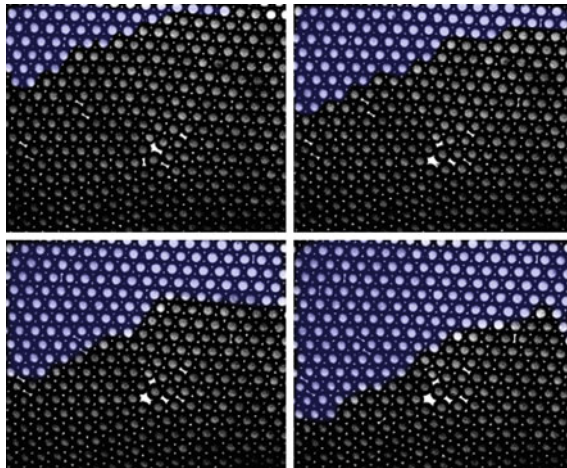
Fig. 5.11 Travelling waves are formed in large densely connected oscillator networks. Each image is spaced 5 s apart. The excitation is *coloured blue* for easy visualization

expected that since the BZ concentrations are rather uniform over the network, a random trigger in one of the oscillators can set off a cascading wave of activity, which repeats periodically. However, we were not able in this scenario to find the precise conditions and locations at which the waves were triggered.

Spiral waves formed in our experiments, when the hexagonal packing was not perfect such that not every oscillator is coupled to six nearest neighbours. Yet, the networks were not so sparse as to form 'islands' or 'peninsulas', where target waves were predominant. An instance of a spiral is seen in Fig. 5.12. A spiral wave can be clearly seen among the oscillator population. A closer look into the network

Fig. 5.12 Formation of spi-
rals in oscillator networks. *Top*
A spiral can be seen clearly in
the oscillator population. *Bot-
tom* Image of the network at
higher magnification reaveal-
ing the lack of perfect local
connectivity for each droplet.
Scale bar is 150 μ
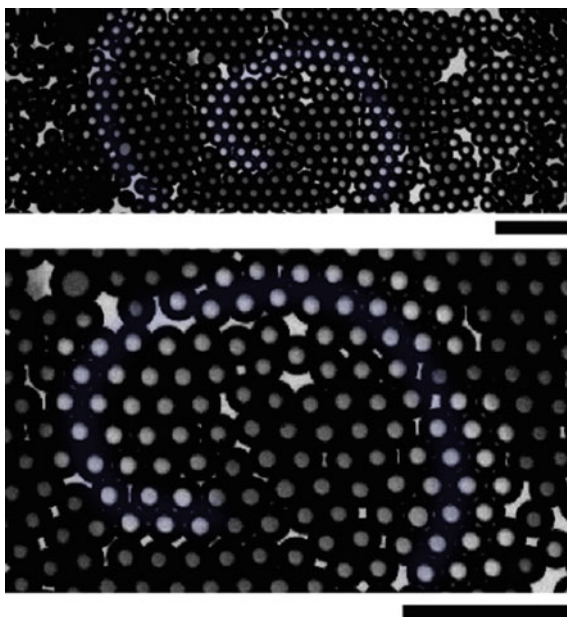
reveals that the local network of each oscillator is not complete according to the
2-dimensional hexagonal packing. The lack of local connections creates a refractory
effect on the excitatory wave due to the different speeds it travels at, in the different
directions. This causes the wave to turn and eventually forms a spiral or other rotary
patterns depending on the exact topology of the network.

Finally, we note that the effect of the bilayer membrane is not just to easily pass
the various species of the BZ reaction from one oscillator to another, such that a dis-
crimination of the 'individual oscillator' is simply lost. In such a case, the behaviour
of the oscillator network can be considered to be the same as that of the BZ reac-
tion in bulk. However, more complex relationships between neighbouring oscillators
connected by a bilayer are seen. As we mentioned before, both the excitatory and
inhibitory components of the BZ reaction can traverse through the bilayer. The for-
mation of the target patterns as described before indicated that the BZ mixture used
in our experiments is excitatory i.e. the excitatory coupling wins over the inhibitory
coupling in determining the state of the coupled oscillators, leading to wave like
patterns as we have seen so far. However, it has been reported in literature [6, 7]
that due to inhibitory coupling between BZ oscillators, it is possible to generate pat-
terns that strongly differ from wave-like patterns. We increased the concentration
of malonic acid to 700 mM compared to the 500 mM used for the previous experi-
ments. It is expected that increasing the concentration of the malonic acid results in a
greater production of the inhibitor, bromine, as shown in the BZ reaction schematic
in Fig. 5.1, thus possibly leading to an inhibitory coupling effect. When the coupling
is inhibitory i.e. non-excitatory, we expect that wave like patterns will not result.
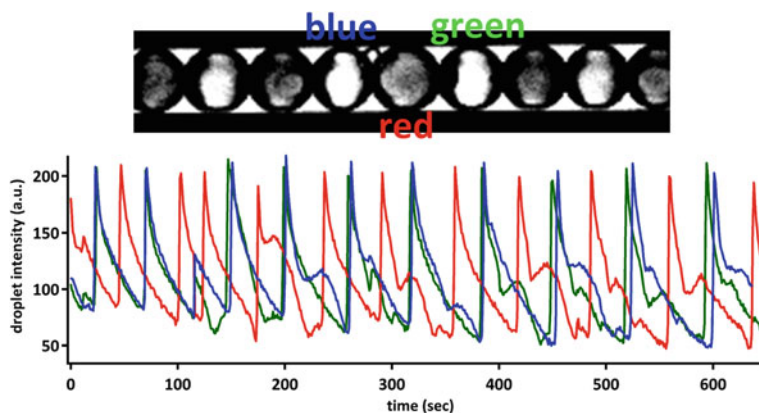
Fig. 5.13 Antiphase pattern in a 1 dimensional oscillator network. *Top* Droplet oscillators in a glass microcapillary. Each droplet pair is connected by bilayer membranes. The droplet diameter is $100\,\mu$. *Bottom* Time trace of the droplet oscillations shown for the three droplets in the center of the top image. The *red*, *blue* and *green* traces correspond to the droplets marked as shown

As anticipated, the increase in the concentration of Malonic acid resulted in a non-wave-like pattern as shown in Fig. 5.13 where every oscillator droplet is found to be in strict anti-phase with its neighbour. This can be understood to be a complicated interplay between the inhibitory and excitatory coupling. In fact it has been shown that the anti-phase state is an attractor for inhibitory coupling [6, 7]. However, in such models of inhibitory coupling, the interdroplet distance is quite large as compared to our experiments where the droplets are separated only by a nanometric membrane. This illustrates that the membrane between the oscillator droplets play an important role in preserving the individual properties of each oscillator. These studies though only demonstrative, must be performed in greater detail in order to quantitate the various synchronization patterns and their relation to the network topology. In particular, a knowledge of the permeability of the membrane to the various coupling intermediates is crucial to have predictive control over the oscillator behaviour.

5.4 Summary and Outlook

Active emulsions, chemical micro-oscillator droplets as presented here, may provide a crucial first step towards the realization of active soft matter which demonstrate complex dynamic functions. The Belousov-Zhabotinsky reaction used here has been studied as a paradigm system for the study of dynamical and pattern forming systems for many years. In the present setting of using it within microfluidic emulsion droplets, qualitatively new phenomena emerge due to the interplay between the droplet network topologies and type of coupling between the oscillators. As we have shown, bilayer membranes play a crucial role in the coupling and synchronization

dynamics. In combination with the results presented in Chap. 2, these open up the possibilities to construct self-organizing dynamic soft matter systems.

Effects such as quorum sensing are widely seen in natural settings and have recently been reported in artificial chemical oscillators [8]. However, there is no deep understanding of such phenomena, particularly due to the difficulty in the resolution of a single, isolated oscillator where very large populations are present, as are typical in such phenomena. Such studies have mainly utilised microbial populations, simply because they are naturally occuring oscillators that are available in sufficient number to carry out such studies. As we have demonstrated here and also as is well known, microfluidic technologies can be used to produce monodisperse droplet samples in great numbers. This can help to study such effects in great detail.

As we discussed in the introduction to this part, active matter, is typically characterised by oscillations and motion of the individual units. As we have discussed in this chapter, the BZ reaction intermediates react with the surfactant in the oil phase and also at the droplet interface. We will show in the subsequent chapters, that this reaction can propel the droplets, creating artificial self propelled droplets.

References

1. I.R. Epstein, J.A. Pojman, *An Introduction to Nonlinear Chemical Dynamics: Oscillations, Waves, Patterns, and Chaos* (Oxford University Press, New York, 1998)
2. A.N. Zaikin, A.M. Zhabotinsky, Concentration wave propagation in two-dimensional liquid-phase self-oscillating system. Nature **225**, 535–537 (1970)
3. A.T. Winfree, Spiral waves of chemical activity. Science **175**, 634–636 (1972)
4. V. Gorodetskii, J. Lauterbach, H.H. Rotermund, J.H. Block, G. Ertl, Coupling between adjacent crystal planes in heterogeneous catalysis by propagating reaction-diffusion waves. Nature **370**, 276–279 (1994)
5. S. Nettesheim, A. von Oertzen, H.H. Rotermund, G. Ertl, Reaction diffusion patterns in the catalytic CO-oxidation on Pt(110): front propagation and spiral waves. J. Chem. Phys. **98**(12), 9977 (1993)
6. M. Toiya, V.K. Vanag, I.R. Epstein, Diffusively coupled chemical oscillators in a microfluidic assembly. Angew. Chem. Int. Ed. Engl. **47**, 7753–7755 (2008)
7. M. Toiya, H.O. González-Ochoa, V.K. Vanag, S. Fraden, I.R. Epstein, Synchronization of chemical micro-oscillators. J. Chem. Phys. Lett. **1**, 1241–1246 (2010)
8. A.F. Taylor, M.R. Tinsley, F. Wang, Z. Huang, K. Showalter, Dynamical quorum sensing and synchronization in large populations of chemical oscillators. Science **323**, 614–617 (2009)

Chapter 6
Swimming Droplets: Artificial Squirmers

Self-propelling droplets which closely mimic the locomotion of some protozoal organisms, so-called squirmers, and their hydrodynamic flow fields are presented.

6.1 Introduction

Self propelled particles (SPPs) typically carry their own energy and are not propelled simply by the thermal buffeting due to the environment. As non-equilibrium entities, they are not restricted to classical equilibrium constraints such as the fluctuation-dissipation theorem and detailed balance. Consequently, SPPs are simple model systems to study the behavior of non-equilibrium phenomena, in particular the mechanics and statistics of active matter.

Studies on SPPs, motivated as it were by the quest for a description of living phenomena, naturally began with the statistical mechanical aspects of biological movement. Due to the relative theoretical and experimental convenience, focus has been mainly on microscale cellular motility over other motion such as that of birds, humans, animals etc. The predominance of viscous forces over inertial forces at the microscopic scales (low Reynolds' numbers) simplifies theoretical treatment due to linearity. However, due to time reversibility in the low Reynolds' number regime, motion mechanisms can be quite complicated and microsopic organisms have developed a variety of strategies to achieve locomotion that allow them to overcome the viscous forces. Flagellated cells such as certain bacteria, sperm, *E. Coli* and trypanosomes use nonreciprocal motions of their flagella to overcome viscous forces and set themselves in motion [1–4]. Organisms such as cyanobacteria, paramecium,
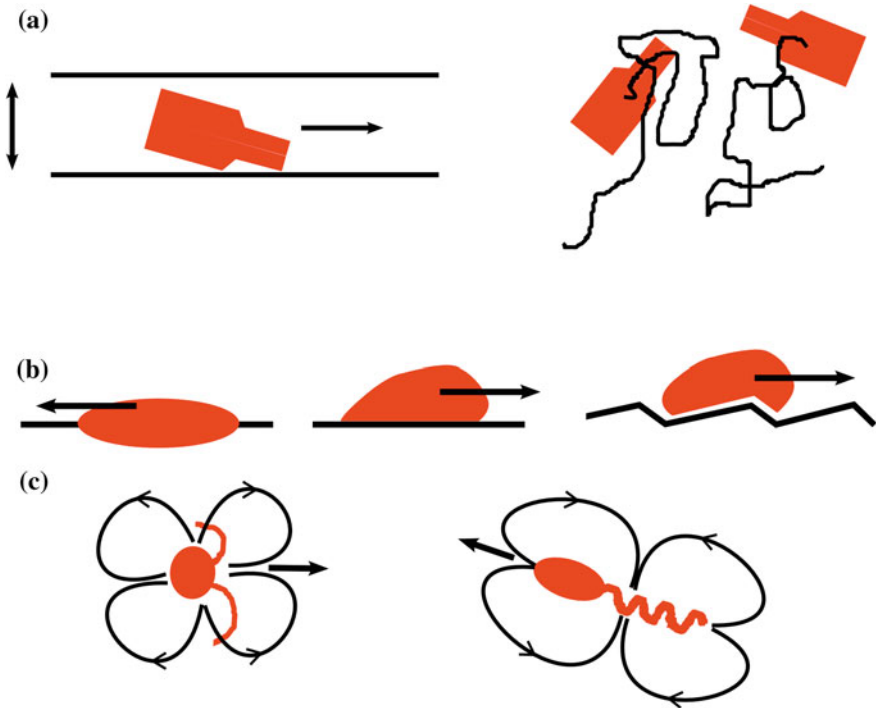
Fig. 6.1 The three classes of SPPs **a** Shaken granular media, is comprised of an asymmetric unit vibrated on (or between two) plates resulting in a quasi two dimensional motion (*black lines* in right image represent object paths) **b** Striders, which move on a surface via modification of the contact properties of the SPP and surface **a** Swimmers, which move in a surrounding fluid, create well defined hydrodynamic flow fields (*black lines*) around them. In all figures, *black arrows* indicate direction of motion

and Volvox belong to a class of swimmers referred to as squirmers and are driven by tangential and/or radial deformations of the cell surface [5–7].

A variety of artificial self propelled particles (SPPs) have also been developed over the years. In the context of the present work, these can be classified as: shaken granular media, striders, and swimmers as depicted in Fig. 6.1. As the name suggests, shaken granular media consists of beads and rods agitated by mechanical shaking. These were among the first to be studied in the context of self propelled objects. Yamada, Hondou, and Sano did pioneering experiments [8] in demonstrating non-Brownian motion of axisymmetric polar objects vibrated between two plates. Asymmetries in the granular unit, either in the form of an asymmetric weight distribution [9] or asymmetric frictional properties [10, 11] lead to a directed motion under agitation.

Striders are such SPPs that move on a surface or at an interface and the motion mechanism relies on the presence of a surface. Self propelled liquid droplets on surfaces have also received considerable attention. The first [12] involves a chemically modified substrate causing variations in the contact angle of a droplet on the surface.

The resulting Marangoni stresses due to the asymmetry of the droplet contact with the substrate propels the droplet forward. Such droplets were also caused to move on a liquid interface due to the differential adsorption of surfactants on the droplet interface [13]. Another kind of strider is a liquid droplet on a hot plate whose surface has a ratcheted step geometry [14]. These are propelled by the flow of air between the droplet and the surface caused by the Leidenfrost effect [15]. Various other such examples of striders such as millimetric camphor and phenanthroline disks on liquid surfaces have also been realised [16–18].

Finally, swimmers are objects that are completely immersed in a fluid and therefore have a hydrodynamic flow field associated with their propulsion. Colloidal janus beads or rods, half covered with platinum, can be propelled by immersing them in H_2O_2 [19]. The platinum catalyzes $H_2O_2 \rightarrow H_2O$, and the resulting osmotic gradients from the asymmetry leads to directed motion. An artificial flagellum in which a red blood cell attached to paramagnetic colloidal beads via DNA linkers can be propelled by an externally applied time varying magnetic field [20]. Finally, modifications of a surfactant at an oil-water interface, of a droplet, either by chemical [21] or photochemical [22] means leads to gradients of interfacial tension around the droplet, thus setting it in motion. All together, a general principle seems to work in the realizations of artificial SPPs i.e. polarity together with a dissipative mechanism leads to motility.

As fas as interactions are concerned, shaken granular media interact by contact and excluded volume interactions alone. Swimmers have a well defined hydrodynamic flow field that emerges due to their motion and can cause longe range interactions mediated by the fluid surrounding them, in addition to excluded volume interactions. Strider interactions can be quite complicated and depend on the surface/ interfacial properties significantly.

The squirming mechanism of swimming is very appealing for elucidating the role of hydrodynamic interactions, since the velocities in the near and far field around such a swimmer can be well described analytically [23, 24]. This makes such swimmers ideally suited for the quantitative study of many open questions regarding the hydrodynamic effects on their interaction with surfaces and with each other, their behavior in external flow, and the origins of coupled and collective behaviour [6, 7].

In this chapter, we present a simple model artificial swimmer that consists of an aqueous droplet moving in an oil 'background' phase. Propulsion arises due to the spontaneous symmetry breaking caused by the reaction of the surfactant at the droplet interface with the contents of the droplet. The reaction at the interface leads to a dynamic instability promoting gradients of interfacial tension around the droplet. As we demonstrate, this results in propulsion of the droplet due to Marangoni stresses. We study the behavior of the self propelled droplets in quasi one and two dimensional environments. Further, we measure the flow fields around such a swimmer and show that they are similar to those due to squirmers.

6.2 Experimental Techniques

Our model squirmer consists of an aqueous droplet moving in an oil 'background' phase. The aqueous phase includes a source of bromine either in the form of dilute (25–50 mM) bromine water or a modified mixture of the Belousov-Zhabotinsky (B-Z) reaction mixture. The non-oscillating B-Z reaction mixture consists of two parts: (i) 50 mM sulphuric acid (H_2SO_4) and 28 mM sodium bromate ($NaBrO_3$) (ii) 400 mM malonic acid ($C_3H_4O_4$) and 2.7 mM ferroin ($C_{36}H_{24}FeN_6O_4S$). For the experiments with the B-Z oscillations, the concentrations are modified as follows: (i) 500 mM sulphuric acid (H_2SO_4) and 280 mM sodium bromate ($NaBrO_3$) (ii) 500 mM malonic acid ($C_3H_4O_4$) and 3 mM ferroin ($C_{36}H_{24}FeN_6O_4S$). The two parts are mixed just prior to droplet formation. Mono-olein (*rac*-Glycerol-1-Mono-oleate, SigmaAldrich) is used as a surfactant, at concentrations (12.5–500 mM), which are much higher than its critical micellar concentration (CMC, <1 mM) in the oil phase, which is squalane (SigmaAldrich). Droplets of the aqueous phase are produced either by hand or using a microfluidic device as shown in Fig. 6.2 and let into a hydrophobised glass capillary or sandwiched between two hydrophobic glass slides separated by a PDMS spacer of $\sim$100 μm thickness. Microfluidic devices are produced using standard soft lithography techniques using PDMS. The glass slides (capillaries) are cleaned using isopropyl alcohol, dried and plasma cleaned for 90 s. A drop of commercially available Nano-Protect is then used to coat the glass surfaces which are then heated in an oven at 65° for 30 min to render them hydrophobic.

Droplet motion is recorded by a CCD camera (PCO 1200) or a high speed camera (Phantom Miro, Vision Research) at frames rates between 0.5 and 1000 Hz. Trajectories are obtained by tracking the droplet positions using MATLAB (MathWorks) and Image-Pro Plus (MediaCybernetics). The flow fields around the squirmer are recorded using the technique of Micro Particle Image Velocimetry (μPIV) [25]. Briefly, the oil phase is seeded with fluorescent tracer beads (200 nm green fluorescent polystyrene beads, Duke Scientific). Fluorescence microscopy is used to record images of the tracer particles and the images are used for PIV analysis using an open source code, PIVlab [26].
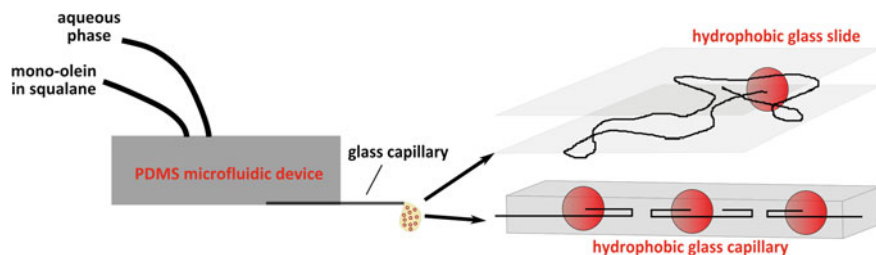

Fig. 6.2 *Left* microfluidic production of squirmer droplets. The droplet production is by a step emulsification droplet production unit. *Right* the squirmers are observed in quasi one and two dimensional environments by confining glass slides or capillaries. The *black lines* represent the tracks of the swimmers

6.3 Results

6.3.1 Marangoni Stresses Propel Droplets

We demonstrate this squirmer scheme with nanoliter droplets containing 25 mM bromine water in a continuous oil phase of squalane containing 50 mM mono-olein (MO). The critical micelle concentration (CMC) is 1.5 mM. The droplets are confined by two hydrophobic glass plates to a quasi 2 dimensional space, thus simplifying droplet tracking. The top panel of Fig. 6.3 shows the trajectory of a single squirmer droplet over a duration of 400 s. The velocity of the droplet in this duration is roughly constant at about 15 µm/sec. The trajectory is reminiscent of a random walk, with a persistence length which is larger than the droplet size and clearly far beyond what would be expected for Brownian motion. A particularly important observation is that the trajectory crosses itself. This is seen even more convincingly in the multiple
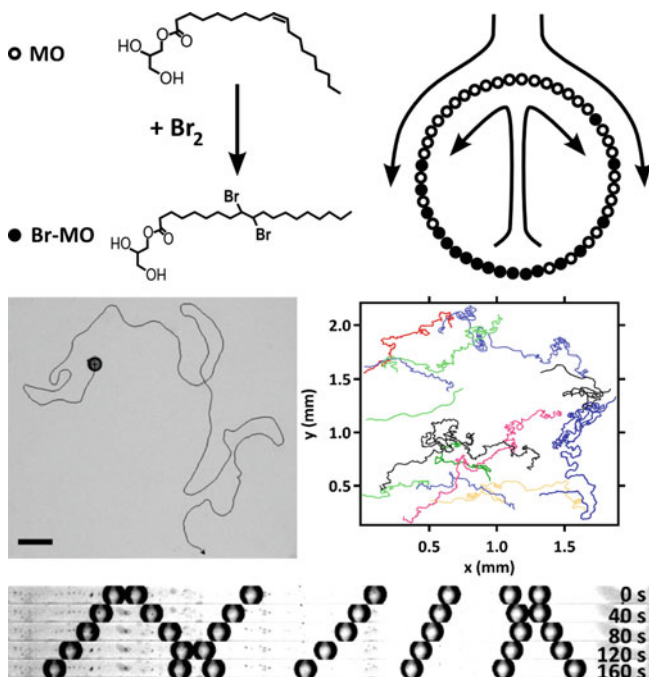
Fig. 6.3 *Top* schematic of a micro-droplet squirmer. Bromination increases the tension of the droplet surface from 1.8 to 3.1 mN/m. The convective flow pattern (shown in the rest frame of the droplet) is accompanied by a gradient in the bromination density. The corresponding Marangoni stress propels the droplet. *Middle*(*left*) path of a single squirmer droplet. The persistence length is clearly large compared to the droplet radius, indicating propelled motion (Scale bar: 300 µ). *Middle*(*right*): Droplet trajectories over an interval of ∼90 s. *Bottom* time lapse series of seven droplets in a microchannel. The droplets change direction without noticeable reduction in velocity

trajectories shown on the right. This is in sharp contrast to other schemes, where the propulsion mechanism itself changes the surrounding medium strongly enough to prevent self-crossing of the path [12]. That this is clearly not the case here is demonstrated in the quasi one-dimensional setup in the bottom panel, which shows a time lapse representation of seven droplets moving in a micro-channel. As two drops touch each other, they reverse their direction of motion and perambulate the channel again, without significant reduction in velocity.

In order to gain some insight into the propulsion mechanism, let us consider a spherical droplet with radius R. The total coverage, c, of the droplet surface with the mono-olein, either brominated or not, is assumed to be roughly constant and in equilibrium with the micellar phase in the oil. The brominated fractional coverage shall be called b. If the droplet moves, there is (in the rest frame of the droplet) an axisymmetric flow field, $u(\theta)$, along its surface. The equation of motion for b is

$$\frac{\partial b}{\partial t} = k(b_0 - b) + \mathrm{div}\,(D_i\,\mathrm{grad}b - ub) \tag{6.1}$$

where b_0 is the equilibrium coverage with brominated mono-olein (brMO). It is determined by the bromine supply from inside the droplet and the rate constant, k, of escape of brMO into the oil phase. D_i is the diffusivity of the surfactant within the interface.

The droplet motion is accompanied by a flow pattern within the droplet and in the neighboring oil, which can be determined from $u(\theta)$ [27, 28]. The corresponding viscous tangential stress exerted on the drop surface must be balanced by the Marangoni stress, $\mathrm{grad}\gamma(\theta) = M\mathrm{grad}b(\theta)$, where γ is the surface tension of the surfactant-laden oil/water interface, and $M = d\gamma/db$ is the Marangoni coefficient of the system. Expanding the bromination density in spherical harmonics,

$$b(\theta) = \sum_{m=0}^{\infty} b_m P_m(\cos\theta) \tag{6.2}$$

we can express the velocity field [27, 28] at the interface as

$$u(\theta) = \frac{M}{\mu \sin\theta} \sum_{m=1}^{\infty} \frac{m(m+1)b_m C_{m+1}^{-1/2}(\cos\theta)}{2m+1} \tag{6.3}$$

where C_n^α denote Gegenbauer polynomials, and μ is the sum of the liquid viscosities outside and inside the droplet. Inserting this into Eq. (6.1) and exploiting the orthogonality relations of Gegenbauer and Legendre polynomials, we obtain

$$\frac{db_m}{dt} = \left[m(m+1)\left(\frac{b_0 M}{(2m+1)R\mu} - \frac{D_i}{R^2} \right) - k \right] b_m \tag{6.4}$$

for all $m > 0$. We see that the different modes decouple, as far as linear stability is concerned. As long as $b_0 M$ is small enough, the resting state is stable against fluctuations. However, when $b_0 M$ exceeds a critical value, the resting state is unstable, and the droplet spontaneously starts to move. It is straightforward to see that for $k < 3D_i/R^2$, this happens first for the lowest mode at $m = 1$ which corresponds to a surface velocity term of the form $u_\theta \sim \kappa \sin\theta$.

6.3.2 Hydrodynamic Flow Fields

As discussed earlier, a swimmer is characterised by its hydrodynamic flow field. Knowledge of this flow field is crucial for understanding swimmer interactions. To elucidate the flow field around the droplet swimmers and for the sake of clarity, we briefly present here the theoretical model and calculations of the flow field for a squirmer.

Typical models of squirmers [24] assume a 'spherical' particle that is driven by a purely tangential velocity (distortion) on its surface. The velocity at a point $\mathbf{r}_s$ on the surface of a sphere of radius a is given by

$$\mathbf{v}_s\left(\mathbf{r}_s, \hat{\mathbf{e}}\right) = \sum_{n=1}^{2} \frac{2}{n(n+1)} B_n \left(\frac{\hat{\mathbf{e}} \cdot \hat{\mathbf{r}}_s}{a} \frac{\mathbf{r}_s}{a} - \hat{\mathbf{e}}\right) P_n'\left(\hat{\mathbf{e}} \cdot \mathbf{r}_s/a\right) \qquad (6.5)$$

where the B_n are constants, $P_n'(x)$ is the derivative of the nth Legendre polynomial, and $\hat{\mathbf{e}}$ is a unit direction vector associated with the sphere. From Eq. 6.5, the polar component of the surface velocity can be written as $u_\theta = B_1 \sin\theta + B_2/2\sin2\theta$, where $\theta = \arccos(\hat{\mathbf{e}} \cdot \mathbf{r}_s/a)$ is the polar angle. The relative strengths of B_1 and B_2 can be tuned to change the characteristic of the surface velocity as shown in Fig. 6.4. For $\beta \equiv B_2/B_1 < 0$, the propulsion acts from the posterior half of the sphere, while for $\beta > 0$, it acts from the anterior. These conditions are qualitatively similar to biological swimmers, so called pushers and pullers respectively. We assign the term neutral squirmer, corresponding to the case of $\beta = 0$.

The flow field $\mathbf{v}$ around the droplet is then calculated by solving the Stokes equation for axisymmetric incompressible flows with $\nabla \cdot \mathbf{v} = 0$ with the boundary conditions $v_\theta(r = a, \theta) = u_\theta$ and $v_r(r = a, \theta) = 0$. As we have seen in the discussion above of the linear stability analysis, we expect a surface velocity of the form $u_\theta \equiv \kappa \sin(\theta)$ corresponding to that of $\beta = 0$ for the droplet swimmers. The solution of the flow field for such boundary conditions, shown in full in the appendix (reproduced from [29]), yields a velocity $\mathbf{v}$ given by

$$v_r(r, \theta) = -\Delta v \left(1 - \frac{a^3}{r^3}\right) \cos(\theta),$$
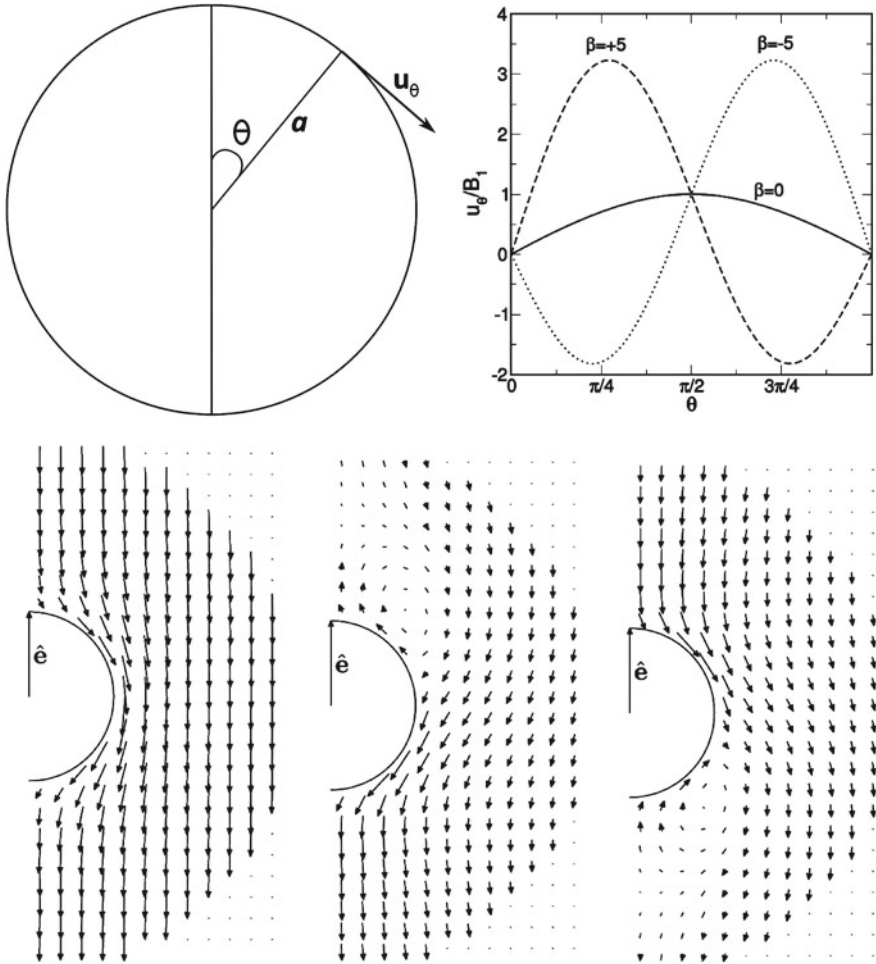
Fig. 6.4 A model squirmer. *Top*(*left*) a schematic of an axisymmetric surface velocity $u_\theta = B_1\sin\theta + B_2/2\sin2\theta$ on a sphere. *Top*(*right*) the surface velocity at different relative strengths of the spherical harmonic modes and (*Bottom*) their corresponding flow fields. $\beta = 0$ corresponds to a neutral squirmer and $\beta < 0$ is a pusher and $\beta > 0$ is a puller

$$v_\theta\,(r, \theta) = -\frac{\Delta v}{2}\left(2 + \frac{a^3}{r^3}\right)\sin\,(\theta) \qquad (6.6)$$

As we can see in Eq. 6.6, the flow field perturbation decays as $\sim 1/r^3$ in three-dimensions and in two-dimensions, it decays as $\sim 1/r^2$ [30]. In order to determine the flow profile around the swimming drop, we performed µPIV using a standard setup (ILA GmbH). The oil phase is seeded with 200 nm green fluorescent polystyrene beads (Duke Scientific) to be used as tracers. The result is shown in Fig. 6.5, and
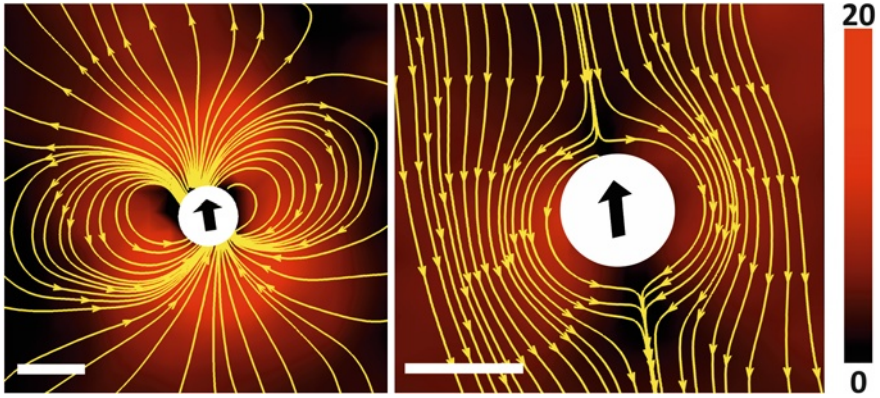
Fig. 6.5 Velocity field around a droplet squirmer. The flow velocity and streamlines in *Left* the reference frame of the laboratory and *Right* the co-moving frame of reference. The magnitude of the flow velocity (*color code*) and streamlines are along a horizontal section through the center of a squirmer droplet. Scale bar: $100\,\mu$; velocity scale (*right*) in microns per second

Fig. 6.6 The fluid velocity calculated at the equator of the swimming droplet. It shows a decay of $\sim 1/r^2$ as the distance from the droplet increases
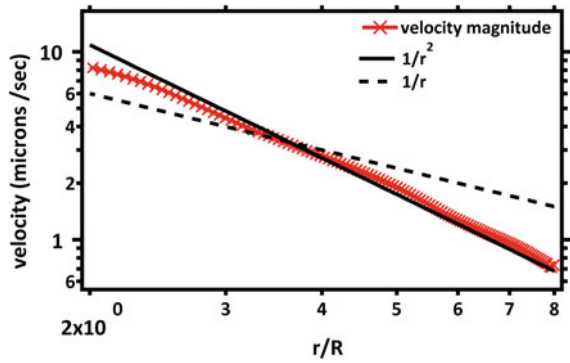
it indeed resembles the flow field around that of a neutral squirmer as shown in the bottom panel of Fig. 6.4. Therefore, we can say here, as discussed in the linear stability analysis, that the surface velocity indeed is set by the destabilisation of the first mode of the spherical harmonics.

From the flow field calculated by μPIV, we extract the velocity field in the oil phase due to the droplet motion along the equator of the droplet. In Fig. 6.6, the velocity magnitude is plotted against the increasing distance from the center of the droplet, where R is the radius of the droplet. It can be seen that the velocity decays as $\sim 1/r^2$ in the far-field. This is to be expected as we have discussed earlier since the droplet is confined to a quasi two-dimensional space in which the measurements are made. However, deviations from the $\sim 1/r^2$ behavior in the near-field, defined by r < 3R, are observed. While these could be due to short lived variations in the surface velocity and spatial inhomogeneties in the channel, further experiments are needed to resolve these.

Therefore we conclude that the droplet swimmers that are propelled by Marangoni stresses, as described earlier, indeed behave as purely neutral squirmers. We note, however, that by careful adjustment of conditions, such as adding suitable solvents to the oil phase, one should be able to tune the exchange rate of the surfactant molecules k (see Sect. 6.3.1), and thus control which modes become unstable. Thereby the flow pattern in the droplet and its vicinity can be adjusted to include the second order term in Eq. 6.5 and thus get a pusher or puller type of squirmer.

6.3.3 Swimmer Velocity

In this section, we present results concerning the velocity of the droplets—first we discuss the speed, followed by a discussion about the directionality.

To discuss the droplet speed, V, we reconsider the total surfactant coverage, c. This adjusts itself as a balance between the molecular adsorption energy at the water/oil interface and the mutual repulsion of the adsorbed surfactant molecules. The equilibrium coverage thus represents a minimum in the interfacial energy. As a consequence, the interfacial tension will not change to first order if c is varied. Deviations of c from its equilibrium value, which come about necessarily for any finite V, will thus be replenished from the surrounding oil phase without noticeable Marangoni stresses.

For a flow profile as shown in Fig. 6.5, we have $\text{div}u(\theta) \propto \cos\theta$. The density of surfactant thus takes the form $\rho \approx \rho_0 + \delta\rho f(r) \cos\theta$, where $\delta\rho \propto V$. $f(r)$ is some function of the radius. If D_m is the diffusivity of the micelles, the diffusion current, $D_m \partial\rho/\partial r$, must balance the depletion rate at the drop interface, $c\text{div}u(\theta) = \frac{3Vc}{2R}\cos\theta$ [24]. As long as this holds, the only source of appreciable Marangoni stresses is the gradient in bromination density, $b(\theta)$. The drop thus keeps taking up speed according to Eq. (6.4). This comes to an end when $\delta\rho \approx \rho_0$. The surfactant layer at the leading end of the drop surface can then not be replenished anymore, and c comes substantially below its equilibrium value. This leads to an increase of surface tension accompanied by a 'backward' Marangoni stress, and thus finally to a saturation of the velocity. According to the reasoning above, we expect that $V \approx 2\rho_0 D_m/3c$.

There is no literature value for the diffusivity of MO micelles in squalane, but we can estimate it on the basis of the Stokes-Einstein relation assuming the radius of the micelles to be similar to the length of a MO molecule (2.3 nm). Using 36 mPa.s for the viscosity of the squalane, we obtain $D_m = 2.6 \times 10^{-12}$ m^2/s. We thus predict $V/\rho_0 \approx 0.27 \frac{\mu\text{m/sec}}{\text{mM/l}}$.

This can be measured experimentally. In order to measure V, we used a reaction mixture within the droplets similar to the Belousov-Zhabotinski (B-Z) reaction, with reactant concentrations adjusted such as to prevent chemical oscillations (with concentrations as described in Sect. 6.2). This results in a spatially and temporally constant bromine release rate in the aqueous phase for an extended period of time. However, since the system is closed, one expects a time dependant swimmer behavior. Indeed, as shown in Fig. 6.8, the speed of the swimmer gradually reduces over time, eventually coming to a halt due to the consumption of fuel. The top panel of
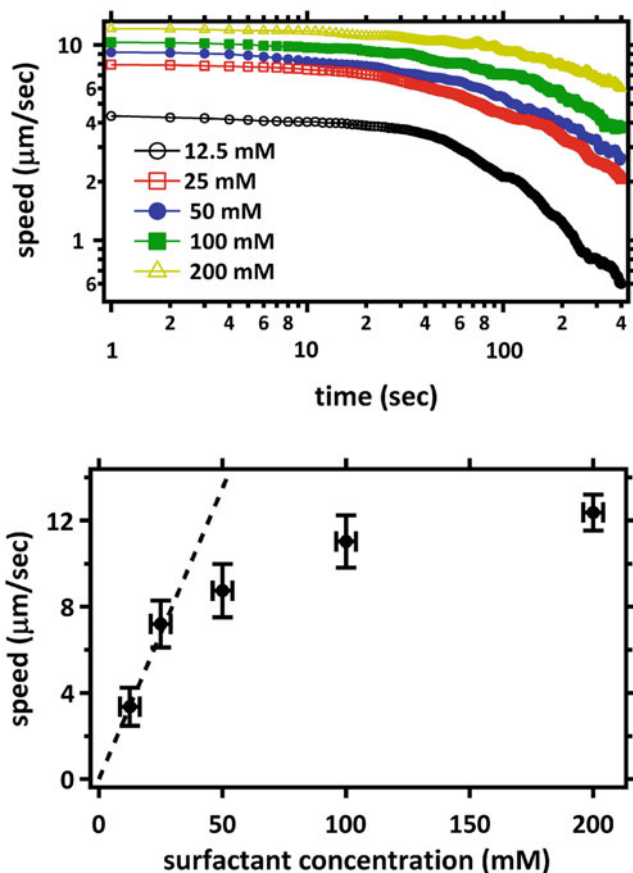
Fig. 6.7 *Top* swimmer speed as a function of time, at different surfactant concentrations, where each curve is an average of ∼50 different squirmer droplets each of diameter ∼80 μ and *Bottom* the initial swimmer speed (average of first 40 time points) as a function of surfactant concentration

Fig. 6.7 shows the droplet speed as a function of time and one indeed sees the decay of the velocity over time. However, to discuss the dependence of the initial droplet speed as a function of the mono-olein concentration in the oil phase, we take an average of the speed over the first 40 time points and this is shown in the bottom panel of Fig. 6.7. The initial linear increase is in agreement with the above prediction (dashed line). As the surfactant density is further increased (and thus the velocity), the complex exchange processes between the water/oil interface and the micelles will finally become the rate limiting step. As a consequence, the speed is expected to level off, in agreement with our data.

As mentioned before, the droplets come to a halt due to the consumption of fuel, either the bromine within the droplet or the surfactant outside the droplet, whichever runs out first. Since the control of bromine within the droplet is tricky due to nonlinear
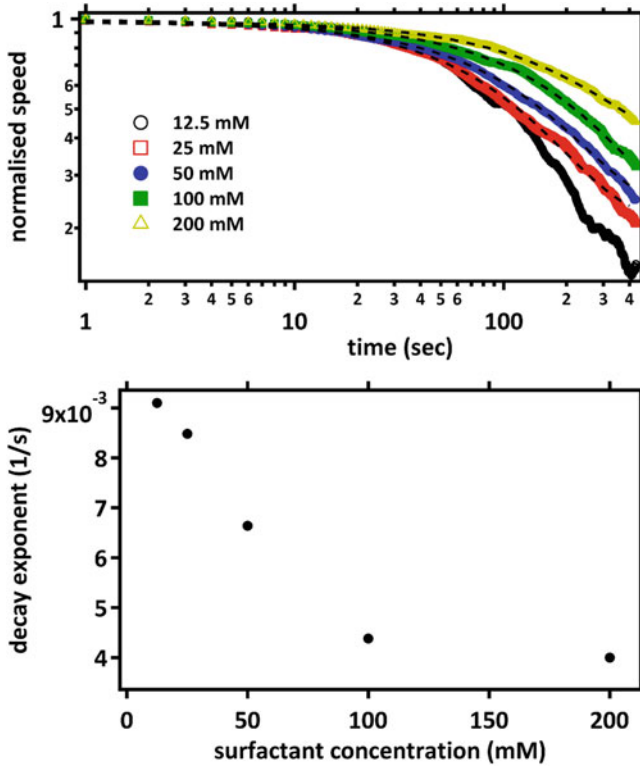
Fig. 6.8 The decay of the swimmer speed with time. *Top* the normalised speed of the squirmers for various surfactant concentration as a function of time. The normalisation is done with the initial (*peak*) speed at each concentration. The decay of the velocity is different for each surfactant concentration. The *black dashed lines* are exponential fits to the data. *Bottom* the decay exponent of the normalised speed as a function of surfactant concentration

dependance of concentrations on the behavior of the B-Z reaction, we again look for the decay at different concentrations of the external fuel i.e. the surfactant. As we increase the surfactant fuel outside the droplet to a concentration much above the concentration of bromine source within the droplets, we expect that the decay rate slows down and eventually tends towards a saturation since the bromine runs out much before the surfactant. That this is indeed the case is shown in Fig. 6.8. In the top panel, we show the speed of the droplet, normalised by the initial speed, as a function of time together with exponential fits to the data shown in black dotted lines. The decay exponent plotted against surfactant concentration indeed shows this saturation behaviour as we just discussed.

The very simple model above predicts the locomotion speed to be independent of the bromine release rate. This can of course not be strictly true in general, and it is instructive to demonstrate this experimentally. We take advantage again of the B-Z reaction, this time creating an oscillating bromine concentration inside the droplet

Fig. 6.9 The speed as a function of time for the squirmers when an oscillating chemical reaction (B-Z) takes place in the droplet. The optical transmission of the droplet is plotted in red (arbitrary units, linear scale) along with the velocity trace
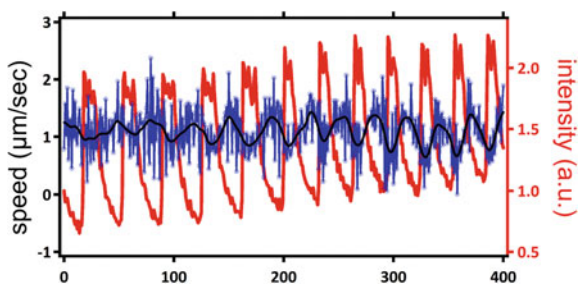
as described in the previous chapter. This oscillation can be easily visualized by the optical transmission of the droplet. Care was taken that there were no spatio-temporal patterns within the droplets, in contrast to some other recent work on droplet locomotion [31]. Figure 6.9 shows an overlay of the the B-Z chemical oscillations and the speed of the swimming droplet, which are anti-phase with each other. As it is known for the B-Z reaction, the decrease of the transmitted intensity corresponds to an increase in the bromine concentration within the droplet. It is obviously possible to control the droplet velocity in some range, and we have demonstrated here how this can be done even in an autonomous manner.

Finally, we come to the discussion of directionality, which together with the speed characterises the squirmer velocity. In Fig. 6.3, we see that some of swimmer tracks are 'smoother' in appearance than others. In other words, some swimmers seem more persistant in their direction than others. However, though the tracks are displayed together, they correspond to swimmers at various times after the initial droplet formation. For a given swimmer, we calculate its directionality, defined as $\langle\cos\phi\rangle$, where ϕ is the turn angle i.e. the angle between the velocity vectors of the swimmer at equidistant time points, as a function of time. As seen in the top panel of Fig. 6.10, which shows the data for surfactant concentration of 100 mM, the directionality increases linearly with time and after $\sim$200 s, it reaches a plateau around $\sim$0.4. As seen in the lower panel of 6.10, this remains roughly constant for a range of surfactant concentrations. Therefore, the change in the directionality of the droplet is likely to be a consequence of the driving from within, namely the bromine source. Initially, when there is a surplus of bromine, the droplets gets 'kicked' around due to the rapidly changing interface conditions. However, as this rate reduces, a balance is reached between the reaction from inside and the replishment of the surfactant from the outside. At this stage, the surface coverage is maintained around an equilibrium value, thus making the motion homogeneous and directionally persistant.

6.4 Summary and Outlook

The Belousov-Zhabotinsky reaction running inside micrometric droplets with mono-olein as a surfactant renders them active: capable of chemical communication as we showed in the previous chapter and also capable of locomotion as described in
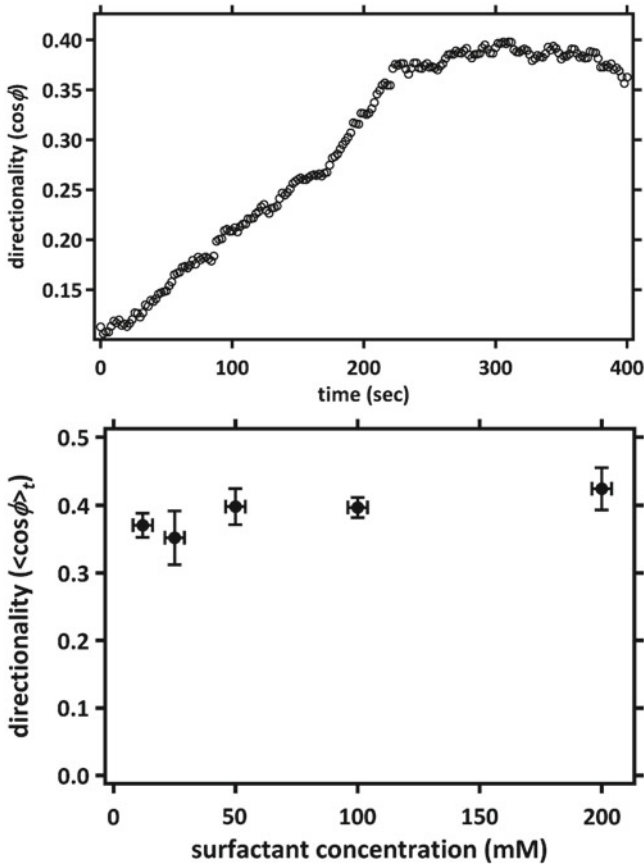
Fig. 6.10 Swimmer directionality. *Top* the time varying directionality is plotted for a surfactant concentration of 100 mM. A linear increase is followed by a saturation of the directionality at $\sim$0.4. *Bottom* the time averaged directionality as a function of surfactant concentration, where each point is an average of $\sim$50 different squirmer droplets each of diameter $\sim$80 μm

this chapter. The locomoting droplets are a novel type of artificial swimmer that mimics the squirming mechanism of propulsion. As we have shown, the droplets are propelled by a Marangoni driven instability that is caused by spontaneous symmetry breaking and sustained through dissipation via a chemical reaction. The chemical reaction has a very weak influence on the environment such that any global chemical coupling of swimmers is not possible. Therefore they are ideally suited to study open questions regarding the physical interactions between SPPs and in particular the role of hydrodynamic interactions on the statistical mechanics of SPP populations.

We have taken the first steps to characterise the swimmer, its velocity and the hydrodynamic flow fields. However, these only open the door to future possibilities— firstly, the flow fields around the squirmers need to be characterised completely,

Fig. 6.11 Scheme for light controlled release of bromine. Silver bromide colloids are included in the aqueous phase which are degenerated by light to release bromine, which participates in the reaction with pristine mono-olein
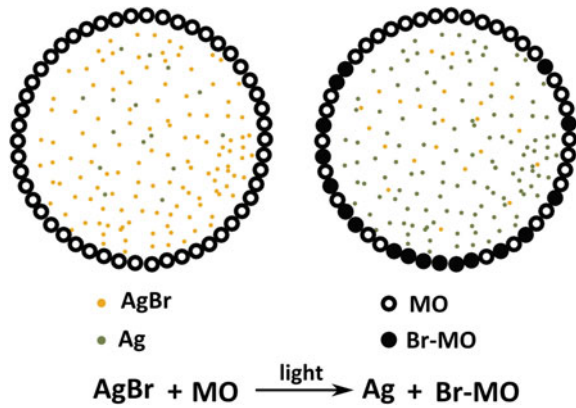
particularly the near fields as we have shown. The chemical tuning to drive the droplets is highly nonlinear, thus making control rather challenging. Further due to this reason, the precise conditions which initiate the motion are not easily accessible. As we also discussed, enhanced control over the motion mechanism can allow us to tune the 'squirmer mode'. Therefore, as a next step, it is planned to replace the B-Z reaction mixture inside the droplets with an aqueous suspension of silver bromide (AgBr) colloids as shown in Fig. 6.11. As the light sensitivity of AgBr is well known from photographic techniques, it might be possible to trigger the controlled release of bromine from within the droplets by light of a suitable wavelength. Therefore, in addition to finding the precise conditions to initiate motion, we might be also able to tune the 'activity' of the droplet squirmers in a light dependant manner. Such control will be very crucial in studying the properties of the droplet squirmers in greater detail.

References

1. H.C. Berg, R.A. Anderson, Bacteria swim by rotating their flagellar filaments. Nature **245**, 380–2 (1973)
2. B.M. Friedrich, I.H. Riedel-Kruse, J. Howard, F. Jülicher, High-precision tracking of sperm swimming fine structure provides strong test of resistive force theory. J. Exp. Biol. **213**, 1226–1234 (2010)
3. D. Bray, *Cell Movements* (Garland, New York, 2000)
4. J.A. Rodríguez, Propulsion of African trypanosomes is driven by bihelical waves with alternating chirality separated by kinks. Proc. Nat. Acad. Sci. USA **106**, 19322–19327 (2009)
5. K.M. Ehlers et al., D. Samuel, H.C. Berg, R. Montgomery, Do cyanobacteria swim using traveling surface waves? Proc. Nat. Acad. Sci. USA **93**, 8340–8343 (1996)
6. T. Ishikawa, M. Hota, Interaction of two swimming Paramecia. J. Exp. Bio. **209**, 4452–4463 (2006)
7. K. Drescher et al., Dancing volvox: hydrodynamic bound states of swimming algae. Phys. Rev. Lett. **102**, 1–4 (2009)

8. D. Yamada, T. Hondou, M. Sano, Coherent dynamics of an asymmetric particle in a vertically vibrating bed. Phys. Rev. E **67**, 040301 (2003)

9. A. Kudrolli, G. Lumay, D. Volfson, L.S. Tsimring, Swarming and swirling in self-propelled polar granular rods. Phys. Rev. Lett. **100**, 058001 (2008)

10. J. Deseigne, O. Dauchot, H. Chaté, Collective motion of vibrated polar disks. Phys. Rev. Lett. **105**(9), 098001 (2010)

11. Z.S. Khan, A. Steinberger, R. Seemann, S. Herminghaus, Wet granular walkers and climbers. New J. Phys. **13**, 053041 (2011)

12. F.D.D. Santos, T. Ondarçuhu, Free-Running droplets. Phys. Rev. Lett. **75**, 2972 (1995)

13. Y. Sumino, N. Magome, T. Hamada, K. Yoshikawa, Self-running droplet: Emergence of regular motion from nonequilibrium noise. Phys. Rev. Lett. **94**, 068301 (2005)

14. H. Linke, B.J. Alemán, L.D. Melling, M.J. Taormina, M.J. Francis, C.C. Dow-Hygelund, V. Narayanan, R.P. Taylor, A. Stout, Self-propelled Leidenfrost droplets. Phys. Rev. Lett. **96**, 154502 (2006)

15. G. Lagubeau, M.L. Merrer, C. Clanet, D. Quere, Leidenfrost on a ratchet. Nat. Phys. **7**, 395–398 (May 2011)

16. N.J. Suematsu, Y. Miyahara, Y. Matsuda, S. Nakata, Self-motion of a benzoquinone disk coupled with a redox reaction. J. Phys. Chem. C **114**(31), 13340–13343 (2010)

17. K. Iida, N.J. Suematsu, Y. Miyahara, H. Kitahata, M. Nagayama, S. Nakata, Experimental and theoretical studies on the self-motion of a phenanthroline disk coupled with complex formation. Phys. Chem. Chem. Phys. **12**(7), 1557 (2010)

18. Y. Hayashima, M. Nagayama, Y. Doi, S. Nakata, M. Kimura, M. Iida, Self-motion of a camphoric acid boat sensitive to the chemical environment. Phys. Chem. Chem. Phys. **4**, 1386–1392 (2002)

19. J.R. Howse, R.A.L. Jones, A.J. Ryan, T. Gough, R. Vafabakhsh, R. Golestanian, Self-motile colloidal particles: From directed propulsion to random walk. Phys. Rev. Lett. **99**, 048102 (2007)

20. R. Dreyfus, J. Baudry, M.L. Roper, M. Fermigier, H.A. Stone, J. Bibette, Microscopic artificial swimmers. Nature **437**, 862–865 (2005)

21. T. Toyota, N. Maru, M.M. Hanczyc, T. Ikegami, T. Sugawara, Self-propelled oil droplets consuming "Fuel" surfactant. J. Am. Chem. Soc. **131**, 5012–5013 (2009)

22. A. Diguet, R. Guillermic, N. Magome, A. Saint-Jalmes, Y. Chen, K. Yoshikawa, D. Baigl, Photomanipulation of a droplet by the chromocapillary effect. Angew. Chem. Int. Ed. **48**, 9281–9284 (2009)

23. J.R. Blake, A spherical envelope approach to ciliary propulsion. J. Fluid Mech. **46**, 199 (1971)

24. M.T. Downton, H. Stark, Simulation of a model microswimmer. J. Phys.: Condens. Matter **21**, 204101 (2009)

25. J.G. Santiago, S.T. Wereley, C.D. Meinhart, D.J. Beebe, R.J. Adrian, A particle image velocimetry system for microfluidics. Exp. Fluids **25**(4), 316–319 (1998)

26. W. Thielicke, E. Stamhuis, PIVlab—time-resolved particle image velocimetry (PIV) tool. http://www.mathworks.com/matlabcentral/fileexchange/27659-pivlab-time-resolved-particle-image-velocimetry-piv-tool

27. M.D. Levan, J. Newman, The effect of surfactant on the terminal and interfacial velocities of a bubble or drop. AIChE J. **22**, 695–701 (1976)

28. M. Levan, Motion of a droplet with a newtonian interface. J. Colloid Interface Sci. **83**, 11–17 (1981)

29. F. Jülicher, J. Prost, Generic theory of colloidal transport. Eur. Phys. J. E **29**, 27–36 (2009)

30. A.T. Chwang, T.Y. Wu, Hydromechanics of low-reynolds-number flow. Part 2. Singularity method for Stokes flows. J. Fluid Mech. **67**, 787 (2006)

31. H. Kitahata, N. Yoshinaga, K.H. Nagai, Y. Sumino, Spontaneous motion of a droplet coupled with a chemical wave. Phys. Rev. E, textbf84, 013101, arXiv:1012.2755v1

Chapter 7
Interacting Droplets: Collective Dynamics

The statistics and dynamics of the interactions of squirmers with each other, with passive tracer particles, with walls and in confinement are investigated.

7.1 Introduction

Interacting self propelled particles (SPPs) have implications in a broad range of systems. Living matter exhibits pattern formation due to interacting self propelled units at various scales, from human crowds, herds, bird flocks, and fish schools [1–3] to bacterial swarms [4], and even down to a molecular level in the dynamics of actin and tubulin filaments [5]. At a theoretical level, several qualitative approaches have been made to incorporate the diverse collective behaviors of such different systems in a common framework [6–8]. Broadly, there have been three categories of theoretical approaches to study and understand the interactions:

1. analysis of the flow induced by an individual or pair of swimmers moving in a viscous liquid [9–12]
2. including nonequilibrium terms in the well studied hydrodynamics of liquid crystals, where active particles are likened to liquid crystals exhibiting orientational order because of their elongated shapes [13–15]
3. derivation of continuum hydrodynamic equations from specific microscopic models (e.g. rule based Vicsek model) of the dynamics [16–18].

Each approach has different merits and disadvantages, with some being too detailed to incorporate more than a few elements at once, and others being too

coarse grained such that microscopic details are ignored. Experimental work has been mainly focussed on using shaken granular media and bacterial populations [4, 19]. The only interactions in granular media are those due to excluded volume interactions and hydrodynamic interactions are fully absent. Experiments with bacterial populations are not only due to the particular importance of understanding the collective behaviour of micro-organisms, but also because these are the only relatively simple active swimmers which can be obtained in sufficient number. Even a bacterium, however, is much more complex than the model elements used so far in theories. Consequently, it is not yet clear which aspects of their collective behaviour are due to physical interactions, and which trace down to more complex biological signalling. The physical interactions are mainly mediated by the medium in which the SPPs are suspended i.e. hydrodynamic interactions or are due to excluded volume interactions. Biochemical interactions include olfactory, visual or chemotactic cues.

Not only flocking behaviour, but also in microbial settings, swimming can significantly affect the distribution of nutrients and chemical signals which are typically thought to only diffuse due to their sizes. The strong flow fields of swimmers can change the distribution of passive media via advection and this is of great significance in understanding population dynamics and evolution. Further, it has been suggested that the hydrodynamic interactions of swimming micro-organisms at interfaces may have biological implications such as in fertizilation and reproduction [20].

In this chapter we investigate the various interactions of the droplet squirmers: (i) with each other, (ii) with passive tracers, (iii) with walls and finally (iv) in one-dimensional confinement.

7.2 Experimental Techniques

The experimental techniques used for the results in this chapter are the same as those described in Chap. 6. They are presented here briefly, for completeness.

All the droplet squirmers here are produced using the non-oscillating B-Z mixture which consists of two parts: (i) 50 mM sulphuric acid (H_2SO_4) and 28 mM sodium bromate ($NaBrO_3$) (ii) 400 mM malonic acid ($C_3H_4O_4$) and 2.7 mM ferroin ($C_{36}H_{24}FeN_6O_4S$). Droplets of this reaction mixture are produced in an external oil phase of squalane containing 200 mM mono-olein by PDMS microfluidic techniques using step emulsification. The two dimensional observation areas are formed either by two hydrophobic glass plates separated by PDMS spacer or are large areas on the same PDMS chip that is used to produce the droplets. Quasi one dimensional experiments are performed in hydrophobised glass capillaries (Hilgenberg GmbH) with square cross sections of inner width of 100 μm and outer width of 135 μm. Image processing and droplet tracking is done using MATLAB, ImageJ and ImagePro-Plus (Media Cybernetics) and the data is analysed using MATLAB.

7.3 Results

### 7.3.1 Hydrodynamic Interactions of Swimmer Populations

It is a long standing debate whether physical effects, like hydrodynamic interactions, are sufficient to explain textures observed in the swarming behaviour of bacteria and other microorganisms, without having to invoke chemotaxis or other genuinely biological effects [6–8, 19]. Using our model squirmers instead of bacteria, we can tackle this problem from the reverse side, asking for the textures we can observe in dense populations of model squirmers, which are guaranteed to exhibit no biological interactions. As we will see, there is indeed considerable structure to unveil even for such simple systems.

We restrict ourselves to effectively two-dimensional systems here, not only for the sake of simplicity, but also because most studies so far have concentrated on the two-dimensional case. Our samples were prepared by creating shallow wells of a few millimeters diameter and a depth just slightly larger than the droplet diameter in poly-dimethyl-siloxane (PDMS) rubber by standard soft lithography techniques. Bonding the PDMS to a glass slide resulted in a compartment, which in addition was connected by a narrow channel to a step emulsification unit, where droplets were produced and subsequently transported through the channel into the sample well. Figure 7.1 shows a typical sample. The red arrows indicate the direction of motion of each droplet. As time proceeds, the formation of rather long-lived clusters of different size is observed. The most striking feature, however, is the significant polar alignment of the velocities of neighboring droplets. In order to quantify this alignment, we use the angular correlation function,

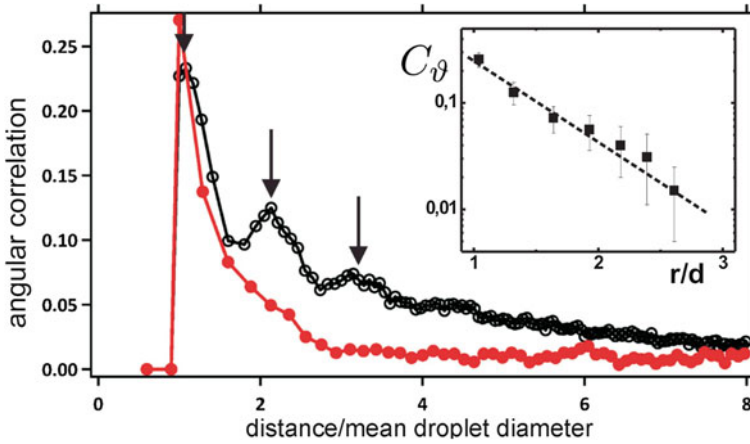$$C_\theta(r) = \langle \delta(r - |r_i - r_j|) \langle \cos\theta \rangle_t \rangle_{ij} \tag{7.1}$$

which describes the propensity of velocities of neighboring particles to align with respect to each other. On the basis of earlier theoretical work, we might under certain circumstances expect a significant polar correlation of the velocities of neighboring

Fig. 7.1 Velocity vectors overlayed on droplets
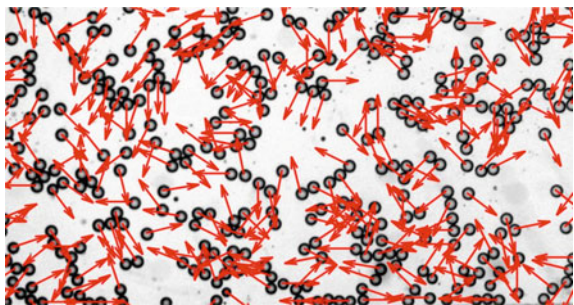
Fig. 7.2 The angular correlation of the droplet motion, C_ϑ, as a function of the scaled distance of the droplet centers, r/d. $d = 2R$ is the droplet diameter. The red curve correspond to an areal droplet density of 0.46, the black curve to a density of 0.78. The black arrows are at multiples of 1.08 droplet diameters. The inset shows a semi-logarithmic plot of the decay of the correlation data. The red line corresponds to a decay length of 0.6 droplet diameters, the straight asymtote of the black line represents a decay length of 2.5 droplet diameters. An oscillation with a period of 1.08 droplet diameters (decaying over 0.9 droplet diameter) has been superimposed to fit the data

droplets [10, 7], just from the hydrodynamic interaction of the squirmers with each other.

That this is indeed the case can be seen in Fig. 7.2. The red curve corresponds to a moderate areal density of 0.46, which we define as the fraction with respect to the density corresponding to a hexagonal close packing. We see that there is significant correlation for small distances. More specifically, the angular correlation function decays approximately exponentially away from the contact distance (which is equal to one droplet diameter, $d = 2R$), as can be seen from the inset. The decay constant is about 0.6 droplet diameters (dashed line in the inset). The angular correlation thus decays almost completely over one interparticle distance, suggesting that the correlation of the velocities is mediated by the pair interaction of the particles. In fact, it has been predicted theoretically that two adjacent droplets which are propelling themselves by means of low order spherical harmonic flow fields may attract themselves into a bound state in which they are swimming with virtually parallel velocities [10]. We provide here a first experimental corroboration of this prediction using a purely 'physical' system. There are, however, also pronounced differences with simulation data. Ishikawa and Pedley [7] have performed simulations of the collective behaviour of spherical droplets with full hydrodynamic interactions, swimming in a monolayer.

This system is very similar to ours, but the monolayer in the simulation was freely suspended in the three-dimensional liquid, such that there was no nearby wall as in our case. This gives rise to long-range hydrodynamic interactions, and provides a

straightforward explanation why they found velocity correlations ranging up to more
than five droplet diameters, in marked contrast to our results.

Correlations become even more pronounced as the density of the droplets is
increased to an areal density of 0.78. As the black curve in Fig. 7.2 shows, we observe
two significant changes. First, the range of the correlation comes significantly larger,
extending clearly beyond four droplet diameters. Second, we observe the appearance
of distinct peaks in the correlation function. The black arrows are at multiples of 1.08
droplet diameters, which is close to what one would expect in case of lateral 'layer-
ing' effects. Also this marked texture, which may be described as ordered rafts, has
not been reported before from simulations of similar systems. An obvious possible
reason is the particularly high areal density in our experiment (it was up to 0.5 in
the study of Ishikawa and Pedley [7]). These results suggest the presence of a phase
transition occurring at a density somewhere between 0.46 and 0.78. Experiments are
under way to search for this transition.

Next, we discuss the effect of the collective behaviour on the effect diffusivities
of the monolayers of swimmers in the two dimensional setting as we just discussed.
We calculate the mean square displacement $\langle x^2 (t - \Delta t) \rangle$ to quantify the motion of
the swimmers. We note here that since the velocity of the droplet is time dependant
as we discussed in Chap. 6 i.e. $v = v(t)$ where v is the velocity of the droplets. In
particular we note that the velocity of the droplet swimmers decreases gradually over
time. Therefore, in order to calculate the mean squared displacement, we introduced
a rescaled time variable τ which is related to the velocity $v(t)$ as

$$\tau = \int_0^t v(t)dt \qquad (7.2)$$

such that in the frame of the rescaled time, the velocity $v(\tau)$ of the droplets will
remain constant at all times. The thus calculated ensemble averaged MSD for exper-
iments with populations of swimmers at three different areal densities, ϕ, are plotted
in Fig. 7.3. From the MSD plots, it can be seen that the motion of the swimmers tran-
sitions from being ballistic (MSD $\sim t^2$) at the short time scales to being diffusive
(MSD $\sim t$) at long times. The crossover to the diffusive regime clearly happens at
different times for the different concentrations. As the concentration of the swimmers
increases, the crossover shifts to shorter times. At low concentration, the crossover is
much later because the swimmers travel in directionally persistant paths before the
weak hydrodynamic fluctuations can significantly alter their trajectories. As as result,
at the lower concentration the transport is ballistic at short times, and at longer times
a crossover to diffusive behavior occurs. However, as the concentration is increased
the diffusivity of the swimmers decreases, as their naturally ballistic trajectories are
increasingly perturbed by hydrodynamic interactions with other swimmers.

For the diffusive regime, an effective diffusivity can be calculated using a linear
fit to the data at the long times ($\Delta \tau > 80$) and this is plotted as a function of the areal
density in the right panel of Fig. 7.4. As we expect from the argument above and
also evident from the MSD traces in Fig. 7.3, the effective diffusivity of the swimmer
populations reduces with increasing swimmer density. However, we see a levelling
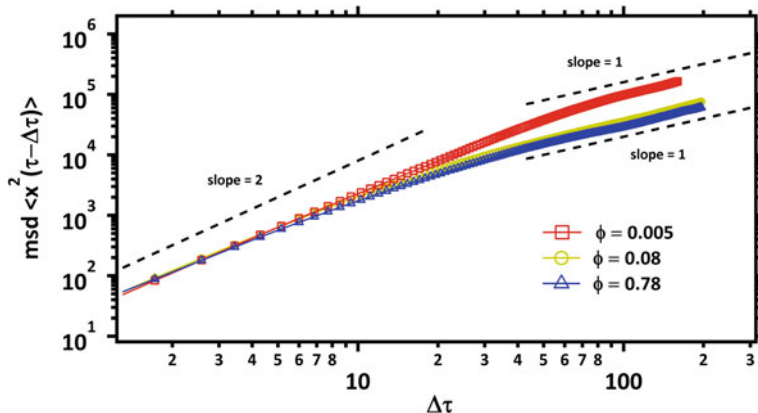
Fig. 7.3 The ensemble averaged mean square displacement (MSD) for a 2- dimensional monolayer of squirmer population at different area fractions. Each population has between 50 and 500 squirmer droplets
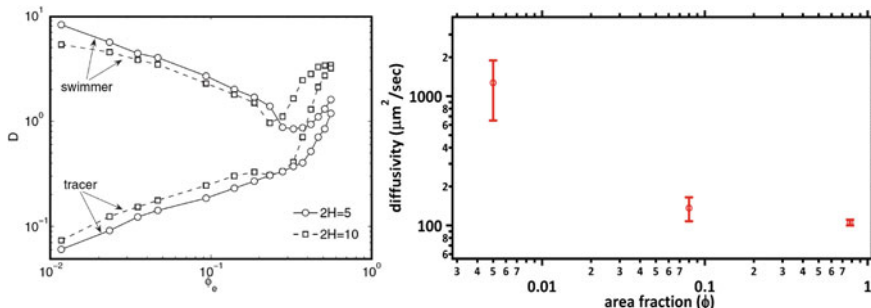
Fig. 7.4 Diffusivity as a function of area fraction. *L*eft Results from a simulation done by Hernandez et al. [6] *R*ight Diffusivities calculated from the long time statistics of the MSD plots shown in Fig. 7.3

off of the diffusivity at increased swimmer densities. In fact, the same behaviour has been seen recently in simulations by Hernandez et. al [6] where they see a reduction in the diffusivity with until a threshold of $\phi \sim 0.3$ at which swimmer density they see an increase in the effective diffusivity. They attribute this to the collective swimming that results due to the hydrodynamic interactions at higher swimmer densities. Indeed, as we have discussed above, hydrodynamic interactions lead to collective swimming states in the droplet swimmers, thus explaining the levelling off of the diffusivities at higher swimmer densities. In the simulations however, the effective diffusivity increases sharply after the threshold of $\phi \sim 0.3$, which is not seen in the experiments. This is not surprising since the simulations were done without monolayer confinement of the swimmers as we have in the experiments. As a result of the monolayer confinement, the long range hydrodynamic interactions may be screened, thus having a reducing effect on the large scale flows of the swimmers,

even though slight collective effects already lead to an enhancement of the effective diffusivity. Further, the walls in the simulations are present much farther away (10 times the swimmers size) than in the experiments, where they might slow down the droplets due to friction. However, it would be very interesting to look for any threshold areal density in the experiments similar to what was seen in the simulations.

7.3.2 Swimmer-Tracer Scattering

The hydrodynamic flow fields not only have consequences for the interaction between swimmers, but also for the distributions of passive particles (tracers) suspended in the medium. The passive particles are in a way 'scattered' by the swimmers involving an interplay of diffusion and advection due to the flow fields of the swimmers. An under-standing of the swimmer-tracer interactions is important to understand processes such as nutrient distribution and uptake in biological settings. Previous studies have demonstrated the enhanced diffusion of Brownian tracer particles in the presence of a dense suspension of swimming bacteria [21, 22]. In fact, in the simulations shown in Fig. 7.4, it can be seen that the diffusivity of the passive tracers is enhanced with the increasing swimming activity. Further, it has been shown experimentally that the statistics of these passive tracers in suspensions of flagellated eukaryotic cells exhibits a non-Gaussian form. In this section, we present the dynamics of the tracer particles around squirming droplets. Rather than the statistical aspects, we focus here on only on the geometry of the tracer trajectories.

The tracer particles that we use for the experiments are 200 nm polystyrene beads that are coated with a fluorescent dye. Therefore, their dynamics in fluid in the absence of any flow is expected to be purely Brownian. However, in the presence of a flow, as caused by the droplet squirmer, in addition to the diffusion, their motion also depends on the flow field set up by the swimmer and the path of the swimmer itself. For the droplet squirmer, the paths of the tracers (black lines) in the rest frame of the droplet are shown in the left panel of Fig. 7.5. Clearly, the tracer tracks follow the flow around the swimmer and reveal, in effect, the flow field of the swimmer which is similar to what we discussed in the previous chapter. However, when the tracers are observed in the reference frame of the laboratory, their paths reveal loopy structures as shown in the right panel of Fig. 7.5. Particularly interesting are the paths of the tracers closest to the squirmer path, which form closed loops. From a flow field similar to that shown in the left panel, it is not obvious at first glance that the tracers should form these closed loop structures.

In order to understand the tracer paths, we look closely into dynamics of a single tracer in the path of the squirmer, which forms a closed loop as shown in the top panel of Fig. 7.6. Snapshots of the swimmer position and the trajectory of a single tracer, in red, show that a loop gets closed as the swimmer passes the tracer. Beyond a distance of ~150 μm, the tracer dynamics are Brownian. As the swimmer approaches closer, the tracer follows the flow field and correspondingly its velocity increases. The
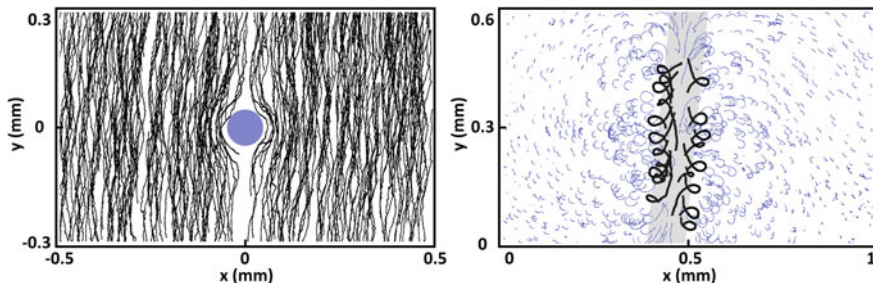
Fig. 7.5 Trajectories of tracer particles around a single droplet squirmer over a 16 s duration *Left* in the co-moving reference frame of the squirmer (shown as *blue circle*, which represents the approximate size of the actual droplet) and *Right* in the laboratory frame of reference. The *grey box* indicates the approximate path of the squirmer. The closed loops of the tracer tracks (*black*) are seen close to the swimmer path
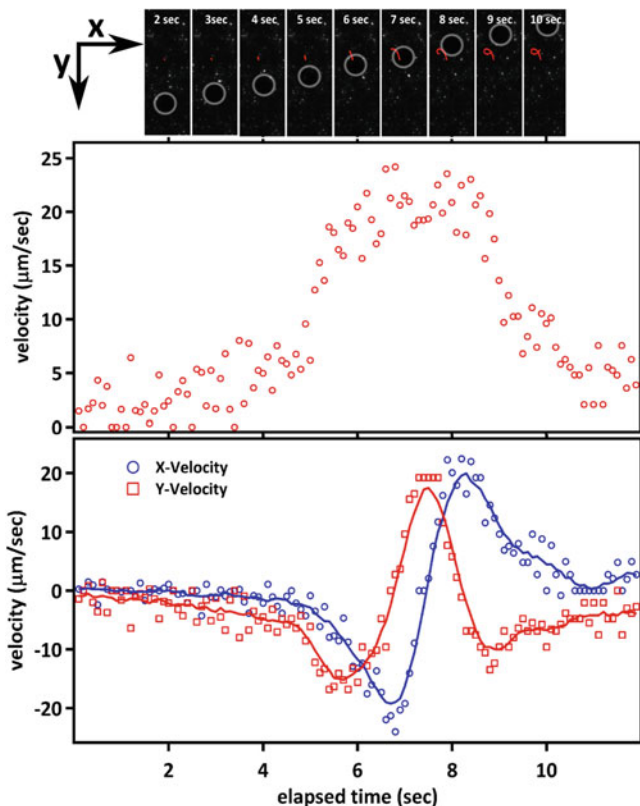
Fig. 7.6 Dynamics of closed loop formation. *Top* Snapshots from an experiment showing the motion of the squirmer droplet (*white circle*) with fluorescent tracers (*white spots*) around. The trajectory of a single tracer which forms a closed loop is shown in *red*. *Middle* The corresponding velocity of tracer as a function of time. *Bottom* The X and Y components of the tracer velocity

velocity of the tracer particle shows two clear peaks, but the details of the formation of the loop lie in the component velocities in the X and the Y directions respectively.

The velocity components in the X and Y directions are shown in the bottom panel of Fig. 7.6. It can be clearly seen from the X-component of the tracer velocity (which in this case is the directional lateral to the swimmer direction) that there are two peaks in the velocity, each corresponding to the movement of the tracer away from and then towards the swimmer, respectively. Similarly, the peak seen in the velocity of the tracer in Y-direction (which is the direction of the swimmer) corresponds to when the tracer reaches the mid-point along the swimmer body, where it moves exactly opposite to the swimmer, whereas the valleys correspond to the front and the back of the swimmer. It is easy to see that for a tracer that goes around the surface of a sphere these are the direct consequence of a tangential velocity on a sphere of the form $u_\theta \sim \kappa \sin\theta$. As we discussed in the previous chapter, this is the flow that is to be expected at the droplet surface due to the Marangoni stresses that propel it. It must be noted that the tracer velocity in the rest frame of the swimmer will also have the same form except that they will be shifted by an amount corresponding to the swimmer velocity.

As the distance from the squirmer increases, we still see loopy tracer paths, but they are not closed (Fig. 7.5)—however, this is simply because of the finite time effect. Asymptotically, all tracer paths must close upon themselves. In fact, it was recently shown analytically by Dunkel et al. [23] that for self-motile force free swimmers, asymptotically, tracer paths converge to a closed loop. While loopy patterns were seen previously in experiments with eukaryotic swimmers [21], the formation of closed trajectories was not resolved. The results presented in this section demonstrate experimentally, for the first time, the dynamics of closed loop formation. Further, it can be seen from the X and Y velocities of the tracer particles that the details of the shape and orientations of the tracer loops are a signature of the flow field due to the swimmer and could throw more light on the flow field of the droplet squirmers, complementing the PIV measurments presented in the previous chapter. These investigations are currently ongoing.

Walls, as opposed to fellow squirmers or passive tracers, are fixed entities. Therefore, squimer-wall interactions are of a different kind as we will see in the section to follow.

7.3.3 Swimmers at Walls

It has been observed and studied in many experiments that microscopic swimmers are attracted to surfaces (walls) [24]. Bacteria and sperm, both flagellated swimmers are known to aggregate at surfaces where they perform circular motions which can lead to large scale organization [24, 25]. By invoking the method of images,[1] it has

---

[1] The method of images is is a mathematical tool for solving differential equations in which the domain of the sought function is extended by the addition of its mirror image with respect to
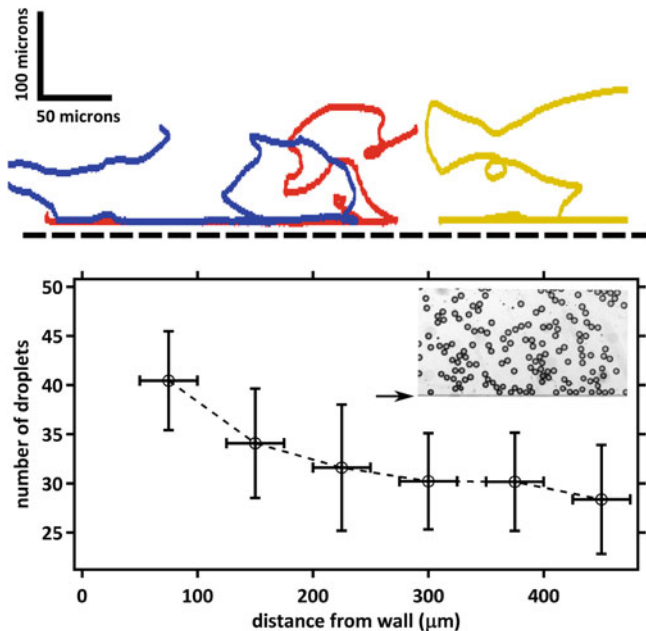
Fig. 7.7 Droplet squirmers have attractive interactions with walls. *Top* Representative squirmer paths (for 3 different squirmers) near a wall (*black dashed line*). *Bottom* The number of droplets as a function of the distance from the wall for an experiment as shown in the *inset*. The average droplet diameter is 50 microns and the *black arrow* points to the wall in the image. Each point on the curve is an average over 1500 time points

been shown that hydrodynamic interactions can explain the attractive interactions of the so called dipolar swimmers with walls [24].

The droplet squirmers are also observed to aggregate at walls. In this section, we do not seek to clarify the hydrodynamics of these interactions. Instead we utilize this behavior, in combination with the fact that the droplet squirmer is simply a non-equilibrium entity, to demonstrate passive rectification. In the top panel of Fig. 7.7, the tracks of three droplets squirmers near a wall (dashed line) are shown. It is readily seen that the droplets tend to travel along the wall for extended lengths, which are much larger than the typical persistence lengths in regions away from walls. The bottom panel of Fig. 7.7 shows the number of droplets plotted as a function of the distance from a side wall for the image shown in the inset. The mean droplet size in the experiment is 50 μm. The vertical error bars represent the statistics on 1500 different time frames of the experiment. The horizontal error bars are one droplet diameter across. This comes from the counting algorithm in which we segment the image into strips of 75 μm width to count the droplets and a half droplet is not

---

a symmetry hyperplane, with the purpose of facilitating the solution of the original problem. In electrostatics, for example, it can be used to calculate the electric field of a charge in the vicinity of a conducting surface.

Fig. 7.8 Squirmers at angu-
lar walls. *Left* Squirmers are
observed in a 2 dimensional
space with a V-shape wall
made from PDMS in the mid-
dle. *Right* An overlay of 600
images shows an aggregation
near the wall, in particular as a
monolayer. The contrast of the
image has been enhanced for
improve visualisation. *Scale
bar* 100 microns
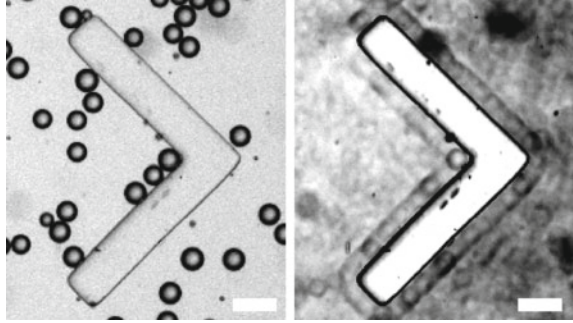
counted. We therefore find that the droplet squirmer number profile peaks strongly
at the wall, indicative of the attractive interactions with walls. Together with the
previous observation, we conclude that the droplet squirmers aggregate near walls
and swim along them for extended times.

Next, we replace straight walls with angular walls in the middle of a channel
as shown in the left panel of Fig. 7.8 to see if droplets tend to accumulate more
along concave walls than convex ones. The chevron shaped structure has angles of
90° at all edges. The attraction of the swimmers to these walls can be seen in the
right panel of Fig. 7.8. This image is constructed by overlaying 600 images (each 1
second apart) of the swimming droplets as the one shown in the left panel. While the
moving droplets appear as a dark smear on the image, it can be seen that along all
the walls, the imprints of a monolayer of droplets can be clearly seen, indicating that
they spend a significant amount of time swimming along the walls. Particularly, at
the concave corners, the swimmers are trapped for a very long time. As we will see
below, the trapping due to the asymmetric V shaped geometry, combined with the
swimmer property of travelling along the walls, can be used to rectify the motion of
a population of the swimmers.

In a set of very elegant experiments, Galajda and colleagues [26] constructed a
bacterial rectifier using a chamber that was divided into two halves by V-shaped walls
as shown in Fig. 7.9. When a bacterial population was initially uniformly distributed
in the chamber, the bacteria were found to be concentrated in one of the halves
(right) with the passage of time, as shown in the fluorescence image. This effect
was attributed to the fact that bacteria were self propelled swimmers that can travel
ballistically along walls and a purely physical mechanism was proposed to explain
the phenomenon, not involving any biochemical mechanisms such as chemotaxis. It
was proposed that for a geometry of walls separating two halves of a chamber, as
shown in the bottom panel of Fig. 7.9, bacteria swimming towards the walls from the
left (numbered 1 and 2) tend to swim along the walls thus leading them into the other
side of the chamber through the gap between walls. However, when they come in
from the right (numbered 3 and 4), due to the shape of the walls, the bacteria which
swim along the walls will be guided back into the same side of the chamber. Thus,
on average more bacteria travel from left to the right than the other way, leading
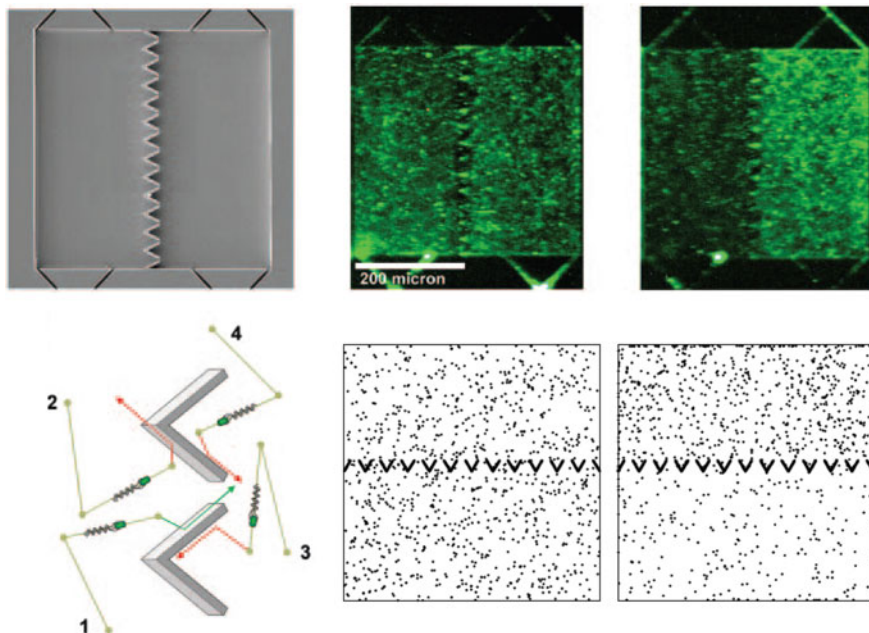
Fig. 7.9 Bacterial rectification using asymmetric walls [26]. *Top* A microfabricated chamber with inlet and outlet ports at *top* and *bottom*. A row of *V-shaped* walls divides the chamber into two halves. A fluorescence image of bacteria in the chamber where there is a uniform distribution at the start of the experiment (*left*) and the steady state after 80 min (*right*). *Bottom* (*left*) Schematic drawing of the interaction of bacteria with the walls. Bacteria on the *left side* may (trace 1) or may not (trace 2) get through the gap, depending on the angle of attack. On the *right*, all bacteria colliding with the wall are diverted away from the gap. *Bottom* (right) Snapshots from a simulation [27], mimicking the above experiment, with point particles that move ballistically along walls

to a concentration on the right side of the chamber. Recent simulations [27] with ballistic point swimmers in the presence of the asymmetric walls, revealed a similar rectification effect. Therefore, the key ingredients for the rectification seem to be ballistic motion along the walls and an asymmetry of the walls to guide the motion, both readily available in our system.

We created a 2-dimensional chamber similar to the one shown in Fig. 7.9 with V-shaped barriers separating the chamber into to equal halves. We guide droplet squirmers into this chamber with an equal distribution on both sides of the barriers and observe their dynamics. As seen in the top panel of Fig. 7.10, which is an overlay of 20 images, each 1 second apart, the walls have a guiding effect on the droplets just as that described above for the case of the bacteria. While the droplets from the bottom half are guided through the gaps, the walls reflect the droplets hitting them from the top. Indeed, the swimmers move ballistically along the channel walls, resulting eventually in an average movement of a population of swimmers from the bottom half of the chamber to the top. Since the droplet size is smaller than the side
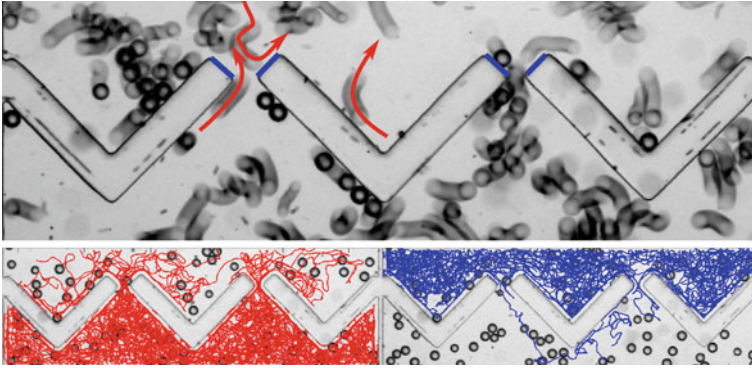
Fig. 7.10 Rectification of droplet squirmers by spatial asymmetry. A 2-dimensional chamber is separated by *V-shaped* walls with gaps of 75 microns between them. The mean droplet size is 50 microns. *Top* A time lapse image showing typical squirmer interactions with walls. Droplet in the *bottom* half of the chamber are guided through the gaps, while those that start at the *top* bounce back from the walls, leading to an effective rectification. *Bottom* Squirmer trajectories over a duration of 10 min are overlayed on the image. *Red* trajectories are for those droplets which were in the *bottom* half of the chamber at the start of the experiment. Similarly blue trajectories represent droplet that started in the *top* half. The rectification effect can be seen by the number of the *red* trajectories that go through to the other side compared with the *blue* ones

wall (marked in blue in the image) of the V-shaped barrier, it may be expected that a similar guiding effect allows droplets from the top half to reach the bottom. This does indeed happen, as we will see below. However, since the length of this side wall is much smaller compared to the long arm of the V and thus the probability of this event is comparitively lower.

The rectification of the droplet motion can be seen very convincingly in the bottom panel of Fig. 7.10 where the trajectories of the droplets are overlayed on the wall geometry. The trajectories shown in red correspond to those droplets that were in the bottom half of the chamber at the start of the experiment and the blue trajectories are correspondingly those of the droplets that started in the top half. At the start of the experiment, corresponding to the trajectories shown, there were 263 droplets in the bottom half and 253 droplets in the top half of chamber. It can be seen very clearly that while more droplets move from bottom to top, and stay there, very few make the transition from the other side. And among the few that do, a majority of them are guided back to the top half due to the rectifying effect. It was counted from the trajectories that 23 droplets transitioned from the bottom to the top half and remained there at the end of the experiment. 5 droplets transitioned from the top to the bottom out of which 2 travelled back (not counted among the 23 mentioned earlier) and 3 remained in the bottom half at the end of the experiment. While the initial droplet distribution ratio in the top to bottom half of the chamber was 0.96, at the end of the experiment it was 1.1. Therefore, we conclude that there is a rectifying effect resulting in directional motion of the droplet population. Thus, from these experiments we can see that the purely physical mechanism described above is sufficient to create passive

rectification under non-equilibrium conditions. The influences of the length and taper of the walls and the ratio of droplet to gap size are currently under investigation from the data already at hand. Further, it must be noted that due to the limited 'lifetime' of the swimmers in this experiment, due to the consumption of fuel, higher distribution ratios could not be achieved.

The droplet squirmers are not just a simple physical model to study the hydrodynamic effects of collective swimming, but also model SPPs well suited for the study of non-equilibrium phenomena. The rectified motion in this system has similarities to Brownian ratchets where particles undergoing Brownian motion in the presence of an asymmetric potential can exhibit a net drift in the presence of an additional ac drive or flashing potential substrate. Whereas the laws of thermodynamics prohibit extraction of useful work from the Brownian motion of particles in equilibrium, these motions can be 'rectified' under nonequilibrium conditions as demonstrated here. Our system is not a Brownian ratchet in this sense; instead, it can be considered to be a realization of a correlation ratchet. The rectification described above is an example for a ratchet created by a broken spatial symmetry (due to the asymmetric barriers) in combination with a broken temporal symmetry (due to the ballistic motion of the swimmers along walls). In correlation ratchets, an overdamped particle can exhibit dc drift on an asymmetric substrate in the absence of an ac flashing or rocking provided that the fluctuations of the particle motion have certain properties that break detailed balance. In our self propelled droplets, the force due to the Marangoni stresses that drives the droplet motion causes the fluctuations to break detailed balance and thus resulting in the broken temporal symmetry.

It has been suggested that such effects could also be at work in biological lipid membranes where asymmetric ion pores may allow for unidirectional diffusion across the membranes [28]. However, in such settings, the pore size is comparable to the size of the molecule traversing it, such that together with a high molecular concentration additional effects arise due to 'stacking up' of the molecules along the length of the ion pore. In the next section, we study the dynamics of the moving droplets when their motion is confined to a single dimension, which is reminiscent of such a situation.

7.3.4 Swimmers in One-Dimension

We can confine the droplet squirmers to a microchannel, such that their motion is restricted to one dimension as shown in Fig. 7.11. In such a geometry, the droplets cannot pass each other, but whenever they collide, they retrace their paths till they meet with a collision again. Since the initial positions, directions and speeds are random, interesting statistics emerge from such motion. In fact, the diffusion of particles in a single dimension where the mutual passage is forbidden and thus the sequence of particles remains the same over time is known as single file diffusion (SFD) and has been studied for a long time [29, 30]. In the thermodynamic limit (when the density of particles $\rho = N/L$ is constant where N is the number of particles moving on a segment of length L, and $N, L \rightarrow \infty$), it has been shown

Fig. 7.11 A time lapse series of droplets confined to motion in a single dimension in a microchannel. Droplets retrace their paths at each collision, reminiscent of single file diffusion
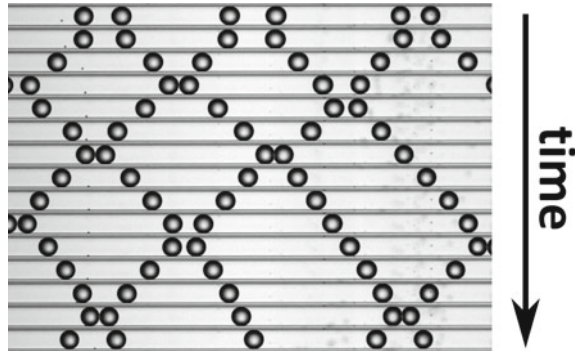
[29] that the expression for the mean squared displacement (MSD) of each particle undergoing SFD can be written as

$$\langle x^2 (t - \Delta t) \rangle = \langle |\Delta x(t)| \rangle / \rho \qquad (7.3)$$

with $\langle |\Delta x(t)| \rangle$ denoting the absolute displacement of a free particle. For ballistic particles, $\langle |\Delta x(t)| \rangle = \langle |v| \rangle t$, where $\langle \cdots \rangle$ is the ensemble average taken over the distribution of initial velocities. Therefore, the MSD for a ballistic single file (bSF) particle can be written as

$$\langle x^2 (t - \Delta t) \rangle = \langle |v| \rangle t / \rho \qquad (7.4)$$

such that a bSF particle diffuses apparently like a Brownian particle with normal diffusion coefficient $D = \langle |v| \rangle / (2\rho)$.

For a stochastic single file (SSF) i.e. a single file of Brownian particles with a damping constant η at temperature T, the equality $\langle |\Delta x(t)| \rangle = \sqrt{4 D_0 t / \pi}$ results in the anomalous diffusion law

$$\langle x^2 (t - \Delta t) \rangle = 2F \sqrt{t} / \rho \qquad (7.5)$$

where F is a mobility factor related to the single particle diffusion constant, $D_0 = \kappa T / \eta$, as $F = \sqrt{D_0 / \pi}$.

The moving droplets in a microchannel are reminiscent of a bSF, such that they move ballistically between collisions. This can be seen in Fig. 7.12 where the velocity of 4 representative droplets in a single file are plotted as a function of time. The changes in droplet direction are marked by droplet collisions, corresponding with the zero crossings of the velocity traces. Between the collisions, the velocity of the droplet stays roughly constant, characteristic of the ballistic regime. From the crossover times, we get an estimate of the most probable collision time between the droplets as shown in Fig. 7.13 and we see that there are peaks in the distribution corresponding to collision times of $\sim$48, $\sim$100 and $\sim$220 s. The various peaks are
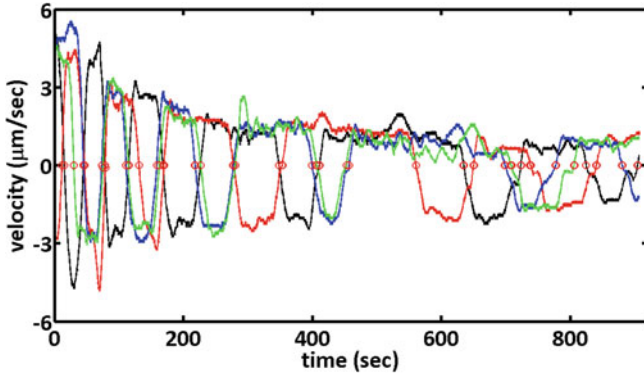
Fig. 7.12 Velocity of droplets in a channel as a function of time, shown for 4 representative droplets. The traces are *coloured* for distinguishability. The *red circles* mark the zero crossings of the velocity traces, indicating droplet collisions

**Fig. 7.13** Probability density of the time between the droplet collisions
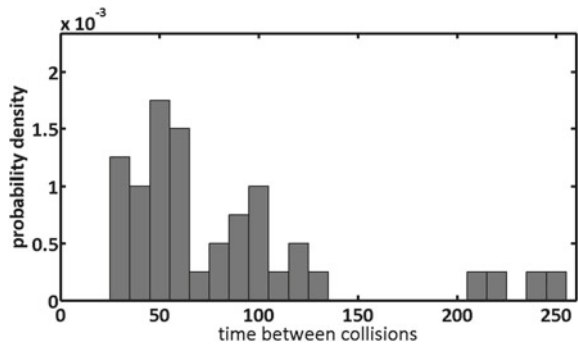
due to the gradually reducing speed of the droplets due to which collision times take longer.

As discussed earlier, in order to account for the gradually decreasing velocity of the droplets, we use a rescaled time variable τ, given by Eq. 7.2. In the frame of the rescaled time, the velocity of the droplets remains constant at all times as seen in Fig. 7.14 with a mean velocity of the droplets of $\langle |v| \rangle \sim 4.17$ μm/s. Further, when we now look at the distribution of the droplet collision times, we get a single peak corresponding to $\tau \sim 65$ s as seen in Fig. 7.15. In this case, we find the mean time of the first collision to be 88.4 s.

Figure 7.16 shows the mean square displacement (MSD) $\langle x^2 (\tau - \Delta \tau) \rangle$, where $\Delta \tau$ is the rescaled time step as defined in Eq. (7.2), plotted against the time step. As expected, at the short times, we see a purely ballistic regime, characterised by a MSD that grows as t^2. It can be seen that at a time of $\sim$80 s, there is a crossover from the ballistic behaviour to a diffusive behaviour, where the MSD grows linearly with time. The velocity autocorrelation for the droplets, is shown in red, and at the short times the velocity is correlated due to the ballistic motion. However at the
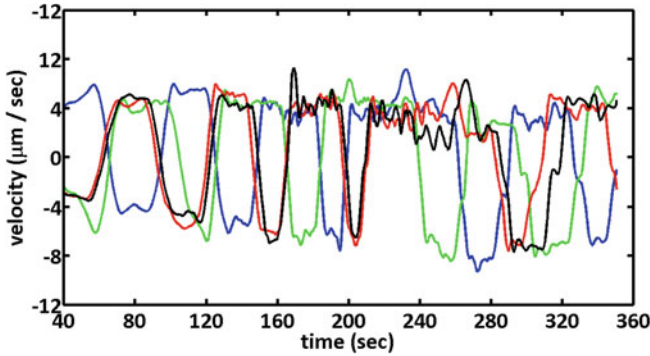
Fig. 7.14 Velocity of droplets in a channel as a function of rescaled time, shown for 4 representative droplets. The traces are *coloured* for distinguishability. In the frame of the rescaled time, the velocity now remains constant over time
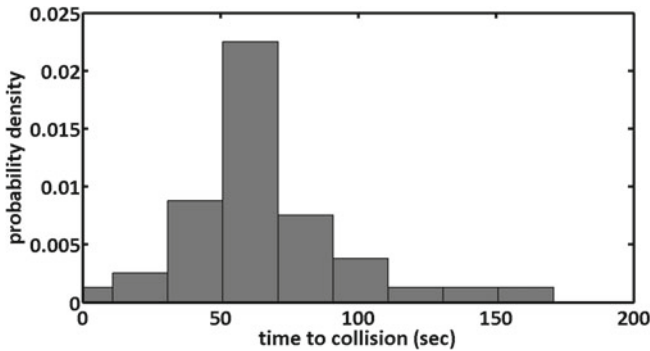
Fig. 7.15 Frequency distribution of the rescaled time between the droplet collisions

crossover to the diffusive regime, we see a corresponding loss of correlation in the velocity of the droplets. This clearly points to a collision time when the direction of motion changes. Indeed, the time of 88 s is the mean time for the first collision as we discussed above. Therefore, it seems that the transition from the ballistic to diffusive regimes is set by the mean time of first collision, as one would expect. Subsequently there are oscillations in the velocity auto-correlation at multiples of the mean first collision time.

We can calculate the diffusivity D at long times by doing a linear fit to the MSD, at long times, as shown by the blue line in Fig. 7.16. The diffusivity in one-dimension is given by the $1/2 \cdot slope\ of\ the\ linear\ fit$ and we get a value for the enhanced diffusivity as $D \sim 1137.7\ \mu m^2/sec$. Using the expression $D = \langle |v| \rangle / (2\rho)$ from the bSF theory, we get $D \sim 1167.8\ \mu m^2/s$ for $\rho \sim 0.0018\ \mu m^{-1}$ (5 droplets per 2.8 mm) and $\langle |v| \rangle \sim 4.17\ \mu m/s$, in good agreement with the diffusivity calculated from the experiments. The value $\langle |v| \rangle \sim 4.17\ \mu m/s$, corresponds to the ensemble
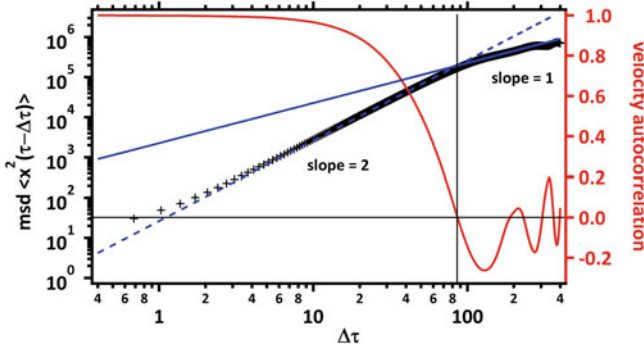
Fig. 7.16 The ensemble average (of 7 droplets) of the mean square displacement as a function of time. The *solid blue line* is a linear fit used to calculate the effective diffusivity of the droplets. The *dotted blue* like has a slope of 2. The *black cross-lines* are a guide to identify the cross-over from the ballistic to diffusive regimes. The *red* trace with the axis on the right is the autocorrelation of the velocity

average of the initial velocity of the droplets when the time variable is rescaled according to 7.2 as discussed above.

However, it must be noted that the present experiments are limited by a finite system size, while the theory is for the thermodynamic limit with $N \to \infty$. More importantly, there are strong hydrodynamic effects which can change the interactions between the swimmers, that are not present in the theory. These could be the reason for the discrepancy between the theoretical and experimental values found above and the statistical inferences drawn might be improved when such effects are taken into account or if the experiments are modified.

Finally, we show that as we change the one-dimensional confinement of the droplets to what may be termed as a quasi 1.5-D confinement, the dynamics of the droplet motion (as measured in one-dimension) become diffusive. This can be seen in Fig. 7.17 where we progressively reduce the droplet size, while still maintaining the condition that neighbouring droplets do not pass each other, such that the motion of the droplets is not strictly one-dimensional. In addition to the reduction of the droplet size, the number density also increases. In such a setting, droplets change direction not only in response to a collision, but also due to changes in swimming direction and therefore their dynamics appears more diffusive. As we can see from the MSD calculated for these experiments, the short time dynamics change from being ballistic for the strictly one-dimensional motion, through enhanced diffusive dynamics, finally to a close to diffusive dynamics when the confinement is significantly reduced. The MSD is calculated only for one dimension in all these experiments. When the short time dynamics tend to be diffusive, as we see for the data in red, we see a crossover to the anomalous diffusive regime as described in Eq. (7.5). Further, since the density increases, the mean time between collisions reduces, thus shifting the crossover to earlier times.
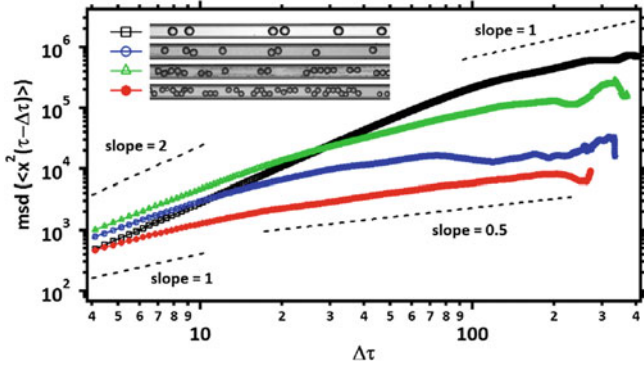
Fig. 7.17 Ensemble averaged MSDs for different confinements of droplets as shown in the *inset* of the legend

In this section, we presented results which demonstrate that the droplet squirmers might be a versatile table top tool to study the statistical mechanics of SPPs in general and not just the hydrodynamics of microswimmers. However, improvements in the experimental techniques such as changing the linear channel geometry to a circular one with more droplets and having an improved chemical drive of the droplets to increase the observation time and thus record many more collisions between the particles will definitely help to improve the statistical inferences.

7.4 Summary and Outlook

We have demonstrated that the artificial squirmer described in Chap. 6 is particulary well suited for the study of collective phenomena of microswimmers. The collective behaviour of these squirmers shows strong velocity correlations and effective diffusivities, which are qualitatively similar to recent simulation results. However, distinct differences were observed which can be attributed in part to simplifications that had to be made in the simulations. The interactions with passive tracer particles were shown to result in closed loops for the tracer trajectories, which can have implications in understanding flow field from tracer properties. Finally, studying their interactions with walls and in confinement, we were able to demonstrate the suitability of the droplet swimmers for studies of a range of non-equilibrium phenomena. While the results presented in this chapter were able to address some open questions concerning the collective dynamics of microswimmer, they open the door to many more possibilities in the future. As we discussed earlier, we would like to look for phase transitions in the swimmer density going from individual to collective dynamics. Such a study will only benefit from the complete characterization of the flow fields of the squirmer, in addition to improving the ability to tune the motion of the swimmer better. While some of the experiments to address these issues are
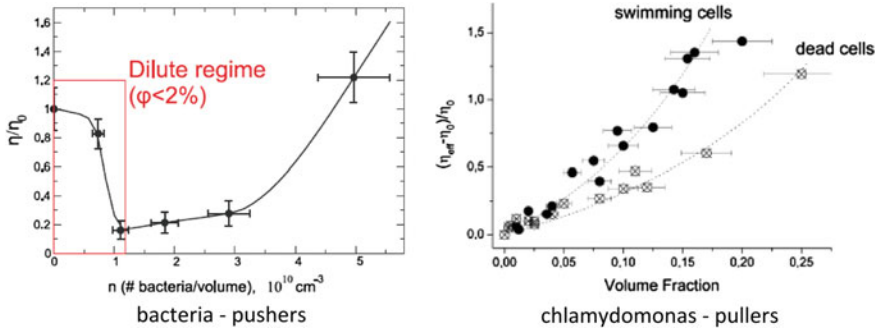
Fig. 7.18 Rheological measurements on *Left* Bacterial suspensions which are pusher type swimmers [31] and *Right* Chlamydomonas suspensions which are puller type swimmers [32]

already underway, we anticipate that many more exciting investigations are possible by simple extensions of the current system.

The rheological properties of suspensions of microswimmers are still very unclear. As shown in Fig. 7.18, recent measurements on bacterial suspensions revealed an effective decrease in the viscosity of the medium with increasing swimmer density in the dilute regime (left panel) [31] while similar experiments with chlamydomonas suspensions revealed an increase at similar densities (right panel) [32]. The bacterium is a pusher type of swimmer, while chlamydomonas pull themselves. However it is not clear how such a distinction might explain the findings or even if this distinction alone is sufficient to account for the different behaviours. The droplet squirmers investigated here might help in addressing some of these issues. Since considerable work has been done on the rheology of emulsions, such principles and experiments could be extended to study the rheology of the active emulsions presented here.

Further, there has been growing interest in the motion of microscale swimmers through complex networks such as that of disease causing pathogens wading through the complex blood stream network [33]. This clearly has implications for disease

Fig. 7.19 Droplet swimmers on 2-D lattice and random network topologies. *White spaces* represent 'channels', *black* regions are walls and the *red circles* indicate swimmers
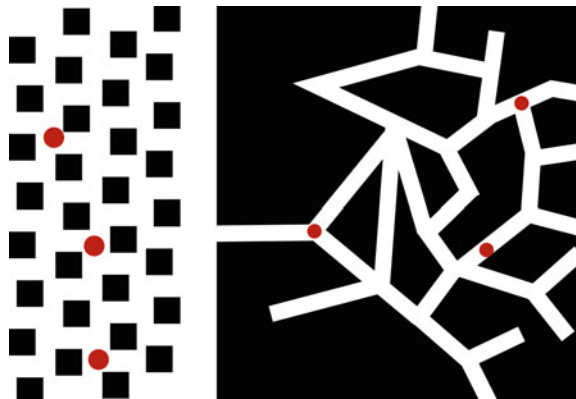
spreading and diagnostics. Other than the obvious biological influences on such motion, it can be imagined that the network topology plays a role in how far a swimmer can traverse through such networks. Such a situation can be mimicked by creating a complex enough, yet quantifiable, network of microfluidic channels through which the droplet squirmers can traverse as shown in Fig. 7.19. As we discussed in this chapter, the complex interplay of the effects of confinement, hydrodynamic interactions and network topology could lead to truly interesting behaviour.

References

1. K. Bhattacharya, T. Vicsek, Collective decision making in cohesive flocks. New J. Phys. **12**, 093019 (2010)
2. V. Guttal, I.D. Couzin, Social interactions, information use, and the evolution of collective migration. Proc. Natl. Acad. Sci. **107**(37), 16172–16177 (2010)
3. P. Romanczuk, I.D. Couzin, L. Schimansky-Geier, Collective motion due to individual escape and pursuit response. Phys. Rev. Lett. **102**, 010602 (2009)
4. H.P. Zhang, A. Be'er, E. Florin, H.L. Swinney, Collective motion and density fluctuations in bacterial colonies. Proc. Natl. Acad. Sci. **107**(31), 13626–13630 (2010)
5. V. Schaller, C. Weber, C. Semmrich, E. Frey, A.R. Bausch, Polar patterns of driven filaments. Nature **467**(7311), 73–77 (2010)
6. J.P. Hernandez-Ortiz, C.G. Stoltz, M.D. Graham, Transport and collective dynamics in suspensions of confined swimming particles. Phys. Rev. Lett. **95**, 204501 (2005)
7. T. Ishikawa, T.J. Pedley, Coherent structures in monolayers of swimming particles. Phys. Rev. Lett. **100**, 088103 (2008)
8. F. Ginelli, F. Peruani, M. Bär, H. Chaté, Large-scale collective properties of self-propelled rods. Phys. Rev. Lett. **104**, 184502 (2010)
9. A. Najafi, R. Golestanian, Simple swimmer at low reynolds number: three linked spheres. Phys. Rev. E **69**, 062901 (2004)
10. T. Ishikawa, M.P. Simmonds, T.J. Pedley, Hydrodynamic interaction of two swimming model micro-organisms. J. Fluid Mech. **568**, 119–160 (2006)
11. E. Lauga, D. Bartolo, No many-scallop theorem: collective locomotion of reciprocal swimmers. Phys. Rev. E **78**(3), 030901 (2008)
12. C.M. Pooley, G.P. Alexander, J.M. Yeomans, Hydrodynamic interaction between two swimmers at low reynolds number. Phys. Rev. Lett. **99**, 228103 (2007)
13. R. A. Simha , S. Ramaswamy, Hydrodynamic fluctuations and instabilities in ordered suspensions of self-propelled particles. Phys. Rev. Lett. **89**, (2002)
14. J. Toner, Y. Tu, Long-Range order in a two-dimensional dynamical XY model: how birds fly together. Phys. Rev. Lett. **75**, 4326 (1995)
15. I.S. Aranson, L.S. Tsimring, Pattern formation of microtubules and motors: inelastic interaction of polar rods. Phys. Rev. E **71**, 050901 (2005)
16. J. Toner, Y. Tu, S. Ramaswamy, Hydrodynamics and phases of flocks. Ann. Phys. **318**, 170–244 (2005)
17. A. Baskaran, M.C. Marchetti, Statistical mechanics and hydrodynamics of bacterial suspensions. Proc. Natl. Acad. Sci. **106**(37), 15567–15572 (2009)
18. T. Vicsek, A. Czirók, E. Ben-Jacob, I. Cohen, O. Shochet, Novel type of phase transition in a system of self-driven particles. Phys. Rev. Lett. **75**(6), 1226 (1995)
19. C. Dombrowski, L. Cisneros, S. Chatkaew, R. E. Goldstein, J. O. Kessler, Self-concentration and large-scale coherence in bacterial dynamics. Phys. Rev. Lett. **93**, (2004)
20. K. Drescher et al., Dancing volvox: hydrodynamic bound states of swimming algae. Phys. Rev. Lett. **102**, 1–4 (2009)

21. K.C. Leptos, J.S. Guasto, J.P. Gollub, A.I. Pesci, R.E. Goldstein, Dynamics of enhanced tracer diffusion in suspensions of swimming eukaryotic microorganisms. Phys. Rev. Lett. **103**, 198103 (2009)
22. X. L. Wu , A. Libchaber, Particle diffusion in a quasi-two-dimensional bacterial bath. Phys. Rev. Lett. **84**, (2000)
23. J. Dunkel, V.B. Putz, I.M. Zaid, J.M. Yeomans, Swimmer-tracer scattering at low Reynolds number. Soft Matter **6**(17), 4268 (2010)
24. A.P. Berke, L. Turner, H.C. Berg, E. Lauga, Hydrodynamic attraction of swimming microorganisms by surfaces. Phys. Rev. Lett. **101**, 038102 (2008)
25. I.H. Riedel, K. Kruse, J. Howard, A self-organized vortex array of hydrodynamically entrained sperm cells. Science **309**, 300–303 (2005)
26. P. Galajda, J. Keymer, P. Chaikin, R. Austin, A wall of funnels concentrates swimming bacteria. J. Bacteriol. **189**, 8704–8707 (2007)
27. M.B. Wan, C.J.O. Reichhardt, Z. Nussinov, C. Reichhardt, Rectification of swimming bacteria and self-driven particle systems by arrays of asymmetric barriers. Phys. Rev. Lett. **101**, 018102 (2008)
28. R.S. Shaw, N. Packard, M. Schröter, H.L. Swinney, Geometry-induced asymmetric diffusion. Proc. Natl. Acad. Sci. **104**, 9580–9584 (2007)
29. A. Taloni, F. Marchesoni, Single-file diffusion on a periodic substrate. Phys. Rev. Lett. **96**, 020601 (2006)
30. K. Nelissen, V.R. Misko, F.M. Peeters, Single-file diffusion of interacting particles in a one-dimensional channel. Europhys. Lett. (EPL), **80**, 56004 (2007)
31. A. Sokolov, I.S. Aranson, Reduction of viscosity in suspension of swimming bacteria. Phys. Rev. Lett. **103**(14), 148101 (2009)
32. S. Rafaï, L. Jibuti, P. Peyla, Effective viscosity of microswimmer suspensions. Phys. Rev. Lett. **104**, 098102 (2010)
33. M. Engstler, T. Pfohl, S. Herminghaus, M. Boshart, G. Wiegertjes, N. Heddergott, P. Overath, Hydrodynamic flow-mediated protein sorting on the cell surface of trypanosomes. Cell **131** (2007)

Chapter 8
Conclusions and Outlook

Non-equilibrium statistics and dynamics, especially in the context of active soft matter, are very active fields of contemporary physics. Indeed, the direct and most appealing motivation of such investigations is the promise of developing a physical theory of living matter. Potential technological benefits include the possibility of using the same principles to create artificial soft functional matter that can overcome some of the limitations of present day technologies. A significant appeal of such systems would be their capability to self-organize their form and function and the ability to self-heal against destructive mechanisms. While the control of active systems from all their possible microscopic states remains an open challenge, it seems feasible to construct artificial systems by providing a sufficiently strict pre-selection of all possible configurations as we showed in Chap. 2. We used soft functional units, i.e., surfactant and lipid molecules, water and oil, constrained by micro-fluidic channel networks and demonstrated that self assembled surfactant bilayer networks in microfluidic channels may provide a crucial first step towards complex dynamical functions comprising artificial nanoscale or molecular units. More specifically, native surfactant bilayers already offer a range of different electrical behaviour that can be exploited to create wet circuitry. The stability of these objects in micro-fluidic systems is quite encouraging, both in static and in dynamic settings. The particular permeation properties of bilayer membranes for messenger molecules, such as those occurring in systems of chemical oscillators (discussed in Chap. 5), furthermore suggests the development of multi-functional, self-assembling dynamic nanoscale systems which open up novel types of active soft matter technology, which is conceptually influenced by the physical building principles of living matter, but relies on simple components apt to synthesis and thorough control.

The construction of biomimetic systems from soft components, directly enables one to test hypotheses about the many biological functions. As Richard Feynman famously noted, "What I cannot create, I do not understand", the construction of artificial systems helps to gain a deep understanding about many natural phenomena. In Chap. 3, we used a simple reconstituted system, to study the fusion of membranes in the context of neuronal signalling. We addressed the poorly understood phenomena

of the mechanism of Ca^{2+} triggering of synaptic vesicle fusion. We were able to unravel the electrostatic interactions that occur between the charged lipids and the proteins that mediate the fusion process. While we were able to reproduce, in vitro, the massive increase of membrane fusion triggered by Ca^{2+}, as seen in vivo, some of the conditions we used in order to achieve it were not completely physiological. However it is easily conceivable that many different factors of physiological environment can lead to a similar condition as we used in the experiments. Thus, the mechanism of the Ca^{2+} triggering could be a basic mechanism at the heart of biological vesicle fusion with minor variations in the conditions leading to it. Future experiments will help to unravel both such conditions and if the mechanism we uncovered here is indeed as basic as it promises to be.

Fundamental understanding, the tools and techniques that enable it and the applications that result from it all go hand in hand. In Chap. 4 we developed a technique for the direct imaging of lipid bilayers with wide ranging implications. The work demonstrated a first step towards imaging lipid bilayers reconstituted in microfluidic channels. The wide applicability of the techniques of microfluidics in a variety of interdisciplinary studies makes such an investigation vital. Our data showed that it was possible to image an unthinned lipid membrane with resolutions down to $\sim$200 nm in one dimension. The technique is particularly promising as it did not cause any photo-damage, typical of many X-ray studies, to the bilayer samples that were studied. The model that we used to extract the structural information from the data is a simple and scalable one, such that improvements of resolution up to an order of magnitude might be possible with suitable adjustments to both model and experiment.

In the second part of this work, we investigated artificial active matter—emulsion droplets dissipating chemical energy. The well known and studied Belousov-Zhabotinsky chemical reaction was run in micro-droplets, thus creating populations of chemical micro-oscillator droplets as discussed in Chap. 5. Qualitatively new phenomena emerged due to the interplay between the droplet network topologies and type of coupling between the oscillators. In combination with the results presented in Chap. 2, these open up the possibilities to construct self-organizing dynamic soft matter systems. These systems are particularly well suited as a table top system for the study of many open questions in non-equilibrium science. Effects such as quorum sensing are widely seen in natural settings and have recently been reported in artificial chemical oscillators. However, there is no deep understanding of such phenomena, particularly due to the difficulty in resolution of a single, isolated oscillator where very large populations are present. The results that we have presented in Chap. 5 might pave the way for detailed investigations.

In the light of understanding the emergence of collective states and phase transitions in non-equilibrium settings, self propelled particles are rapidly gaining popularity as an elegant model system. In this context, we introduced an artificial micro-swimmer in Chap. 6. We studied the mechanism driving its motion and characterised its velocity and showed that it mimics an idealised model of natural microscale swimming. Unlike many other artificial self propelled objects, these can be created easily and in large quantities with identical properties, without the many

irrelevant complicated mechanisms pertinent to biological systems. Therefore it is particularly well suited to study the purely physical aspects of collective motion. Indeed, in Chap. 7, we showed that hydrodynamic interactions alone might be sufficient for collective ordering to occur. We observed the formation of ordered rafts and the possibility of the existence of a phase transition from the individual to collective behaviour. We studied their collective behaviour in confinement, and found behaviour previously only predicted by theory. These studies suggest that they would be very well suited to complement theoretical approaches to obtain a quantitative understanding of collective motion. Such an understanding, naturally, has many applications. For example, understanding the collective global rearrangements of swimming microscopic algal populations, could have dramatic environmental and economic implications.

Appendix A
Materials and Methods

This describes the various protocols and recipes used in this work.

Monoolein stock

I use 25 mM monoolein in squalane as my continuous phase.
   Molecular weight of monoolein: 356.64
To make 25 mM of monoolein in squalane I use 89.16 mg in 10 mL (i.e. 8.916 mg/mL)

Monoolein/Cholesterol stock

A mixture of 25 mM monoolein and 25 mM cholesterol in squalane is used.
   Molecular weight of cholesterol: 386.65
To make 25 mM of cholesterol in squalene I use 96.6625 mg in 10 mL (i.e. 9.7 mg/mL)

Gramicidin

$10\,\mu$g/mL of gramicidin A in ethanol is used which is added to the electrolyte
(Sect. A). Molar mass of gramicidin is 1882.3 g/mol. This means that the molarity is approximately $5.5\,\mu$M.
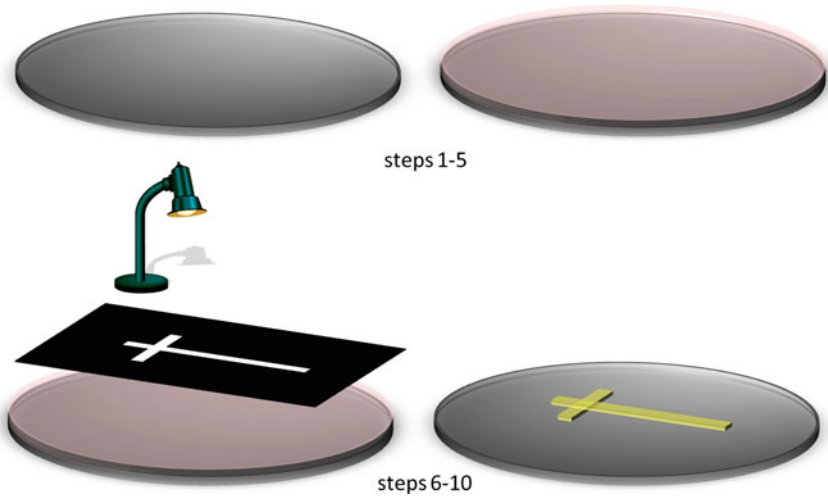
Fig. A.1 Soft lithography technique for the preparation of PDMS microfluidic devices
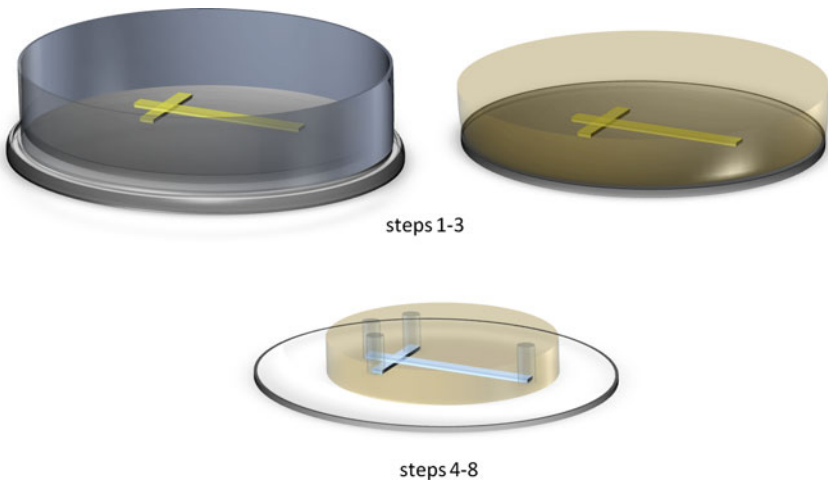
Fig. A.2 Soft lithography technique for the preparation of PDMS microfluidic devices

Microfluidic Devices

The channels are in a PDMS layer which is then bonded to a glass cover slide. The PDMS layers are formed by pouring uncured PDMS over SU-8 masters. The fabrication of the SU-8 masters and the PDMS devices is shown in Figs. A.1 and A.2 and described below in detail.

SU-8 Masters

The following is the recipe for making masters in SU-8 in the clean room.

1. Wash the silicon wafer in Isopropanol and blow dry with nitrogen
2. Heat at 200 °C for 10 min
3. Spin coat SU-8 100 (for a thickness of 100–120 μm, adjust the spin speed to 1400 RPM)
4. Pre-softbake at 65 °C for 15 min
5. Softbake at 95 °C for 40 min
6. Expose for 30 s at 15 mW, 365 nm in HP contact mode. Wait for 1 min. Expose again for 30 s.
7. Pre postbake at 65 °C for 1 min
8. Post bake at 95 °C for 8 min
9. Develop for 8–10 min in SU-8 developer
10. Sonicate for 3–4 s and wash with acetone followed by isopropanol.

PDMS and Assembly of Devices

1. PDMS (Sylgard 184) with cross linker in the ratio of 10:1 is poured over the silicon master.
2. This is degassed in the desiccator to remove bubbles. (Degas until the PDMS layer is completely free of bubbles)
3. Cure PDMS at 85 °C for 4 h
4. Cut the PDMS mould around the structure and peel off from the master.
5. Punch holes for the inlets and outlets.
6. Wash the PDMS layer and a cover slide with isopropanol and place in plasma cleaner.
7. Plasma clean at HIGH for 30 s to 1 min
8. Bond the PDMS to the glass by immediately bringing the two in contact and pressing lightly, making sure that no air is trapped in between.

Ag/AgCl Electrodes

1. A cleaned silver wire (diameter 100–300 μm) is placed in a non-metallic container containing 150 mM salt (NaCl) solution.
2. The silver wire to be chlorided in the (+) positive terminal of a power supply and the other electrode (another silver wire) to the (−) negative terminal.
3. The chloriding electrode darkens, while the other bubbles. Continue until the darkened surface is evenly coated.

Electrolyte

150 mM NaCl in Millipore water as electrolyte (8.8 mg/mL NaCl in water) is used.

Agar Salt Bridge

0.5 % (i.e. 0.5 g/ 100 mL) agarose in electrolyte solution is used to form a gel to fill the capillaries used to form the electrodes.

Pulling Micropipettes

A ramp test was done on the Sutter P-97 Flaming Brown pipette puller and the procedure for Program 1 as recommended in the manual was followed and the results are as below: (The ramp test is done to identify the temperature at which the glass will melt and can be pulled into a micropipette)

Ramp test results:
Heat: 791 (R)
So the following program was used:
Heat: R + 15 = 806
Pull: 0
Velocity: 50
Time: 150
For the borosilicate glass (1.0×0.5 mm): heating time was 7.44 s (1 loop)

Liposome Preparation

50 mg of 1,2-diphytanoyl-sn-glycero-3-phosphocholine (DPhPC, Avanti Polar Lipids, Alabaster, AL) is taken in a glass vial and Buffer (10 mM HEPES, 200 mM KCl, pH 7.06; 5 mL) is added to the lipid and vortexed for 10 s. The solution was subjected to five freeze-thaw cycles. The lipid-buffer suspension was then pushed through a 0.2 µm PTFE filter (VWR). The extruded sample was diluted with buffer to a volume of 12 mL, yielding a 2 mg/mL lipid solution. The vesicle solutions were divided into aliquots of 1 mL and stored at 4 °C.

Appendix B
Hydrodynamic Flow Fields with Axial Symmetry

In spherical coordinates, the velocity field is related to the stream function $\psi(r, \theta)$ [1] by

$$v_r = -\frac{1}{r^2\sin\theta}\frac{\partial\psi}{\partial\theta} \tag{B.1}$$

$$v_\theta = \frac{1}{r\sin\theta}\frac{\partial\psi}{\partial r} \tag{B.2}$$

The stream function satistisfies the differential equation $E^4\psi = 0$, where

$$E^2\psi = \left(\frac{\partial^2}{\partial r^2} + \frac{\sin\theta}{r^2}\frac{\partial}{\partial\theta}\frac{1}{\sin\theta}\frac{\partial}{\partial\theta}\right)\psi \tag{B.3}$$

Simple solutions to Eq. B.3 are given by

$$\psi = \sin^2\theta\left(A_1 r^4 + A_2 r^2 + A_3 r + \frac{A_4}{r}\right) \tag{B.4}$$

where $A_1, ..., A_4$ are constant parameters determined by boundary conditions. The corresponding pressure field is given by $P = -\eta\cos\theta\left(20A_1 r + 2A_3/r^2\right) + P^\infty$, where P^∞ is the pressure far from the spherical droplet. The body force acting on the droplet which is balanced by forces exerted by the hydrohynamic flow is $f^P = -8\pi\eta A_3$ [1].

The solution of the form given by Eq. B.4 with boundary conditions $v_\theta(r = a) = v_s(\theta)$ and $v_r(r = a) = 0$ is determined in the frame of moving with the droplet. Here, $v_s(\theta)$ is the velocity on the surface of the droplet of radius a. For large r, the Stokes' flow requires motion at constant velocity Δv, $v_r \simeq -\Delta v\cos(\theta)$ and $v_\theta \simeq \Delta v\sin\theta$. From the latter conditions, it follows that $A_1 = 0$, and $2A_2 = -\Delta v$. Because there is no external force acting on the droplet, $f^P = 0$ and thus $A_3 = 0$. The boundary conditions on the droplet surface imply that $A_4 = -A_2 a^3$ and $3A_2 = (\kappa)\,\partial_x\phi$. The corresponding flow field can be calculated using the relation between the stream

function and the velocity as given in Eq. B.2 and is given by Eq. 6.6. For an arbitrary distribution of surface slip $v_s(r = a) = v_s(\theta)$, a $1/r^2$ term for the corresponding flow field exists in general. This term vanishes by symmetry if the surface slip is a symmetric function $v_s(\theta) = v_s(\pi - \theta)$ such as is the case for $v_s \sim \sin(\theta)$ described by Eq. 6.5.

Reference

1. J. Happel, H. Brenner, *Low Reynolds Number Hydrodynamics: With Special Applications to Particulate Media*, 1st edn. (Springer, Berlin, 1973)

Curriculum Vitae

Personal Details

Name	Shashi Thutupalli
Place of birth	Bapatla (India)
Nationality	Indian

Education

2012–present	Postdoctoral Fellow, Princeton University, Princeton, USA
2011–2012	Postdoctoral Fellow, Max Planck Institute
	for Dynamics and Self Organization, Göttingen, Germany
2007–2011	Doctoral Research, Max Planck Institute
	for Dynamics and Self Organization, Göttingen, Germany
2003–2005	Master of Applied Science,
	University of Toronto, Canada
1997–2001	Bachelor of Engineering (Electronics),
	Bangalore University, India

Employment

2005–2007	Research Scientist,
	General Electric Global Research Center, Bangalore, India
2001–2003	Engineer,
	CoreEL Technologies, Bangalore, India

Fellowships

2012–2015	Human Frontier Science Program Cross Disciplinary Fellowship
2008	International Max Planck Research Fellowship
	(did not use)
2003–2005	University of Toronto Graduate Fellowship
2003	Melbourne Post-Graduate Research Scholarship
	(did not accept)